PRESIDENCY UNIVERSITY

DEPARTMENT OF LIFE SCIENCES

PhD Thesis Synopsis

Studies on the conformational dynamics of HIV-1 accessory proteins to guide new therapeutic development

Name of Candidate: **SATYABRATA MAJUMDER**

Registration Number with date: **R-18RS18120187 (Date: 11th February, 2020)**

Name of Supervisor: **Dr. KALYAN GIRI**

Anita Mukherjee
17.01.2024

17/01/24

17/1/24

17/1/24

17/1/24

17-1-24

17/01/24

Name: SATYABRATA MAJUMDER

Supervisor: Dr. KALYAN GIRI

Co-supervisor (if any):

Title of Thesis: Studies on the conformational dynamics of the HIV-1 accessory proteins to guide new therapeutic development

PhD registration Number with date: R-18RS18120187 (Date: 11th February, 2020)

Enrolment Number with date: PU/PHD/DLS/2018/089 (30th October, 2018)

Place of work: Department of Life Sciences

Residential Address: Vill.+P.O.: Nabapally, Champahati; P.S.: Baruipur; Dist.: South 24 Parganas; State: West Bengal; PIN: 743330

Corresponding Address:

Email: majumdersatyabrata400@gmail.com, satyabrata.rs@presiuniv.ac.in

Phone Number: 9733567406, 8768087851

Satyabrata Majumder 24/11/23

Signature of Research Scholar

Kalyan Giri 24/11/23

Signature of Supervisor

Dr. Kalyan Giri
Assistant Professor
Department of Life Sciences
Presidency University, Kolkata

Contents

Topic	Page No.
Abstract	**4**
Introduction	**5-7**
Methodology	**8-13**
Result and Discussion	**14-60**
Conclusion	**61-62**
Significance of the study	**63**
Future directions	**64**
Reference	**65-71**

Abstract

The human immunodeficiency virus-1 (HIV-1) encodes four accessory proteins that play critical roles in viral pathogenesis. This research utilized integrated computational modeling and molecular dynamics (MD) simulation techniques to elucidate the structural dynamics and previously unexplored functional mechanisms of Vpr, as well as the process of designing and repurposing drug-like candidates against Vpr and Nef. Molecular dynamics simulations revealed novel insights into Vpr's conformational space for membrane association and ion channel formation processes. The Vpr C-terminal helix (residues 54-77) was found to be stably embedded within lipid bilayers, likely comprising the transmembrane core of its ion channel structure for the first time. Multimeric Vpr ion channel models were proposed, providing the first structural insights into this oligomeric complex. Analysis of Nef's conformational space identified a conserved druggable pocket that participates in homodimerization, representing a potential target. Fragment-based approaches generated novel lead compounds against Nef, which were optimized via advanced MD simulations. We also found Viprinin (a coumarin derivative) and two of its potent derivatives as potent targets for Vpr. The findings provide crucial insights into viral mechanisms and assist structure-based drug discovery efforts against HIV-1 accessory proteins. The proposed ion channel models and inhibitor compounds establish a computational framework for future investigations into HIV-1 structural biology and drug development.

Introduction

The human immunodeficiency virus (HIV) is the causative agent of the global pandemic acquired immunodeficiency syndrome (AIDS) in humans. HIV-1 initiates a long-lasting infection within human hosts, leading to the gradual decline of CD4+ lymphocytes, which are the primary in vivo target cells for the virus, ultimately leading to compromised cellular immune function [1]. In 2022, an estimated 39.0 million people were living with HIV, 1.3 million newly contracted the virus, and approximately 630,000 died from AIDS-related illnesses [2]. HIV-1, a member of the lentivirus family, contains genetic instructions for retroviral Gag, Pol, and Env proteins, as well as four accessory proteins known as Vpu, Vif, Nef, and Vpr [3]. These proteins are multifunctional in nature which selectively interacts with plethora of cellular proteins, and remarkably, their operational tactics share a common thread: none of these proteins possess intrinsic enzymatic capabilities; rather, they appear to function as molecular adaptors and orchestrating host cell manipulation [4]. Studies conducted in vivo or in primary cell types vulnerable to HIV-1 infection has exhibited that the accessory proteins can significantly modify the trajectory and intensity of viral infection, replication, and the progression of the associated disease [5]. The main functional roles of these accessory proteins in the advancement of disease are summarized below:

HIV-1 Vpu is an 81-amino acid type I transmembrane protein exhibiting characteristics consistent with class IA viroporins, featuring a single transmembrane domain, a luminal amino terminus, and a cytosolic carboxy terminus [6-9]. HIV-1 Nef and Vpu independently reduce CD4 receptor levels in infected cells, with Nef affecting pre-existing CD4 at the plasma membrane and Vpu targeting newly synthesized CD4 in the endoplasmic reticulum. The cytoplasmic domain of Vpu plays a crucial role in this modulation. Phosphorylation of Serines S52 and S56 at the cytosolic domain of Vpu by casein kinase II is essential for this function. The Vpu mediated CD4 downmodulation hinders antibody-dependent cell-mediated cytotoxicity (ADCC) and promotes virus propagation by protecting infected cells from elimination [10-17]. Vpu plays a crucial role in counteracting the antiviral host restriction imposed by BST2, a glycoprotein that tethers viral particles to the cellular membrane and preventing virus release. Vpu interacts with BST2, leading to its removal from the plasma membrane and subsequent degradation in lysosomes or the proteasome, thereby preventing its incorporation into virions [18]. Vpu also serves as an ion channel protein, forming homo-oligomers through its transmembrane domain and likely assembling as a pentamer [19, 20]. These Vpu channels are weakly selective for monovalent cations over anions, and their activity correlates with CD4 degradation [21]. The C-terminal helices of Vpu modulate

oligomerization and channel conductance, while Vpu-induced enhancement of viral release is associated with membrane potential depolarization in host cells [22]. Additionally, Vpu can interact with the cellular inward K+ rectifier TASK1, leading to its degradation, and indicating Vpu's potential role in disturbing K+ transport. This ion channel function influences cell permissiveness for Vpu-defective viruses and has been observed in various model systems, including Xenopus oocytes and yeast [23]. Apart from this, Vpu downregulates host cellular proteins such as CCR7, CD1d, CD40, CD81, CD155, MHC-1, TSPANs (25, 26, 28 and 30) which directly or indirectly enhance viral replication, release and consequently disease progression [24].

HIV-1 Vif is a positively charged, 23-kilodalton (kDa) protein consisting of 192 amino acids [25].The main of this accessory protein is to counteract the antiviral action of APOBEC3G by inhibiting its incorporation into viral particles, mainly through proteasomal degradation. Vif forms an E3 ligase complex, Vif–Cul5–EloB/C, which promotes the polyubiquitination and subsequent proteasomal degradation of APOBEC3G. Vif also antagonizes other APOBEC3 proteins, including APOBEC3C to H, through the same E3 ligase complex, relying on specific interaction sites and motifs, such as the SOCS box and zinc-binding motifs. It has also been shown that a T cell transcription factor, core-binding factor subunit beta (CBFβ), directly interacts with Vif and helps in the formation of stable Vif–Cul5–EloB/C E3 ligase complex [26].

Nef is a small nonenzymatic accessory protein, typically weighing between 27 and 34 kDa. It is expressed during the early stages of the viral life cycle and carries out a diverse range of functions within the host cells. Nef consists of two main parts: the N-terminal anchor region and a folded core region that houses a flexible internal loop spanning approximately 25 residues. The initial 60 amino acids comprising the anchor region are primarily disordered and feature a myristoylation site at the initial glycine residue. This myristoylation facilitates Nef's attachment to the pliable core of the membrane leaflet. Nef engages in interactions with a diverse array of membrane proteins and factors, including CD4, CXCR4, CCR5, MHC-I, T-cell receptor, SERINC5, trafficking proteins, guanine nucleotide exchange factors, protein kinases, and many others [27-32]. One of its conserved functions among all HIV-1 Nef M-group subtypes is to activation of Hck kinase. Numerous structural and in vitro analyses focusing on the recruitment and activation of Src-family kinases have indicated that Nef displays a selective affinity for the SH3 domain of Hck and Lyn kinases. This interaction results in the displacement of the SH3 domain from its typical regulatory position within the

kinase, ultimately leading to the constitutive activation of the kinase in in vitro systems which results in increased HIV-1 transcription and viral replication in macrophages [33-35].

Vpr, a protein comprising 96 amino acids with a molecular weight of 14 kDa, exhibits conservation in both HIV-1 and Simian immunodeficiency virus SIV. Its multifaceted functions in the host cell contribute to the disease's progression, ultimately assisting in the advancement of AIDS [36, 37]. Vpr plays a crucial role in transporting the viral Pre-Integration Complex (PIC) from the cytoplasm to the host cell nucleus via interaction with importin-α and it another prominent function is to inducing G2 cell cycle arrest. Vpr's binding to importin-α has been elucidated through crystal structures, shedding light on the nuclear transportation process [38]. The mechanism behind Vpr-induced G2 cell cycle arrest is not fully understood, but studies have showed that it targets a chromatin-bound substrate, leading to ubiquitination and proteolysis, which activates the G2/M checkpoint mediated by ataxia telangiectasia-mutated and Rad3-related proteins, resulting in G2 cell cycle arrest. Recent research involving the crystal structure of the DDB1–DCAF1–Vpr–UNG2 complex has revealed how Vpr guides UNG2 (Uracil DNA glycosylase) towards degradation, further inducing G2 cell cycle arrest [39, 40]. Apart from these Vpr has an intriguing ability to form cation selective ion channel on the host cell plasma membrane [41, 42]. Given its crucial role in AIDS pathogenesis, Vpr is a promising target for therapeutic interventions.

Currently authorized medications exclusively focus on HIV-1 Pol and Env-encoded proteins, such as reverse transcriptase (RT), protease (PR), integrase (IN), and gp41. Consequently, broadening the spectrum of molecular targets in HIV-1 therapy by including the accessory proteins could potentially diversify treatment alternatives, ultimately yielding impactful and highly effective novel therapeutic approaches. But in order to initiate drug designing campaign against the accessory proteins, in depth knowledge of the conformational space of the proteins are required. Thorough understanding of the conformational changes involved in protein-protein interactions, such as those between accessory proteins and cellular factors, is critical for designing drugs that disrupt these interactions and inhibit viral replication. Conformational analysis can also reveal unique pockets or regions in the protein structures that are not evident in a single static structure. Targeting these specific sites can lead to more effective and selective drug design.

Methodology

1. Sequence retrieval, transmembrane domain prediction, and structure modeling

The Vpr sequence was retrieved from the Uniprot database (ID: P69726) [43]. To predict the transmembrane topology of this protein sequence, HMMTOP [44] and TMHMM [45] servers were employed. Both of these servers utilize Hidden Markov Models (HMMs) to make predictions about the transmembrane structure of proteins. For generating the Vpr homology model, NMR structure of Vpr (PDB Id:1M8L) [46] was used as template and SwissModel [47] server was used to build the model.

The HIV-1 Nef protein structure was taken from the Protein Data Bank (PDB) entry 4U5W [48]. We conducted a comparative analysis of Nef from 4U5W with all other available Nef structures in the PDB that include the region of interest and found significant similarity with the available 3D structures, with a root-mean-square deviation (RMSD) of the backbone less than 1.5Å. This step shows that Nef maintains a consistent conformation when interacting with various cellular partners. Any missing residues were modeled with CHARMM-GUI [49].

2. Identification of druggable pockets

To identify potential druggable binding sites on the Nef protein DeepSite [50] and FTMap [51] servers were employed. DeepSite utilizes a knowledge-based approach involving the use of 7622 proteins from the scPDB database of binding sites to construct convolutional neural networks (CNN). On the other hand, the FTMap method involves the distribution of 16 small organic probe molecules with varying shapes, sizes, and polarities across the protein surface.

3. Fragment-based small molecule design

AutoGrow4 was employed to generate small ligand molecules in the specified pocket. We utilized AutoGrow4's [52] default fragment library molecules, categorized into four groups based on molecular weight (MW $\leq$ 100 Da, 100 Da < MW $\leq$ 150 Da, 150 Da < MW $\leq$ 200 Da, and 200 Da < MW $\leq$ 250 Da), sourced from the ZINC15 database. OpenBabel 2.3.1 was used to convert the SMILES fragment libraries into 3D pdbqt format. We defined a docking grid of 22 Å × 20 Å × 20 Å at the specified protein pocket, with the center of mass (COM) of the FTMap probe cluster (probes that bound to pocket 3) serving as the grid center (grid center coordinates: -1.57, -0.653, 19.762 in x, y, and z directions).

4. General MD simulation setup

System description	Simulation Engine	Force-field description	Simulation box type	Temperature (K)	Production simulation duration	No. of independent replicates
Vpr in water	GROMACS 2018.3	GROMOS96 54a7	Dodecahedron	300	50 ns	7
Vpr complexed with viprinin	GROMACS 2018.3	GROMOS96 54a7	Dodecahedron	300	50 ns	7
Vpr complexed with ViprininD1	GROMACS 2018.3	GROMOS96 54a7	Dodecahedron	300	50 ns	7
Vpr complexed with ViprininD2	GROMACS 2018.3	GROMOS96 54a7	Dodecahedron	300	50 ns	7
Nef in water	GROMACS 2020.5	AMBER99SB-IILDN	Cubic	300	100 ns	20
Nef complexed with compound 1	GROMACS 2020.5	AMBER99SB-IILDN	Cubic	300	100 ns	3
Nef complexed with compound 2	GROMACS 2020.5	AMBER99SB-IILDN	Cubic	300	100 ns	3
Nef complexed with compound 2-mod1	GROMACS 2020.5	AMBER99SB-IILDN	Cubic	300	100 ns	3

Nef complexed with compound 2-mod2	**GROMACS 2020.5**	**AMBER99SB-IILDN**	**Cubic**	**300**	**100 ns**	**3**
Vpr C_helix in POPC membrane	**GROMACS 2022.4**	**CHARMM36**	**Rectangular**	**310**	**200 ns**	**3**
Vpr C_helix in DPPC membrane	**GROMACS 2022.4**	**CHARMM36**	**Rectangular**	**323.15**	**250 ns**	**3**
Vpr N_helix in DPPC membrane	**GROMACS 2022.4**	**CHARMM36**	**Rectangular**	**323.15**	**250 ns**	**3**
N_helix system 1 (POPC mebrane)	**GROMACS 2022.4**	**CHARMM36**	**Rectangular**	**310**	**200 ns**	**3**
N_helix system 2 (POPC mebrane)	**GROMACS 2022.4**	**CHARMM36**	**Rectangular**	**310**	**200 ns**	**3**
Full length Vpr in Vertical orientation inside POPC bilayer	**ACEMD3**	**CHARMM36**	**Rectangular**	**310**	**1000 ns**	**3**
Full length Vpr in Horizontal orientation inside POPC bilayer	**ACEMD3**	**CHARMM36**	**Rectangular**	**310**	**1000 ns**	**3**

System description	Simulation Engine	Force-field description	Simulation box type	Temperature (K)	Production simulation duration	No. of independent replicates
Vpr C_helix in random mixture of CG POPC lipid and TIP3P water beads	**GROMACS 2021.5**	**ElneDyn 3.0.0**	**Cubic**	**310**	**200 ns**	**3**
Vpr N_helix in random mixture of CG POPC lipid and TIP3P water beads	**GROMACS 2021.5**	**ElneDyn 3.0.0**	**Cubic**	**310**	**200 ns**	**3**
Vpr C_helix in random mixture of CG POPC and POPE (1:4) lipid and TIP3P water beads	**GROMACS 2021.5**	**ElneDyn 3.0.0**	**Cubic**	**310**	**200 ns**	**3**
Vpr N_helix in random mixture of CG POPC and POPE (1:4) lipid and TIP3P water beads	**GROMACS 2021.5**	**ElneDyn 3.0.0**	**Cubic**	**310**	**200 ns**	**3**
Vpr C_helix Oligomers (Tetramer to Heptamer) in POPC lipid bilayer	**GROMACS 2022.3**	**CHARMM36**	**Cubic**	**310**	**300 ns for each Oligomer**	**3 for each Oligomer**

5. ColDock Simulation

In ColDock [53] simulations, multiple ligands (6, 8, and 10) were placed randomly within 20 Å of protein atoms in a 30 Å × 30 Å × 30 Å cubic box. These systems were solvated with TIP3 water and a salt concentration of 0.15 M, using the AMBER99SB-IILDN force field. To prevent ligand aggregation during MD, a repulsive Lennard-Jones potential was applied between ligand molecules. Initial 50 ns MD simulations with 33 ligand molecules in a 12 Å × 12 Å × 12 Å cubic box with TIP3 water and 0.15 M Na+ and Cl- ions were conducted to assess aggregation. The radial distribution function (RDF) using the central C18 atom showed that without the repulsive force, ligand molecules aggregated (<6 Å), but with the repulsive force, they did not aggregate. A flat RDF value around unity at r > 10 Å indicated a uniform distribution, while the repulsive force prevented aggregation when ligands approached each other (<10 Å). Following Nef-multiple ligands system simulations, ligand poses were clustered based on contact with Nef, allowing the selection of multiple ligand poses from MD trajectory.

6. AquaMMapS water analysis

The Nef protein (PDB ID: 4U5W) was prepared for the CHARMM36 force field in a series of steps. The Hck SH3-SH2 kinase monomer was removed, and hydrogen atoms were added, accounting for a simulated pH of 7.0. The protonation of titratable side chains was manually verified. Subsequently, TIP3P water molecules were introduced to the simulation box using the VMD Solvate plugin 1.5. To ensure overall charge neutrality, Na+/Cl- counter ions were added up to a final concentration of 0.15 M, employing the VMD Autoionize plugin 1.3. For both equilibration and productive simulations, the ACEMD3 [54] MD engine was utilized.

7. Multiple walkers supervised molecular dynamics (mwSuMD) simulations

In this method, a single ligand molecule was placed approximately 35 Å from pocket 3 of Nef and it was parameterized with the GAFF force field through Antechamber. Six independent mwSuMD [55] replicas were conducted. Atomic contacts were analyzed using the GetContacts tool, with a donor-acceptor threshold distance of 3.5 Å and a 120° angle. Molecular mechanics energies were calculated with the MMPBSA.py script from AmberTools20, employing the MM/GBSA method for solvation continuum effects.

8. Protein lipid interaction analysis

To analyze and quantify the interactions between lipids and proteins, we processed the trajectories from both the CG self-assembly MD simulation and the all-atom MD simulation of the C_helix using PyLipID tool (version 1.5.0) [56].

9. Molecular docking

Viprinin, ViprininD1 and ViprininD2 were docked on the specified site of Vpr using Autodock 4.2.6 [57]. The docking simulation box was centered on the region encompassing Glu25 and Gln65 with dimensions of 60 Å in all three directions (Xcenter, Ycenter, and Zcenter coordinates were set to -2.909, -5.097, and -0.331, respectively), and a grid spacing of 0.375 Å was applied. The initial coordinates of the ligands after minimization were used as the starting point for docking. Three independent docking runs were conducted, varying the number of Genetic Algorithm (GA) runs (100, 200, and 300), population size (250, 350, and 400), and RMS cluster tolerance (1 Å, 2 Å, and 2 Å). All other parameters were maintained at their default values. Lamarckian Genetic Algorithm search space was employed for the docking simulation. The docked poses with the most negative binding energy, indicating the lowest energy/score complexes, from the three docking runs were selected for subsequent Molecular Dynamics simulations for each Vpr-ligand system.

10. Umbrella sampling simulation

Three separate pulling simulations were initiated (using GROMACS 2018.3) from an energy-minimized solvated complex structure with different random number seeds. To predict the unbinding pathway, the Caver program was employed, and complexes were aligned along the Z-axis accordingly. In each of the three pulling simulations, Vpr remained stationary as a reference, while viprinin, viprininD1, and viprininD2 were pulled along the Z-axis within a box size of 6.56 Å (x-axis), 4.362 Å (y-axis), and 14 Å (z-axis) over 500 ps, employing a force constant of 600 kJ/mol/nm2. The pull rate was set at 0.005 nm per ps. Conformations of solvated complexes were recorded at 0.2 nm intervals during the unbinding process, generating varying snapshot numbers (ranging from 11 to 16) for different complexes. Additionally, an extra conformation was included to ensure 0.1 nm spacing within the first three windows due to limited ligand diffusion in the bound state. Subsequently, conformations underwent 100 ps NPT equilibration before a 5 ns MD run at 300 K. The potential of mean force (PMF) was extracted from Umbrella sampling simulation outputs using weighted histogram analysis (WHAM) with the gmx wham module.

Results and Discussion

Objective 1: **<u>Study on the conformational dynamics of the HIV-1 accessory proteins</u>**

1.1 Conformational dynamics of HIV-1 Vpr in lipid environment

1.1.1 Conformational feature of C_helix (residues 53-80) and N_helix (residues 12-34) in lipid bilayer

To predict Vpr ion channel topology, understanding protein conformation is crucial. In the later section, Coarse-grain simulations revealed C_helix as the putative transmembrane region, and N_helix displayed amphipathic behaviour by associating with a bilayer leaflet at the solvent side. To further explore the conformational dynamics, 200 ns all-atom MD simulation of N_helix (in triplicate) were conducted taking the last snapshots from the coarse-grained simulations (system 1 and system 2) (**Figure 1**).

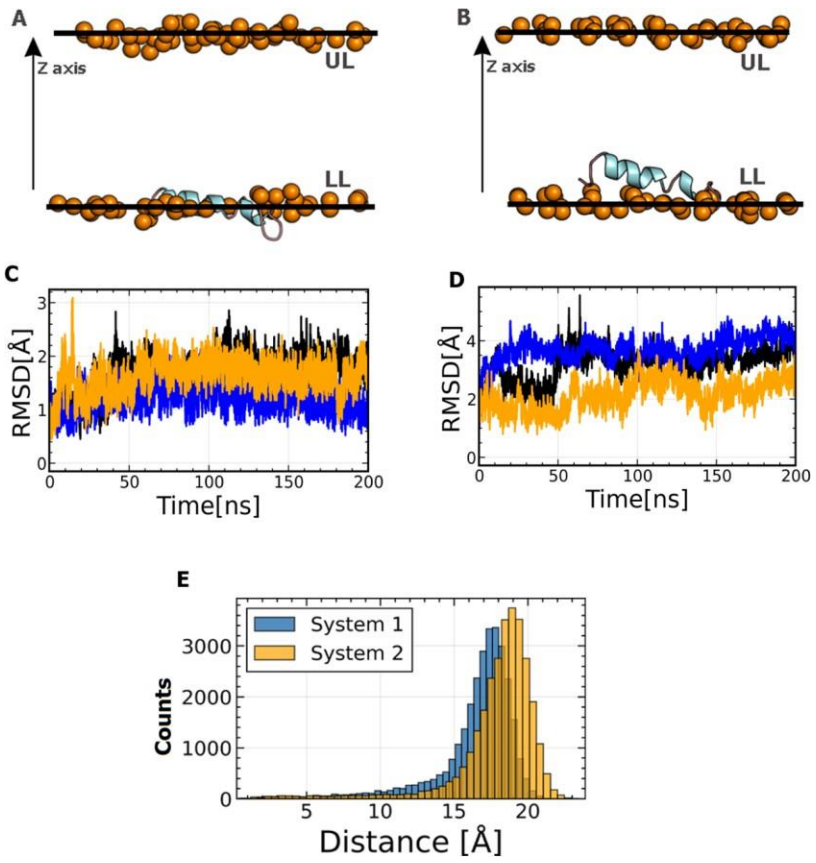

Figure 1: Initial configuration of N_helix (cyan) in A) system 1 and B) system 2. Orange beads are lipid phosphate head groups (UL: upper leaflet, LL: lower leaflet). RMSD of the backbone atoms of N_helix with three independent replicates (black: replica 1, blue: replica 2

and orange: replica 3) from C) system 1 and D) system 2. All the simulations are converged as indicated by the plateau in RMSD trajectories. E) Frequency (no. of frames from three concatenated trajectories) histogram of the distance between com of N_helix and POPC membrane during the simulations (mean distance value for system 1 is 16.43 ± 2.87 Å and for system 2, it is 18.00 ± 2.92 Å).

Throughout the simulation, the N_helix in system 1 displayed remarkable conformational stability (**Figure 1C**) and it was attributed to the substantial number of hydrogen bonds and salt bridge contacts with water and phospholipid head groups at the bilayer-solvent interface. In contrast, in system 2, the N_helix exhibited substantial conformational changes due to the increased hydrophobic interactions with the lipid bilayer (POPC) which results in the collapse of the α-helical structure in N-terminal residues 12-19 (**Figure 2**).

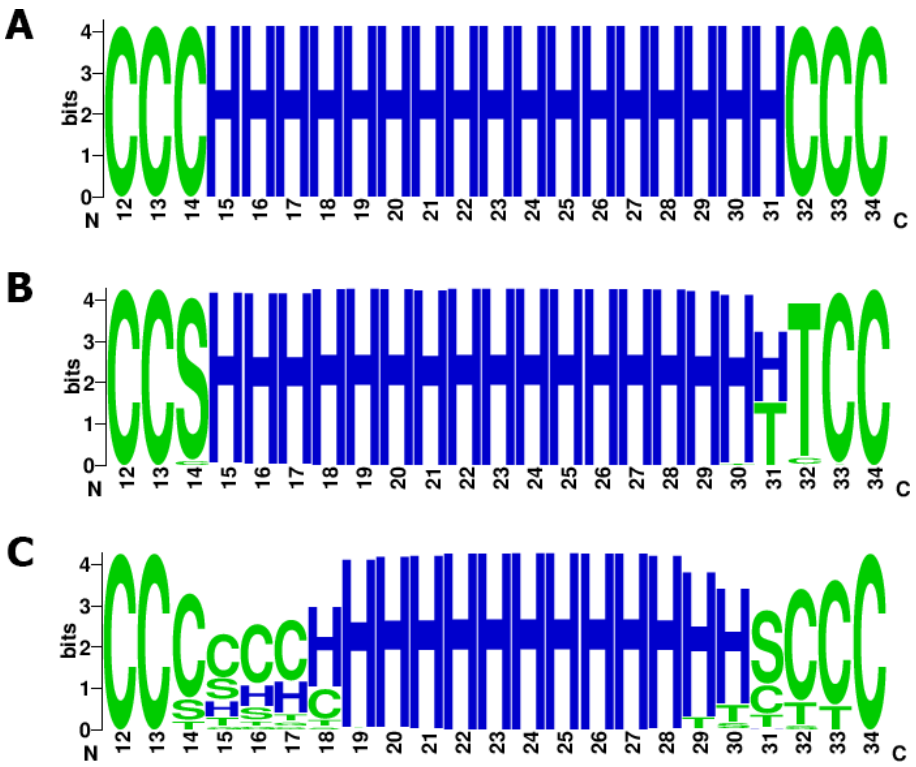

Figure 2: Secondary structure of the N_helix during simulation calculated using DSSP program. The average configuration was plotted using Weblogo tool. 'C', 'S', 'T' and 'H' denotes random coil, sheet, turn and α-helix respectively. A) Initial secondary structure for both system 1 and system 2 N_helix. B) Average secondary structure of the N_helix of system 1 calculated from three replicas. C) Average secondary structure of the N_helix of system 2 calculated from three replicas.

In both systems, the N_helix remained stabilized in its initial position, as indicated by the distance between the protein and bilayer center of mass during the simulation (**Figure 1E**). N_helix displayed high conformational stability in both POPC and DPPC membrane systems (**Figure 4C, D**). However, due to its amphipathic nature, it exhibited significant lateral displacement along the Z-axis in both systems (**Figure 5C, D**).

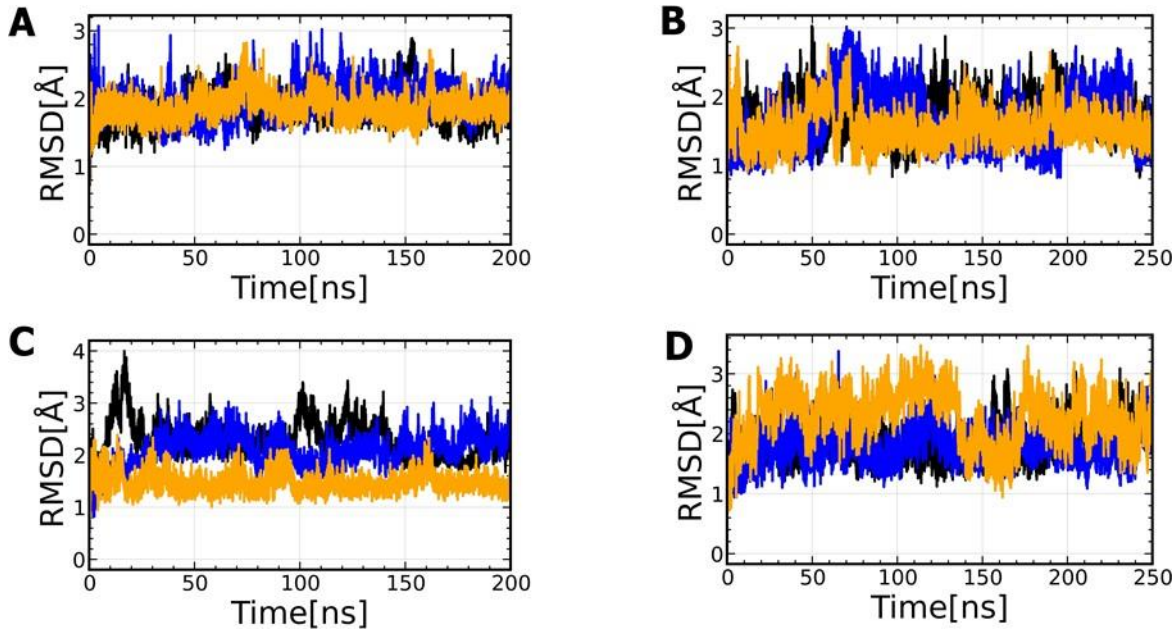

Figure 4: All the simulations were done in triplicate (black: replica 1, blue: replica 2 and orange: replica 3). RMSD of the backbone of C_helix in A) POPC and B) DPPC bilayer and the RMSD of the backbone of N_helix in C) POPC and D) DPPC bilayer.

C_helix remained highly stable throughout the 200 ns simulation with minimal lateral displacement (**Figure 5A**) when introduced at 21° tilt angle. C_helix exhibited even greater stability (**Figure 4B**) and minimal lateral displacement (**Figure 5B**) in the DPPC membrane. The root mean square fluctuation (RMSF) of the backbone (**Figure 6**) of the C_helix residues in POPC and DPPC system shows a similar profile.

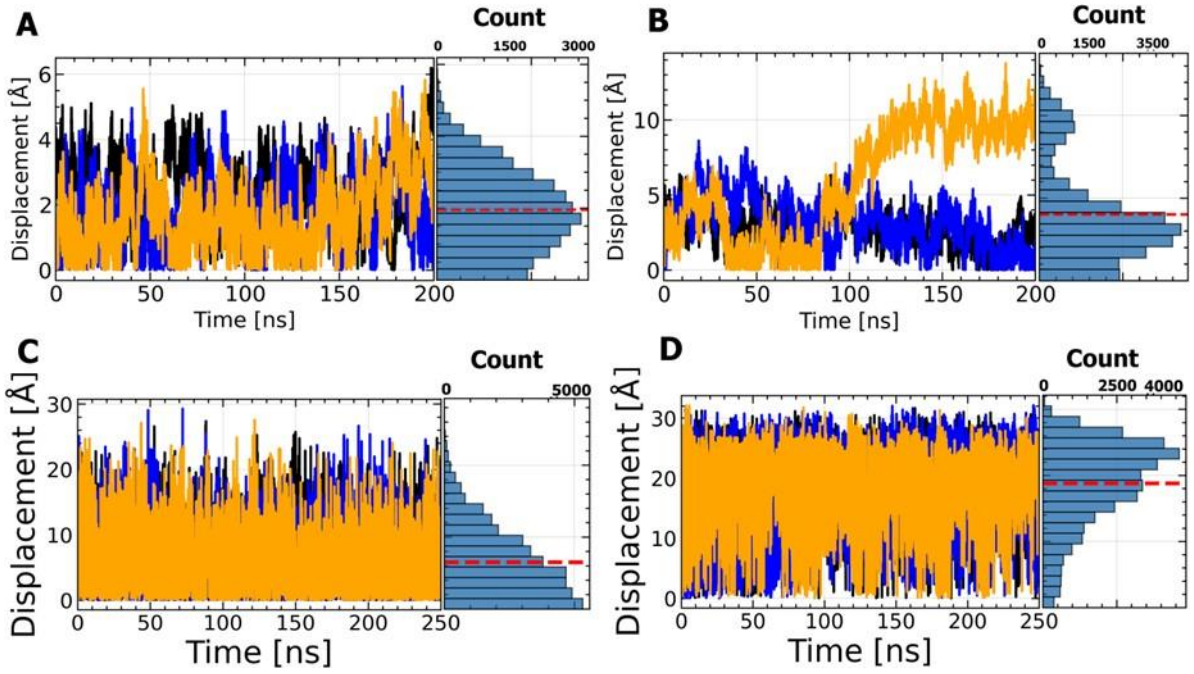

Figure 5: Lateral displacement of C_helix in A) POPC, B) DPPC bilayer and the lateral displacement of N_helix in C) POPC, D) DPPC bilayer. The red dashed lines in the count plots are the mean calculated using the three concatenated replicas.

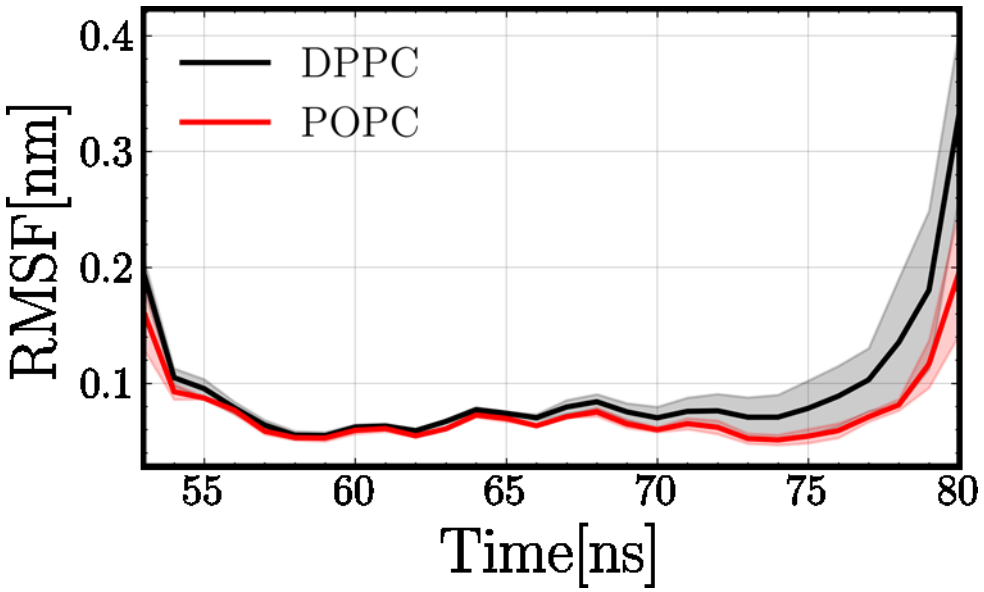

Figure 6: Mean RMSF (Root mean square fluctuation) plot of the backbone atoms of C_helix residues in DPPC and POPC membrane system drawn from three replica simulations. The red and black transparent areas are the respective standard deviation.

1.1.2 Conformational feature of full-length Vpr inside POPC bilayer

We conducted three independent 1 μs MD simulations of the full-length Vpr protein within a POPC bilayer in both horizontal and vertical orientations to gain a deeper insight into the structural arrangement of the complete Vpr protein in lipidic environment. In the horizontal system, significant structural changes and collapse of core three helix structure in Vpr protein were observed during MD simulations as indicated by the increased RMSD and the distance between the COM of the N_helix and C_helix (**Figure 7A, C**). Vpr's ability to adopt different conformations in response to its environment is highlighted in a previous study where it adopted a distinctive fully open "U" shaped conformation in H_2O/Trifluoroethanol environment [58]. In contrast, the vertical system showed much higher stability throughout the simulation (**Figure 7B**). Hydrogen bond interactions played a crucial role in maintaining the three-helix structure of Vpr in the vertical system, while these interactions were disrupted in the horizontal system, leading to loss of the native folding although similarities in intra-hydrophobic contacts were observed between the two systems (**Figure 8**). PCA of the trajectories obtained single prominent clusters in both horizontal and vertical system (**Figure 7E, F**). In the final conformations of Vpr from both systems, it was consistently observed that, despite the lipid environment favoring some conformational deviation, the C_helix remained stably positioned within the lipid bilayer (**Figure 7H, I**). These observations indicate that the lipid environment affects Vpr's conformations which is vital for its role as an ion channel.

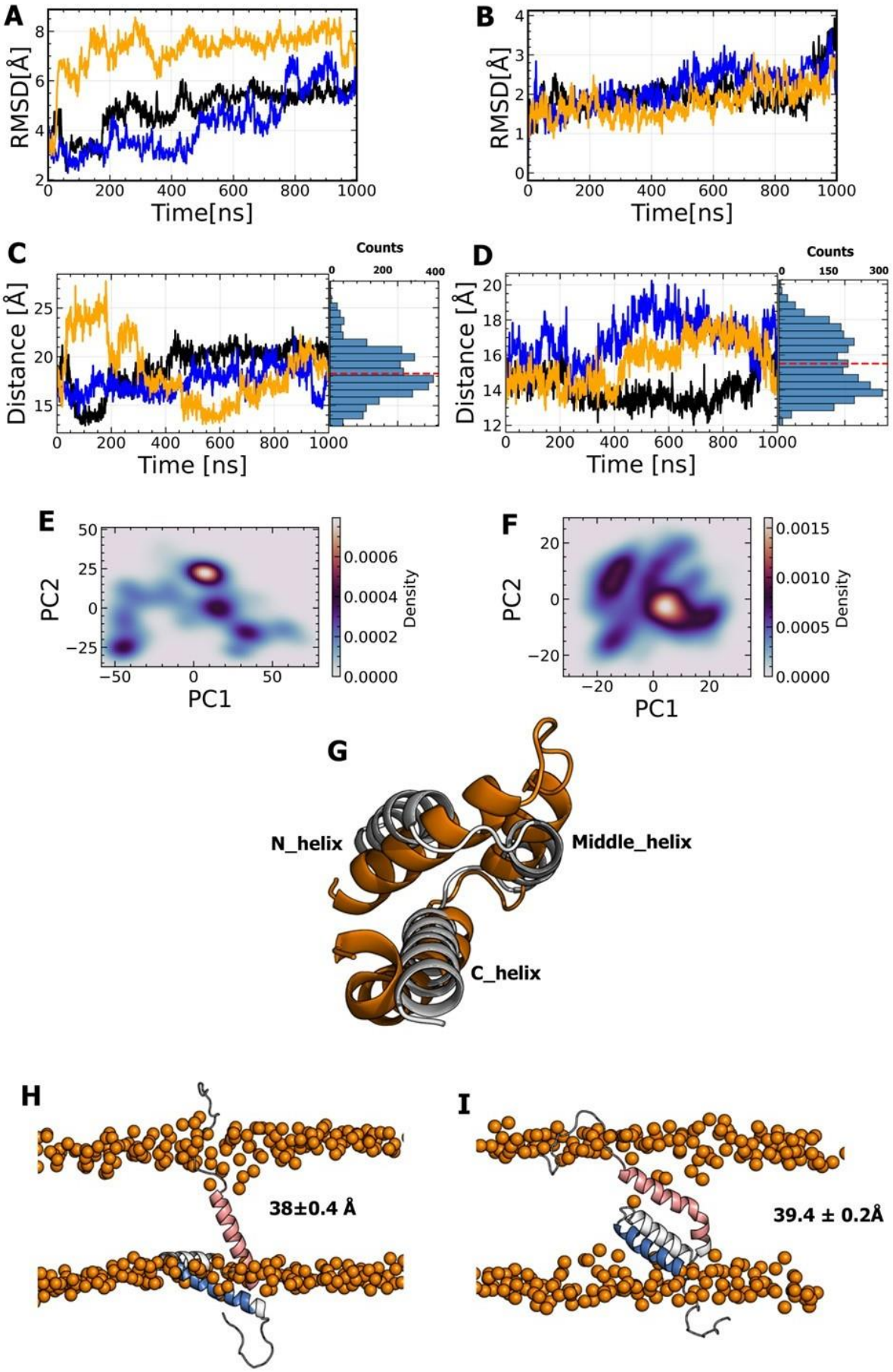
A
RMSD[Å]
Time[ns]
B
RMSD[Å]
Time[ns]
C
Distance [Å]
Time [ns]
Counts
D
Distance [Å]
Time [ns]
Counts
E
PC2
PC1
Density
F
PC2
PC1
Density
G
N_helix
Middle_helix
C_helix
H
38±0.4 Å
I
39.4 ± 0.2Å

Figure 7: RMSD of the backbone of Vpr region 17-77 of A) horizontal and B) vertical orientation during simulation. Three independent replicas have been run (black: replica 1, blue: replica 2 and orange: replica 3). Distance between com of N_helix and C_helix in C) horizontal and D) vertical orientation. The red dashed lines in the respective frequency plots are the mean values calculated from the three replicas. PCA density plot of Vpr (region 17-77) from E) horizontal system and F) vertical system. G) Superimposition of representatives extracted from the center of the highest density regions. Orange and white-colored conformations are extracted from plots E and F respectively. Backbone atoms were used for the superimposition and N terminal 1-16 and C terminal 78-96 random coil regions were excluded from the computation. The last configuration from replica 1 of H) horizontal and I) vertical systems from simulations. Orange beads represent the POPC phosphate head groups, in blue is the N_helix, pink is the C_helix, and white is the middle helix. Some of the headgroups are omitted to visualize the helices properly. Membrane thickness is computed by calculating the distance between the density peaks (along the Z-axis) of lipid phosphate head groups.

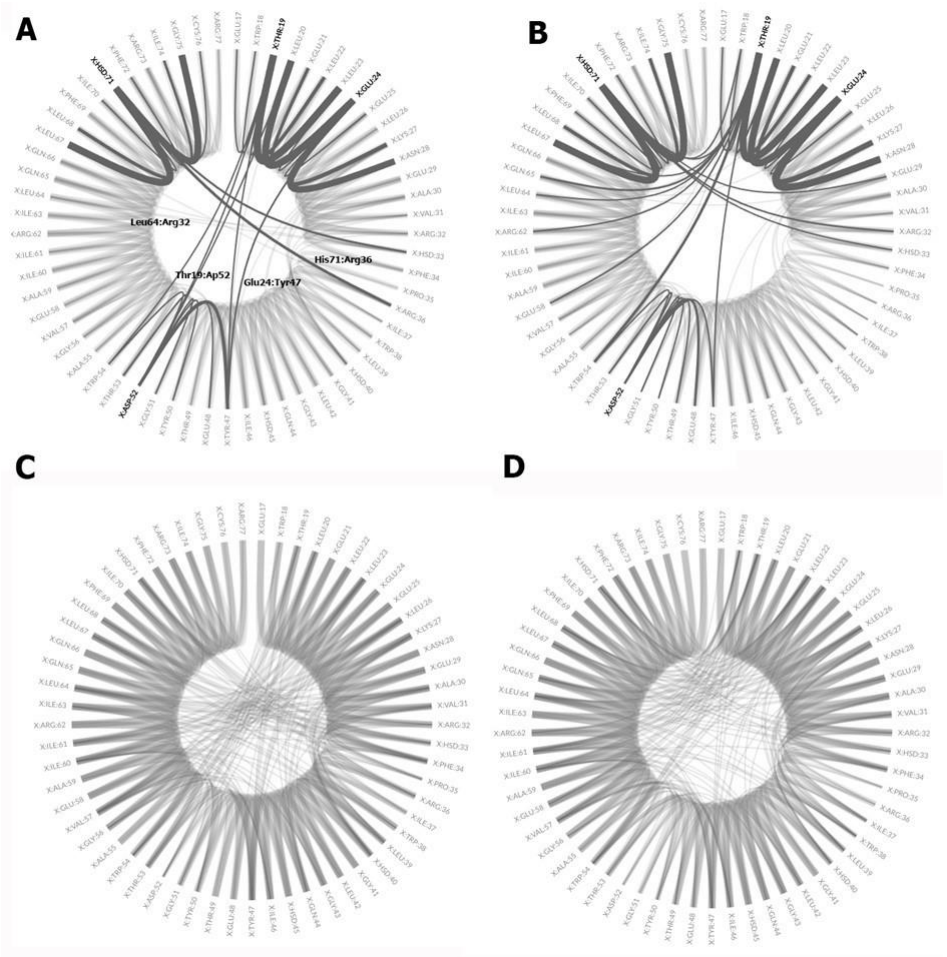

Figure 8: Intra-molecular contact analysis plot. Hydrogen bonds for A) the vertical and B) the horizontal systems and hydrophobic contacts for C) the vertical and D) the horizontal system. Important contacts are highlighted in bold. For the hydrogen bond contacts the donor-acceptor threshold distance was set to 3.5 Å and the angle to 120°. For the hydrophobic contacts, the following criterium was chosen:

$$|AB| < R_{vdw}(A) + R_{vdw}(B) + 0.5 \text{ Å}$$

Where 'A' and 'B' are the two participating atoms and Rvdw is the van der Waals radius of the atoms.

1.2 Exploring Conformational Dynamics in HIV-1 Nef Potential Pockets to Enhance Drug Design Strategies

In order to design drugs against a specified pocket of a protein, in depth details of the conformational dynamics of that pocket is required. First, to identify potential drug targets on Nef, we utilized DeepSite and FTMap. We focused on three pockets (**Figure 9, Table 1**) with the highest DeepSite score within the Nef core region (amino acids 79-153 and 184-201) (**Figure 12**).

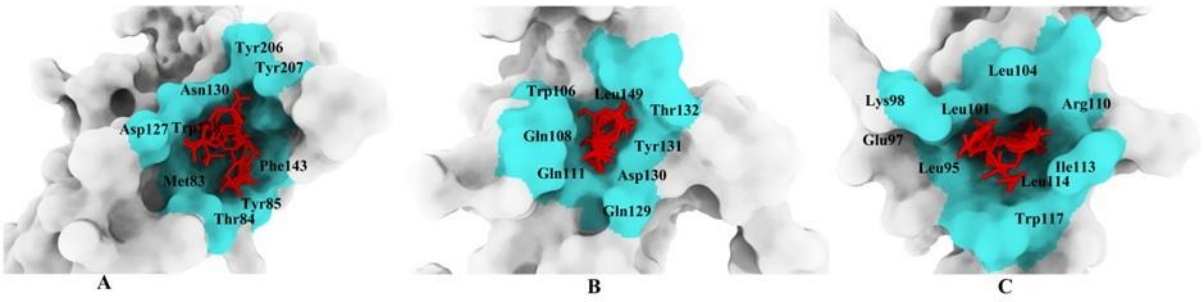

Figure 9: Three highest-ranking pockets as predicted by DeepSite and FTMap : A) Pocket 1, B) Pocket 2, and C) Pocket 3. We have highlighted the pocket grooves in cyan and identified key pocket residues. The FTMap probes are illustrated in red.

Table 1: Details of the three predicted pockets on Nef. Probe density is calculated as bound probes at the specified pocket/Total no. of probes.

Pocket Id	DeepSite score	FTMap probe density	Pocket lining residues
Pocket 1	0.93	0.3	Met83, Thr84, Tyr85, Asp127, Trp128, Asn130, Leu141, Thr142, Phe143, His197, Tyr206, Tyr207
Pocket 2	0.89	0.23	Trp106, Gln108, Gln111, Gln129, Asn130, Tyr131, Thr132, Pro133, Gly134, Arg138, Leu149
Pocket 3	0.93	0.29	Leu95, Lys96, Lys98 Gly99, Gly100, Leu101, Leu104, Arg110, Gln111, Ile113, Leu114, Trp117, trp187

Next the conformational dynamics of each of these pockets are assessed from 20 independent MD simulations of monomeric apo-Nef (total 2μs). Among the identified pockets, Pocket 3 emerges as the most promising candidate due to its remarkable inherent stability (**Figure 10)**.

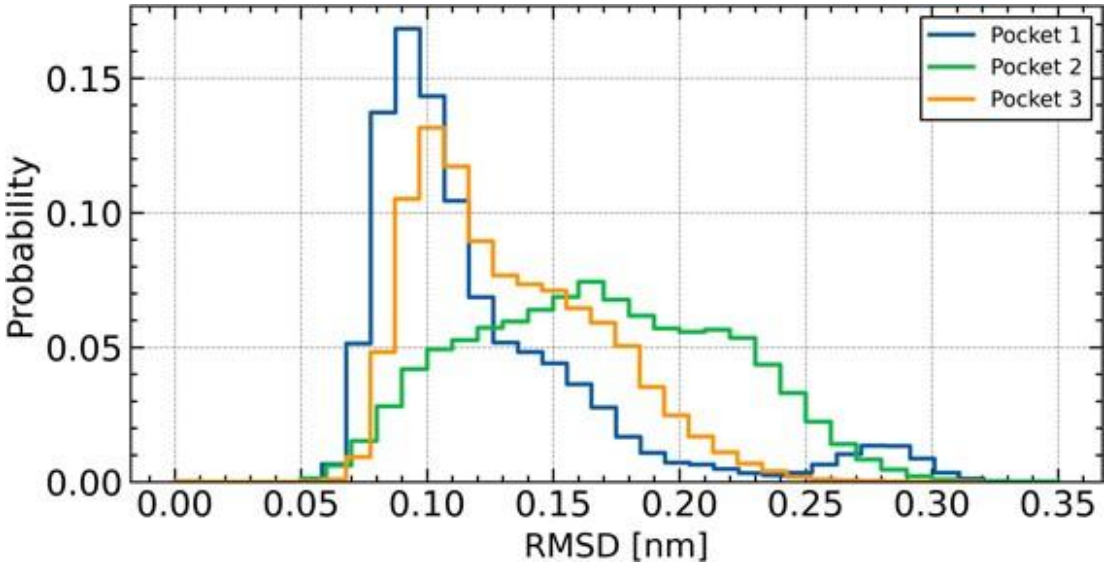

Figure 10: RMSD probability histogram of the top three pockets. Pocket 3 is the most stable pocket with very low mean backbone RMSD of 1.5Å.

Pocket 3 also plays a crucial role in the homo-dimerization process, forming essential contacts which are depicted in **Figure 11**.

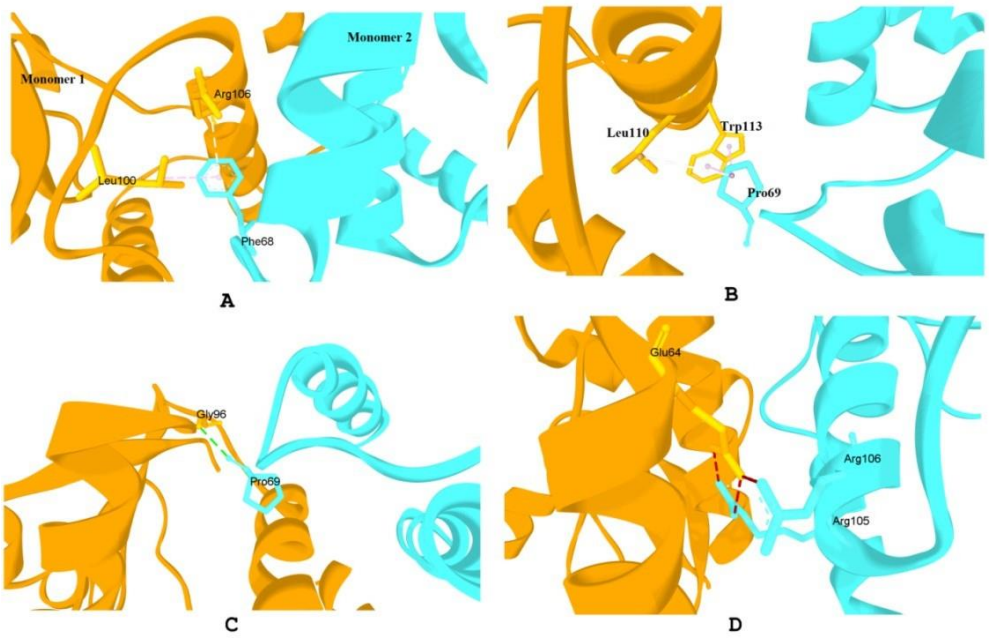

Figure 11: Important Nef dimer forming contacts (PDB id: 6B72) between two monomers (orange and cyan) involving pocket 3: A) Two Pi-alkyl contacts; B) Three Pi-Alkyl contacts; C) An hydrogen bond contact; D) Three salt bridge contacts.

The loop region of Nef produces substantial flexibility as indicated by the RMSF plot (**Figure 13**). We projected the conformational landscape of the Nef core along the first four PC combinations (**Figure 14**). To assess the stability of the PCA-extracted structures, we superimposed them to other Nef structures available in the Protein Data Bank (PDB). The results indicate a significant similarity between the PCA extracted structures and existing Nef structures, with mean RMSD values consistently at or below 2.0 Å (**Figure 15**).

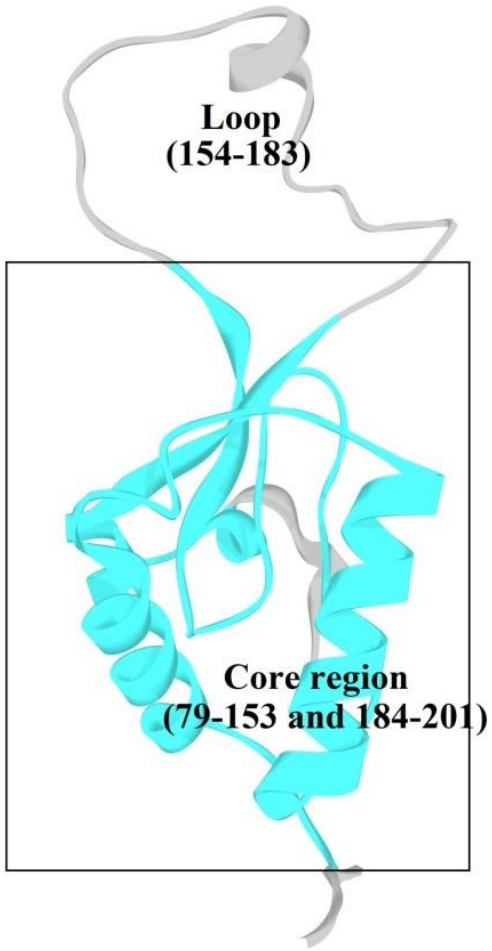

Figure 12: Nef core region (cyan) and loop region (grey).

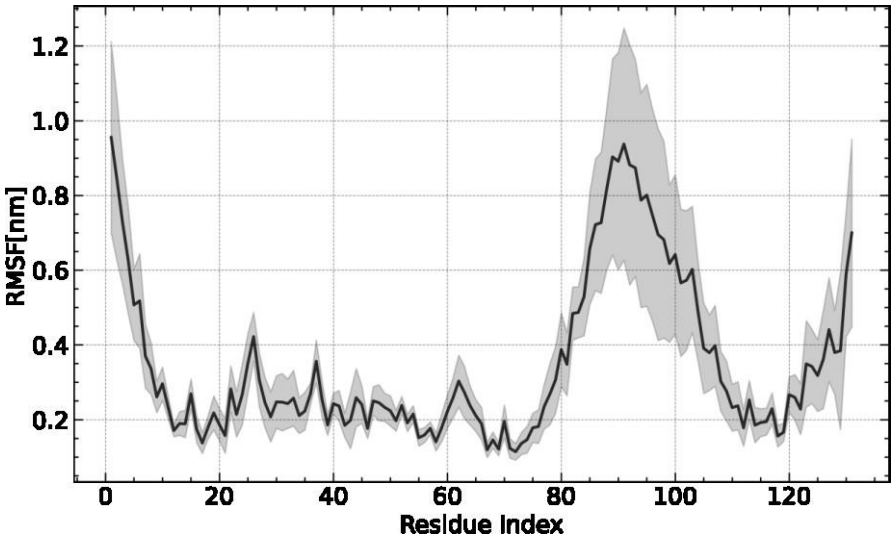

Figure 13: Root mean square fluctuation (RMSF) plot with standard deviation drawn from concatenated 20 independent MD trajectories.

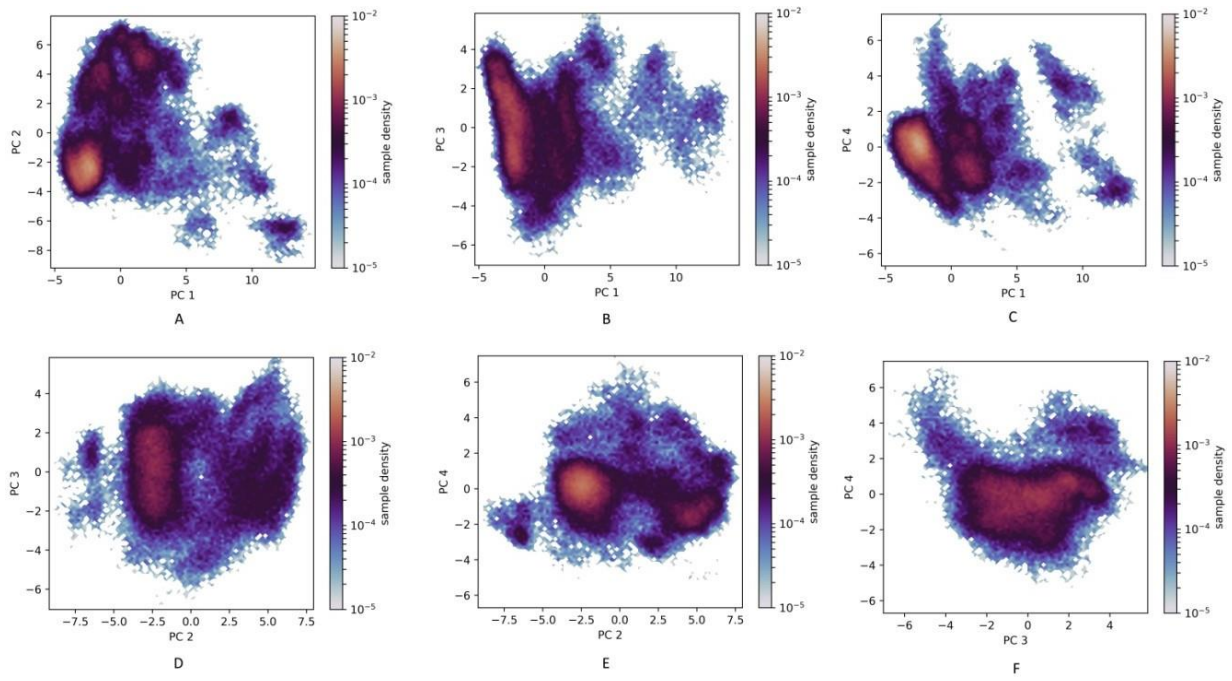

Figure 14: PCA density plots of first four PC combinations: A) PC1 vs PC2; B) PC1 vs PC3; C) PC1 vs PC4;D) PC2 vs PC3; E) PC2 vs PC4; F) PC3 vs PC4. Representative structures were taken from high-density regions and a random structure was taken from the low-density region of PC1 vs PC2.

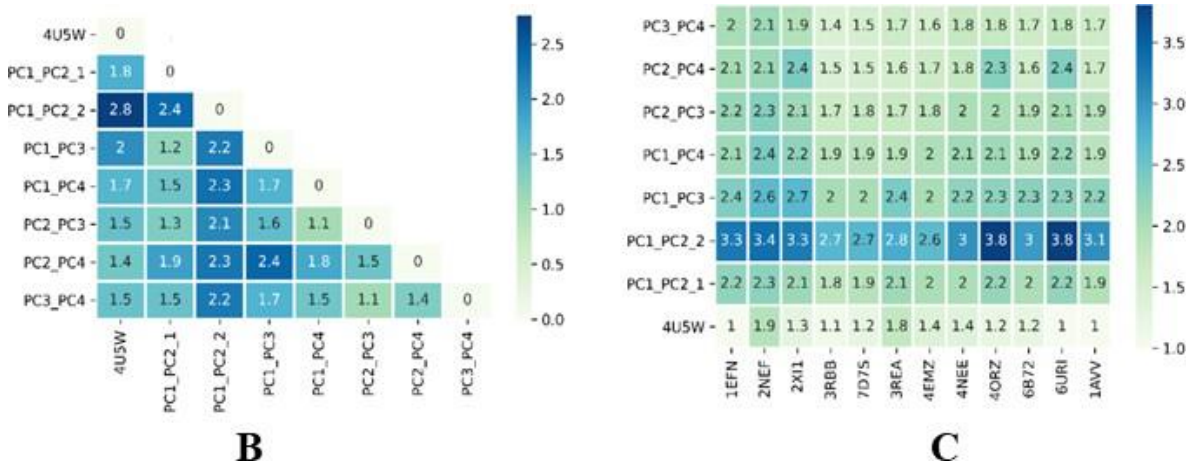

Figure 15: B) Intra RMSD values (backbone atoms) of PCA extracted Nef structures and C) RMSD values between PCA extracted structures and available Nef models from the PDB database.

Pocket 3, despite some flexibility in the backbone of lining residues, overall remain stable during the simulations. In the context of PDB entry 4UW5, the involvement of Gly100, Glu97, and Phe94 in creating backbone hydrogen bonds with a water molecule (**Figure 16**) adds an intriguing aspect to potential interactions in this pocket.

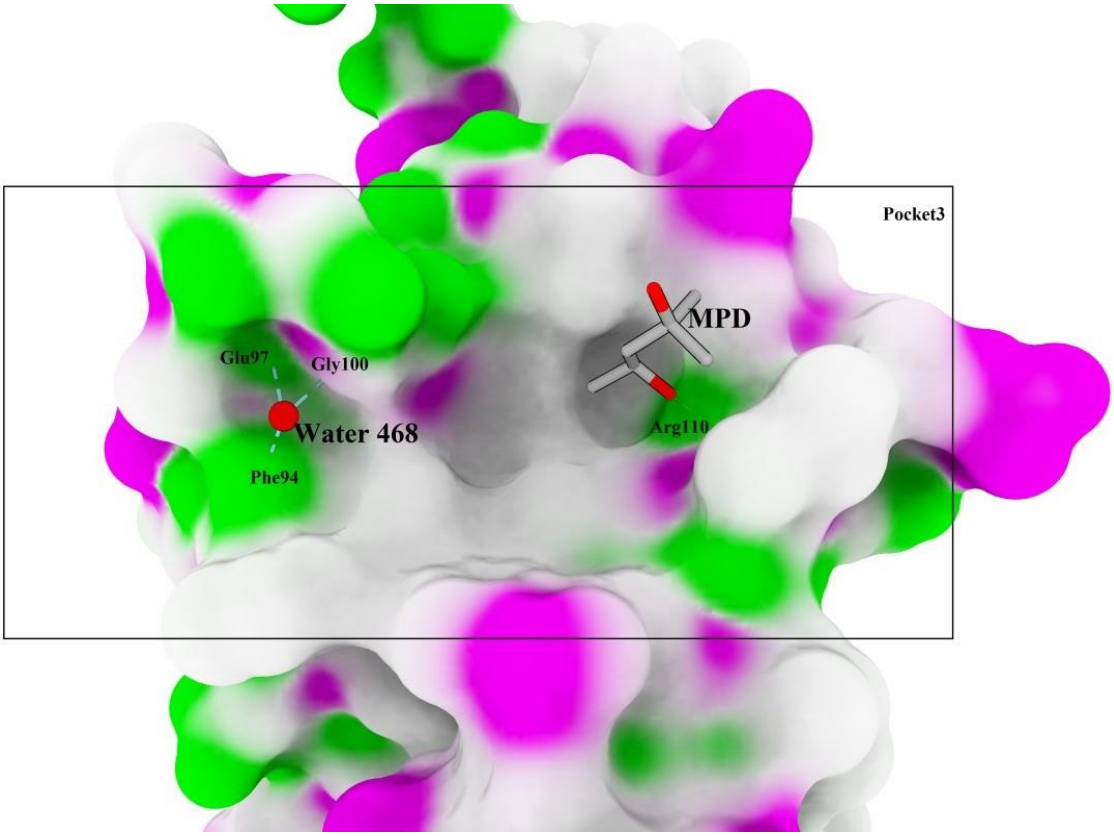

Figure 16: Position of water, (4S)-2-methylpentane-2,4-diol (MPD) inside pocket 3. The protein surface is colored according to the H-bond donor or acceptor characteristic. Residues forming H-bond with the former are labeled.

Objective 2: **Studies on membrane association mechanisms of HIV-1 accessory proteins and elucidating the process of membrane channel formation**

HIV-1 Vpu is an extensively studied viroporin with ion channel activity. Various molecular dynamics (MD) simulation studies have consistently shown that the native Vpu forms pentameric ion channels within the lipid bilayer. These channels are stabilized by robust hydrophobic interactions among the individual monomers. The structure of Vpu has been elucidated in its membrane-compatible conformation (PDB Id: 2N28), providing detailed insights into both its cytosolic and transmembrane components. In contrast, Nef and Vif, despite loosely interacting with the membrane through their disordered N-terminal myristoylation and C-terminal domains, respectively, primarily exert their functional activities within their globular cytoplasmic domains. The disordered membrane-interacting segments of Nef and Vif lack inherent functional roles and do not form any oligomers within the membrane bilayer, hence extensive studies on these domains may not be crucial for therapeutic interventions. While Vpr exhibits versatility as a cytoplasmic protein with diverse functions, it also demonstrates the intriguing capability to interact with membranes and form cation-selective ion channels. However, the specific structural details governing these interactions remain elusive. For Vpr to assume an ion channel-compatible conformation within the bilayer, it must undergo significant conformational changes, which have not been previously characterized. The novel conformations of Vpr, observed in this study, play a pivotal role in comprehending neuronal cell death associated with HIV-1-associated dementia. Therefore, the extensive study of the Vpr protein is driven by its crucial role in pathogenic ion channel function.

2.1 Prediction of the C- and N-terminal helices orientation in lipid bilayer

To determine the topological orientation of the C_helix and N_helix in the lipid bilayer, we used TMHMM server which revealed that residues 55-76 are highly likely to be part of the potential transmembrane region, in line with predictions made by HMMTOP. In order to validate the sequence based findings, we conducted coarse-grained molecular dynamics (CGMD) simulations to study the relative positioning of the N_helix and C_helix within a lipid bilayer. We placed the helices within a random mixture of CG lipids and water beads to mimic bilayer formation. The bilayer thickness was computed to 36 Å for both systems, consistent with prior findings [59]. During the simulations, the C_helix consistently remained embedded within the membrane, while the N_helix oriented itself at the interface between

lipids and water (**Figure 17**) exhibiting its amphipathic nature, consistent with prior experimental observations [60]. Similar results are replicated when we conducted the same CGMD setup with POPC and POPE lipids in a ratio of 1:4.

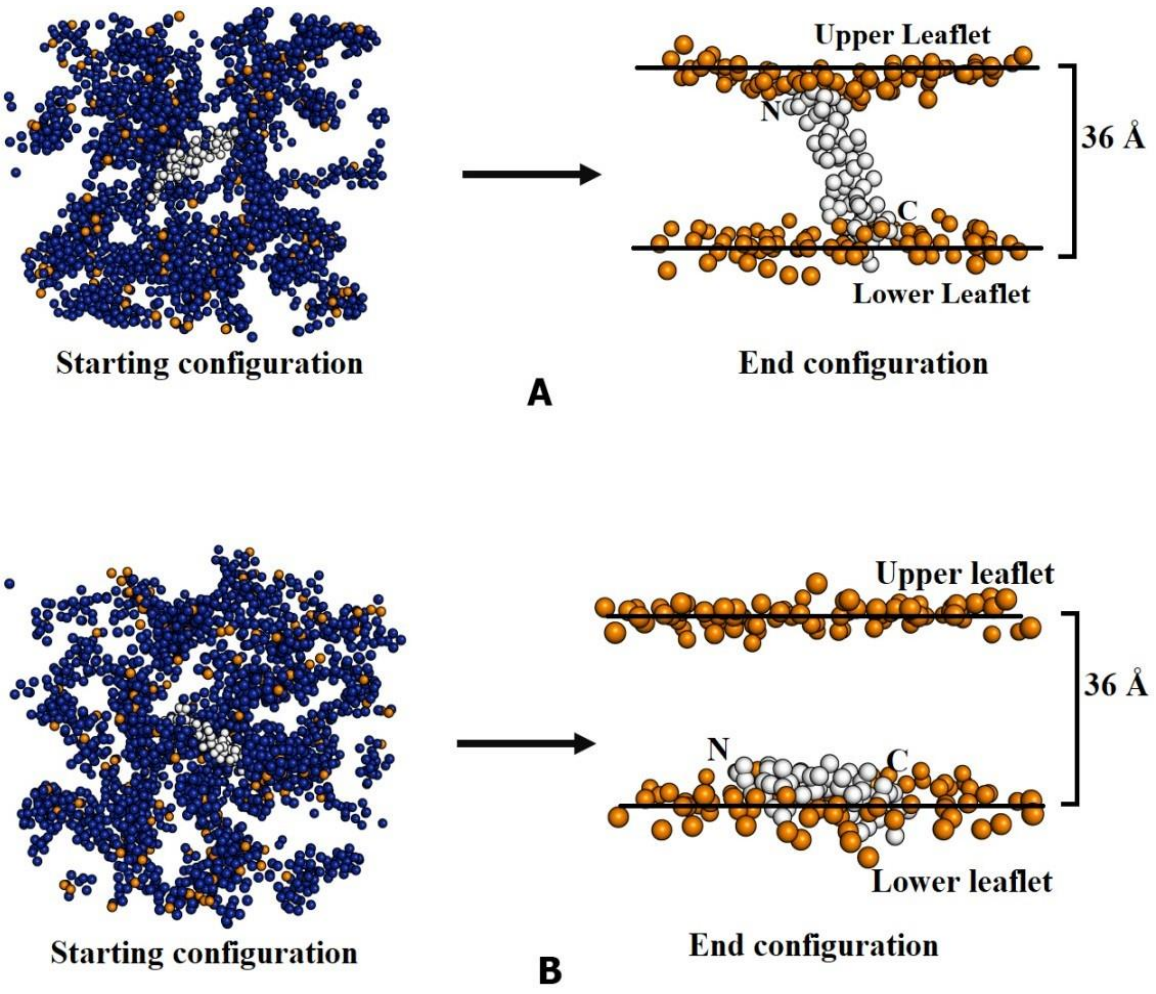

Figure 17: Coarse grain bilayer self-assembly simulation of A) C_helix and B) N_helix system. Blue beads are CG water molecules, Orange beads are lipid phosphate head groups and White bonded beads are Vpr helices.

2.2 Modelling the Ion channel conformation

We conducted PCA of the C_helix conformations from both the full-length Vpr trajectory (**Figure 18B**) and the C_helix trajectory (both POPC and DPPC, **Figure 18A**). Representatives from both trajectories were very similar, and as a result, we selected the C-helix representation from the latter set of simulations to use as a monomer in predicting the

multimeric Vpr channel. We utilized a standalone version of HSYMDOCK to generate multimeric channel models, ranging from tetramers to heptamers. Two distinct sets of conformations were constructed (**Figure 19**). In the first set (conformation 1), we applied selective restraints so that polar residues were exclusively positioned within the channel pore, creating a polar inner lining. In the second set (conformation 2), we employed the default parameters of HSYMDOCK, allowing multimer formation without imposing any restraints. In both cases, we selected the top-scoring models for subsequent molecular dynamics (MD) simulations.

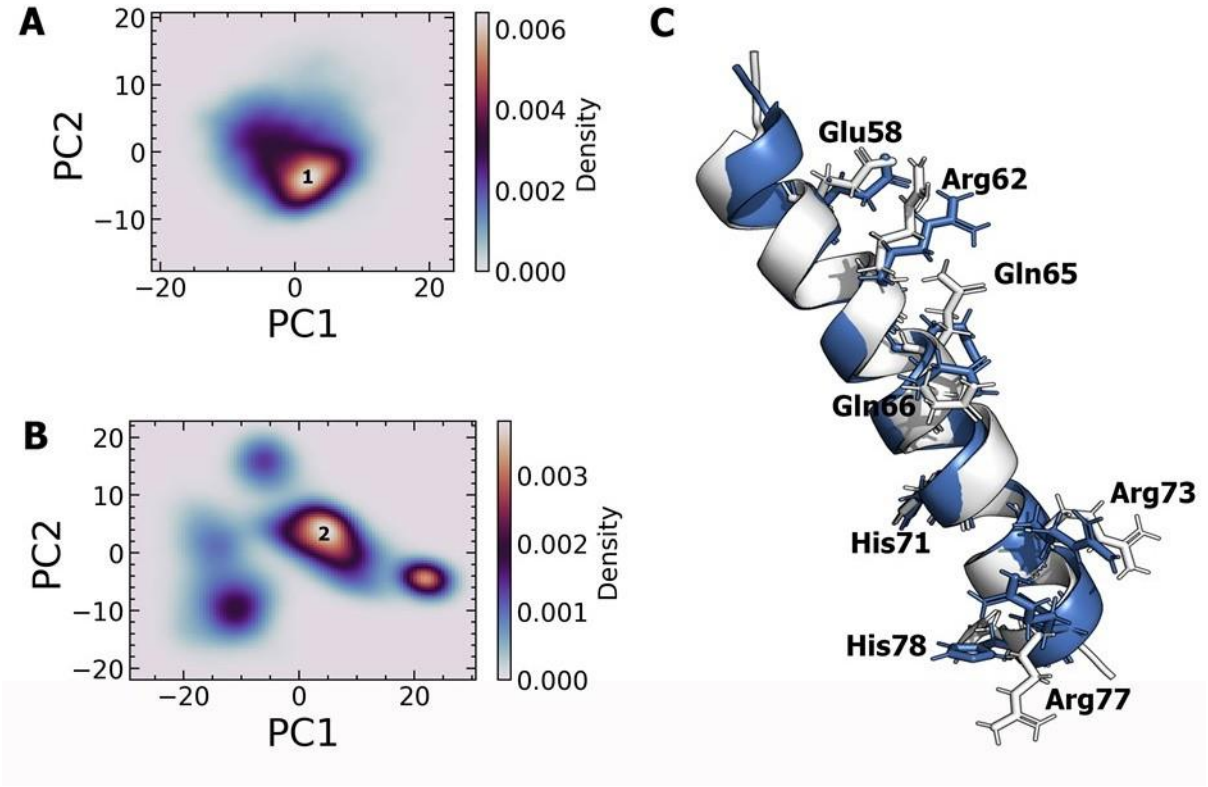

Figure 18: PCA density plot from the concatenated trajectories of A) C_helix from both POPC and DPPC system and B) C_helix derived from the whole Vpr simulation. C) Superimposition of the conformations extracted from point 1 (white) and point 2 (blue) of the PCA plot.

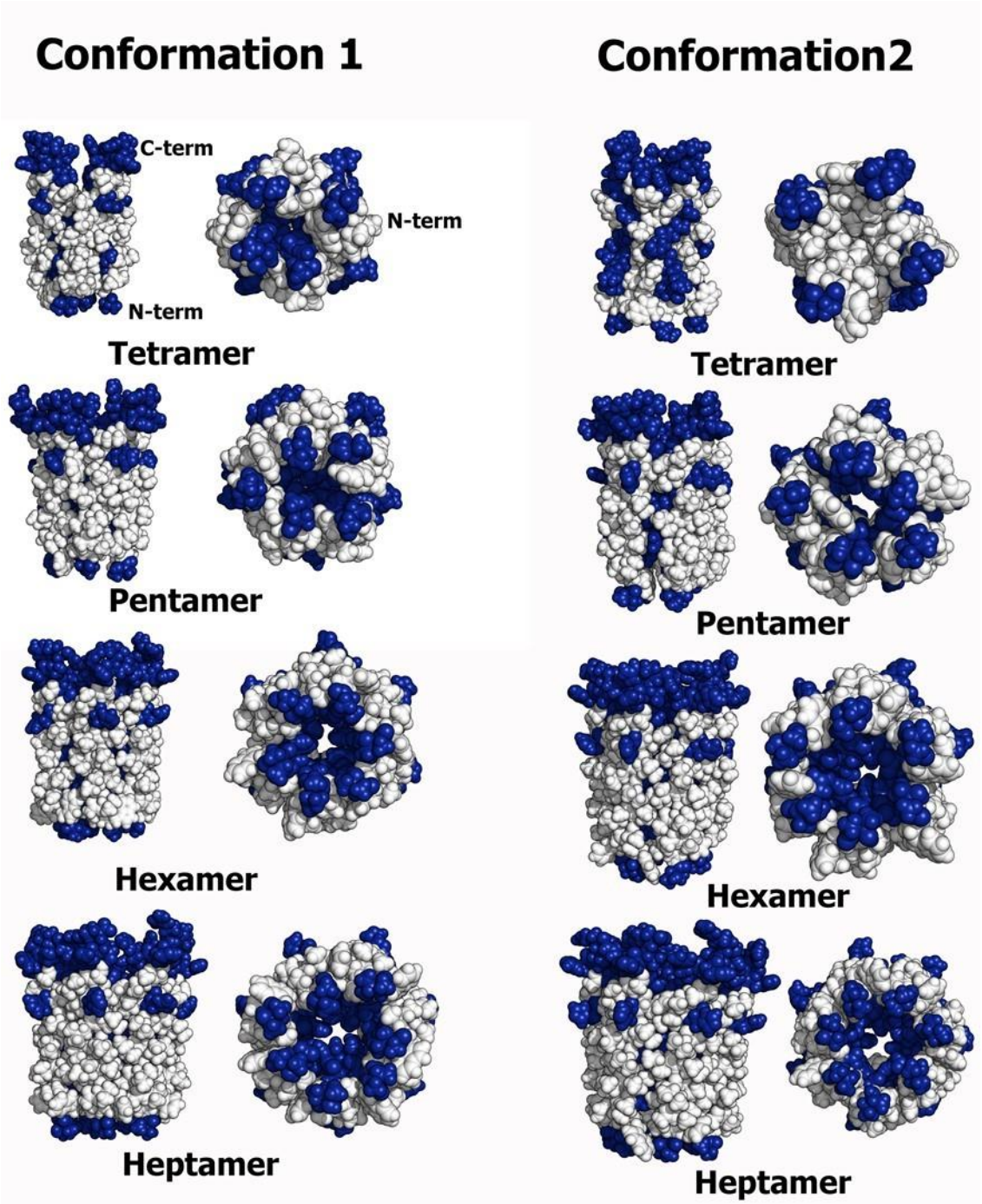

Figure 19: Initial channel models predicted using HSYMDOCK. In each model, the polar residues are colored as blue spheres and hydrophobic residues are colored as white spheres. The polar residues are restrained inside the channel pore in conformation 1, while in conformation 2 no constraints were imposed and default parameters of HSYMDOCK are used. The left-hand panels are the N-terminal orthoscopic top views of A) tetramer, B) pentamer, C) hexamer and D) heptamer. The right-hand panels are the lateral side views of E) tetramer, F) pentamer, G) hexamer and H) heptamer.

In the first set of models, excluding polar residues from multimer interfaces, only the tetramer and pentamer show a C_helix tilt along the Z axis, consistent with previous MD simulations. In contrast, the second set of models displays this tilt in all multimers. Interestingly, the heptameric channel exhibits a similar polar inner lining prediction in both sets, not seen in lower oligomeric forms, suggesting a preference for a hydrophilic channel core in higher oligomeric models. It's worth noting that not all ion channels have a hydrophilic core; some have hydrophobic residues inside. Recent MD simulations indicate that Vpu forms a pentameric channel stabilized by van der Waals interactions [61], potentially serving as a reference for arranging multiple Vpr monomers. We then computed the possible conformations of Vpr channel models by placing them in a POPC lipid bilayer and subjected to a 300 ns MD simulation in triplicate. We assessed structural stability by calculating the RMSD of backbone atoms. Most multimeric models had high RMSD values (> 3.5 Å in all cases) (**Figure 20**). The tetrameric Vpr conformation 2 displayed the highest stability throughout the MD simulations (2.84 ±0.37 Å). The pentameric models manifested a plateau (in two out of three replicas) within the range of 4.0-4.5 Å after 200 ns. These plateaus indicate the attainment of stable, reoriented channel conformations. Both hexameric models exhibited comparably low mean RMSD values (3.60±0.46 Å and 3.28±0.65 Å, for conformation 1 and 2 respectively), while the heptameric conformation 2 (Figure 8H) displayed a relatively lower mean RMSD than conformation 1.

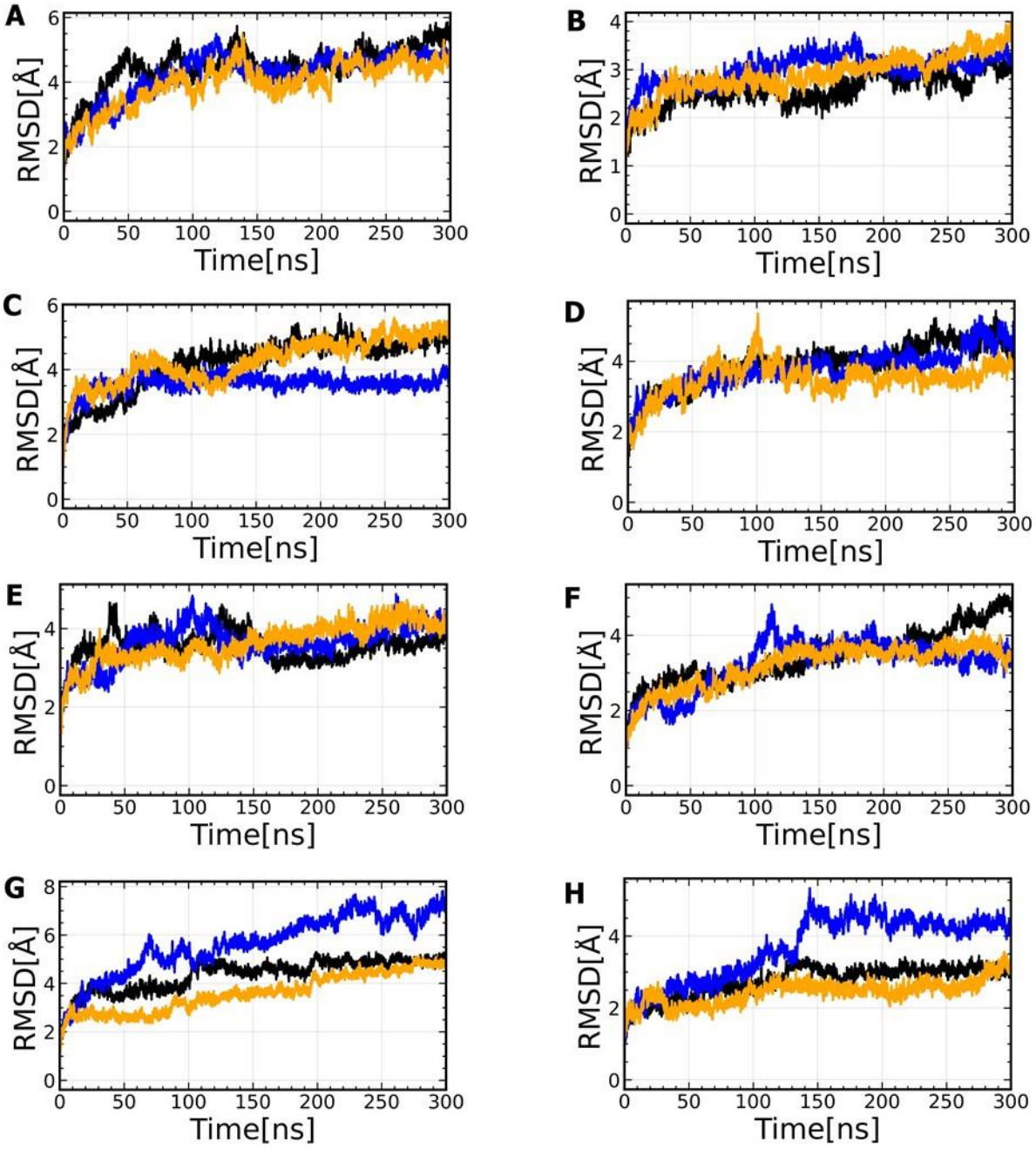

Figure 20: RMSD of the backbone atoms of A) tetrameric, C) pentameric, E) hexameric, G) heptameric channel from conformation set 1 and B) tetrameric, D) pentameric, F) hexameric , H) heptameric channel from conformation 2 during simulation. All the simulations were run in triplicate (black: replica1, blue: replica2 and orange: replica 3).

Objective 3: Investigation of selectivity mechanism and conductivity of ion channels formed by HIV-1 accessory proteins

To investigate ion conductance through the C_helix channel, the density map of water within each channels' pores **(Figure 21**) and the electrostatic potential surface of each oligomer are calculated (**Figure 22, 23**). It was found that the pore of both tetrameric models was impermeable to water molecules (**Figure 21A**) due to its very small pore size. On the other hand, both conformations of the pentameric models exhibited significant water densities, with termini and central regions well hydrated and overall compatible with a multistep mechanism of transport for ions

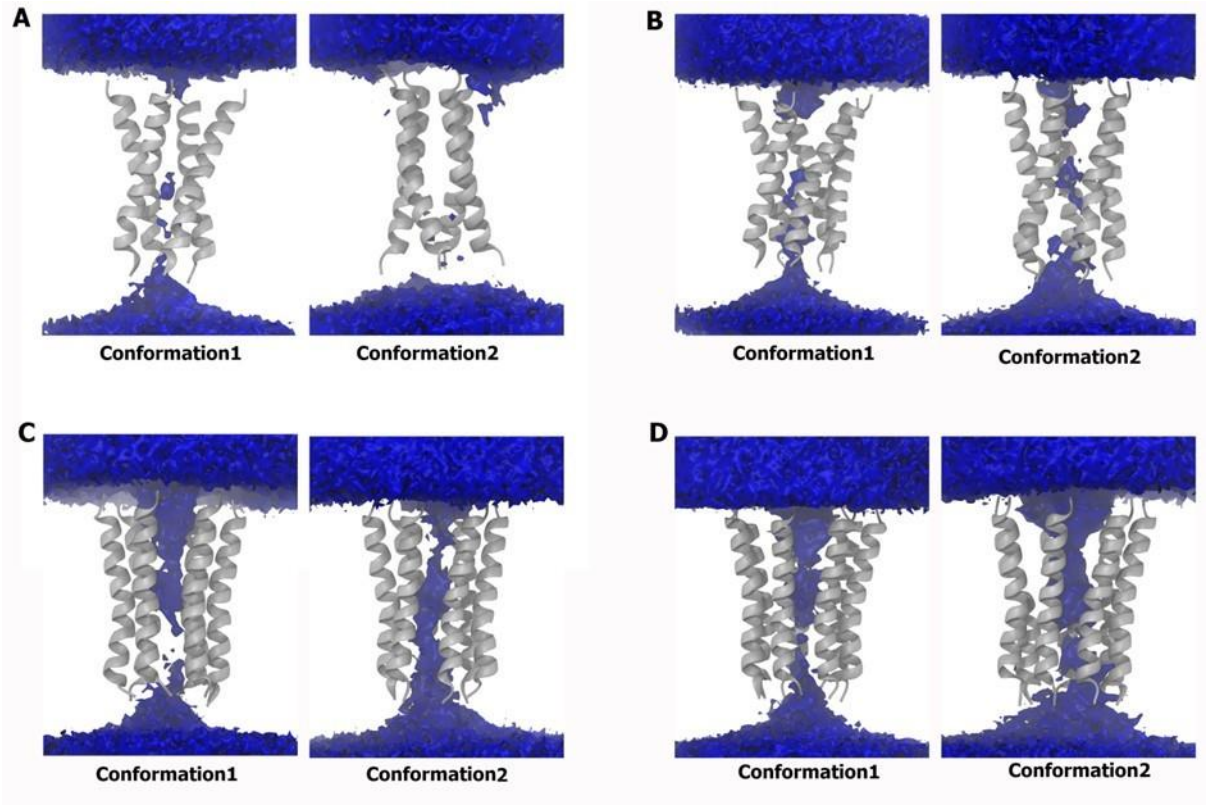

Figure 21: The water density map of the oligomers, calculated using all three replica MD simulations. A) Tetramer, B) Pentamer, C) Hexamer, D) Heptamer. The densities are superimposed to the initial structures with isovalue set to 0.07. Water is represented in blue solvent and the protein is represented in cartoon format.

We identified the most stable channel configurations by projecting the last 150 ns of the trajectory onto the first two principal components (PCs) and selected representative states from the high-density region. We then computed the electrostatic potential of these representative channel structures using the Poisson-Boltzmann (PB) equation (**Figure 22,**

23). Notably, in the pentameric and hexameric channels of conformation 2, there is a negative electrostatic potential on the solvent-exposed surface in the C-terminal region, suggesting a potential role as an electrostatic cation selectivity filter. In contrast, conformation 1 displays negative potential spots on the N-terminal surface due to the presence of Glu58. This positioning of Glu58 is relevant to calcium ion selectivity. Both sets of conformations exhibit a mixed potential on the channel's inner lining and a predominantly hydrophobic surface facing the membrane, consistent with previous MD simulation findings. Additionally, there is a gradient of electrostatic potential from the N to C-terminal region, indicating the channel's orientation within the lipid bilayer. According to the electrostatic all the conformation 2 oligomers' C-termini were associated with a negative potential, which may function as a cation selectivity filter that facilitates the first stage of cation binding. It is reported that in Ca^{2+} channels, glutamate residues at the channel termini are involved in Ca^{2+} selectivity [62]. In both the pentameric conformations, the N-terminal potential surface reveals areas with negative potentials attributed to the existence of Glu58. But in the pentamer of conformation 2 (**Figure 23B**), the Glu58 faces the channel pore whereas the negative charge on the C_terminal end creates a site for the accumulation of cations. Similarly, we identified a distinct negative patch at the C-termini, in the hexameric and heptameric models of both conformations but they are radiated out of the pore (**Figure 22C, D**) thus reducing the possibility of a cation docking site. In the tetrameric model of conformation 2, Glu58 faces towards the bilayer rather than the pore surface and the small pore size does not allow any water molecules in the center of the pore. The influenza virus M2 channel (PDB ID: 6PVR) presents interhelical Arginine-Aspartate salt bridges at the C-terminal of the pore. Vpr instead bears the aforementioned glutamates in place of aspartates at N-termini, which in our models are also predicted to interact with arginines in the pentameric oligomer. The longer glutamate side chain would be consistent with a pentameric tertiary arrangement of Vpr, compared to the tetrameric, more compact, M2 channel. Moreover, the M2 channel has glycine residues facing the pore, alongside short side chain residues like alanine and serine. A study showed that during the transport of K^+ through KcsA K^+ channel, in the absence of water, carbonyl oxygen atoms within the selectivity filter create a cage around the K^+ binding sites to mimic the waters of hydration [63]. In our pentameric model, glutamine residues would protrude into the larger pore and favor cation transport, as suggested by the water cluster analysis (**Figure 21B**). The water molecules in the center of the pore can create the required hydration for the cations in order to transport successfully. Previously, MD simulations proposed that water molecules coordinate the passage of K^+ ions through the pore of rat Kv1.2 voltage-

sensitive K^+ channel [64]. The electrostatic potential surface of the M2 channel is somewhat comparable with the pentameric model

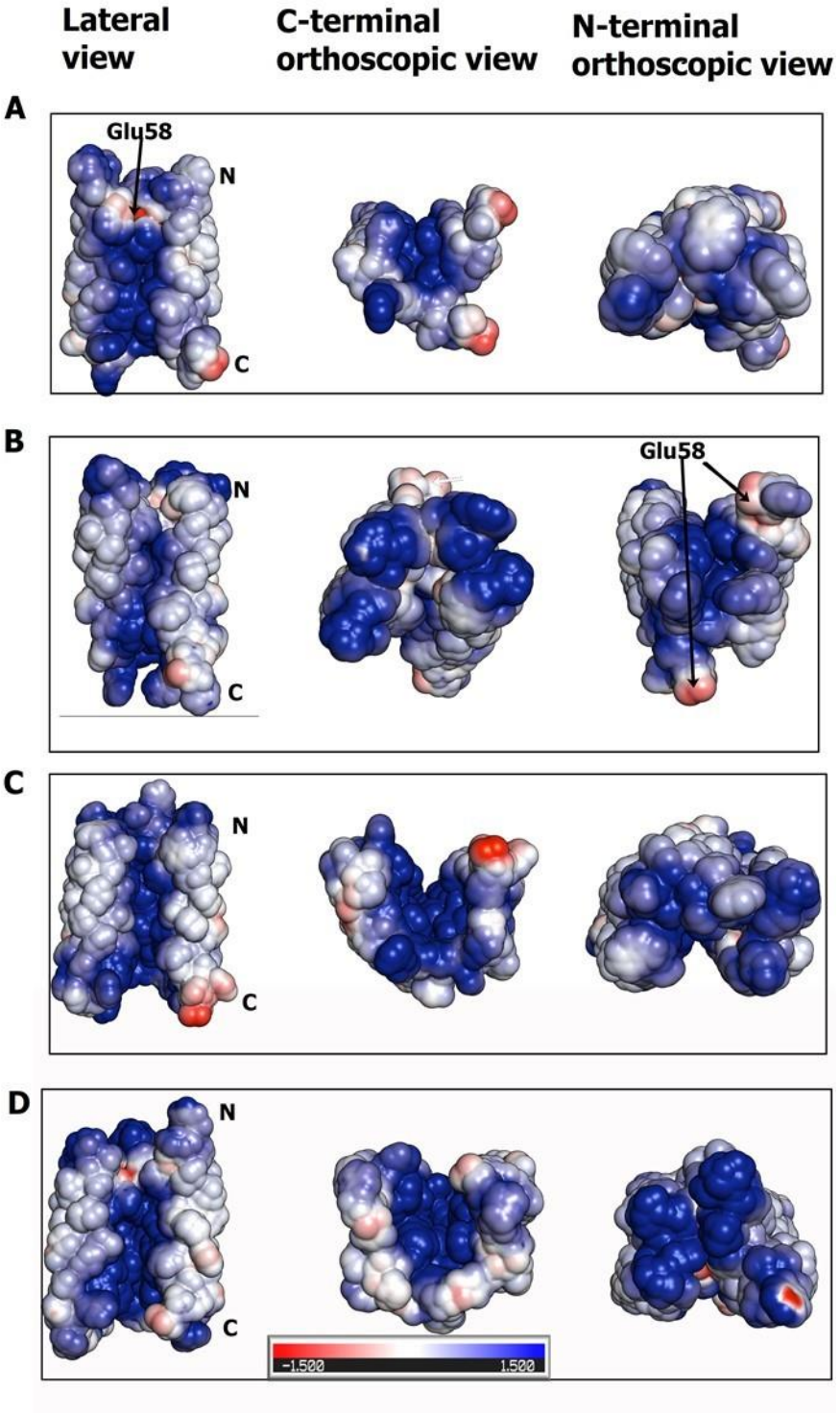

Figure 22: Predicted potential energy surface of the representatives of channel models from conformation 1 calculated by solving the Poisson-Boltzmann equation. A) Tetramer, B)

Pentamer, C) Hexamer, D) Heptamer. For better visualization of the pore lining electrostatics a monomer is removed.

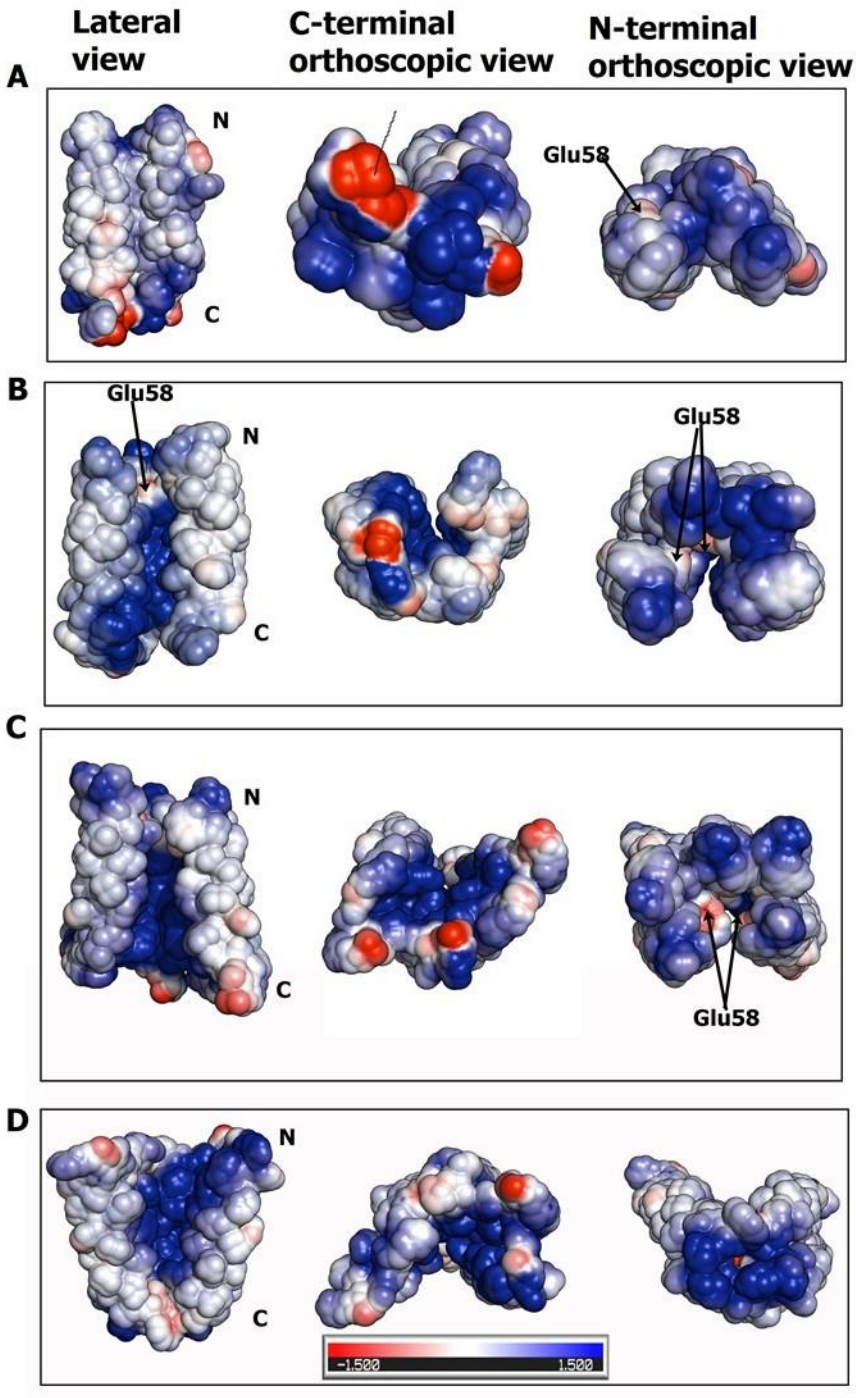

Figure 23: Predicted potential energy surface of the representatives of channel models from conformation 2 calculated by solving the Poisson-Boltzmann equation. A)Tetramer, B) Pentamer, C) Hexamer, D) Heptamer. For better visualization of the porelining electrostatics a monomer is removed.

Objective 4: Identification of suitable small molecules that may act as potential HIV-1 accessory protein inhibitors

4.1 Exploring the interaction mechanism between Viprinin and its morpholine and piperidine derivatives with HIV-1 Vpr

4.1.1 Docking simulation of Viprinin, ViprininD1 and ViprininD2 with Vpr

Viprinin and its two derivatives were docked in the Vpr docking site in triplicate and took the top docked poses(**Figure 24**). The docking energies (scores) aligned with previous experimental results [65], showing ViprininD1 and ViprininD2 as more effective Vpr inhibitors.

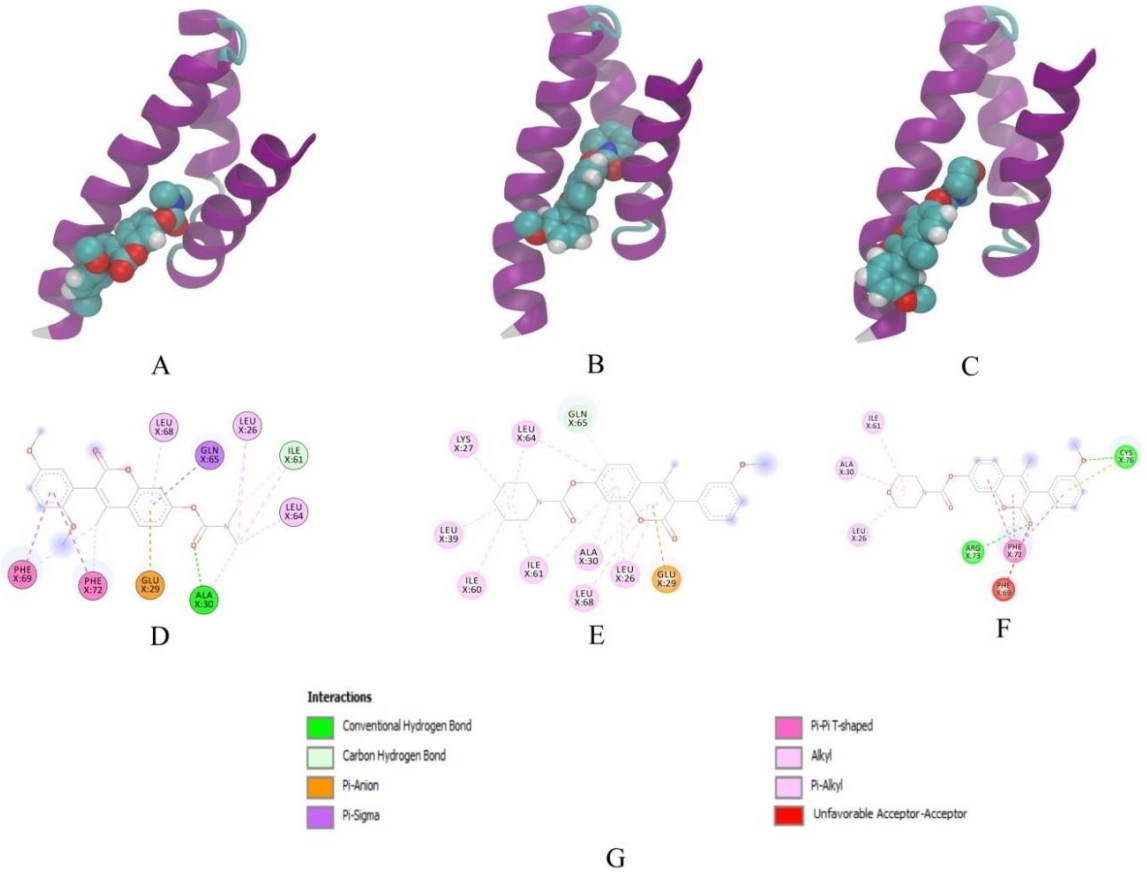

Figure 24: A) Top docked pose of Viprinin (-6.31 Kcal/mol), **B**) ViprininD1 (-7.7 Kcal/mol), and **C**) ViprininD2 (-6.99 Kcal/mol). **D)** Viprinin formed a hydrogen bond with Ala30 and 12 hydrophobic interactions. **E)** ViprininD1 had no H-bond but formed 14 hydrophobic contacts. **F)** ViprininD2 formed two H-bonds and eight hydrophobic interactions but had an

unfavorable acceptor-acceptor interaction G) The color-coded key provides information about the types of interactions observed.

4.1.2 MD Simulation of Vpr-ligand complexes

Multiple simulation runs were conducted for better reliability of the computed metrics. We used abbreviations for convenience, designating Vpr protein bound with Viprinin, ViprininD1, and ViprininD2 as Vpr_V, Vpr_V1, and Vpr_V2, respectively, focusing on backbone atoms only. ViprininD1 induced substantial structural deviations in Vpr backbone (**Figure 25B**). Two runs showed partial unfolding of helix 2 and bending of α-helix 3 (**Figure 26A, B**) as depicted from secondary structure analysis. RMSD values showed distinct patterns in the Vpr backbones of all complexes. Vpr_V1 had a higher RMSD value compared to Vpr, Vpr_V, and Vpr_V2 indicating different convergence patterns. RMSF value (of all Vpr backbones indicates that the N-terminal (Glu17-Glu21) and C-terminal residues (Ile74-Arg77) exhibit high fluctuations (**Figure 27**).

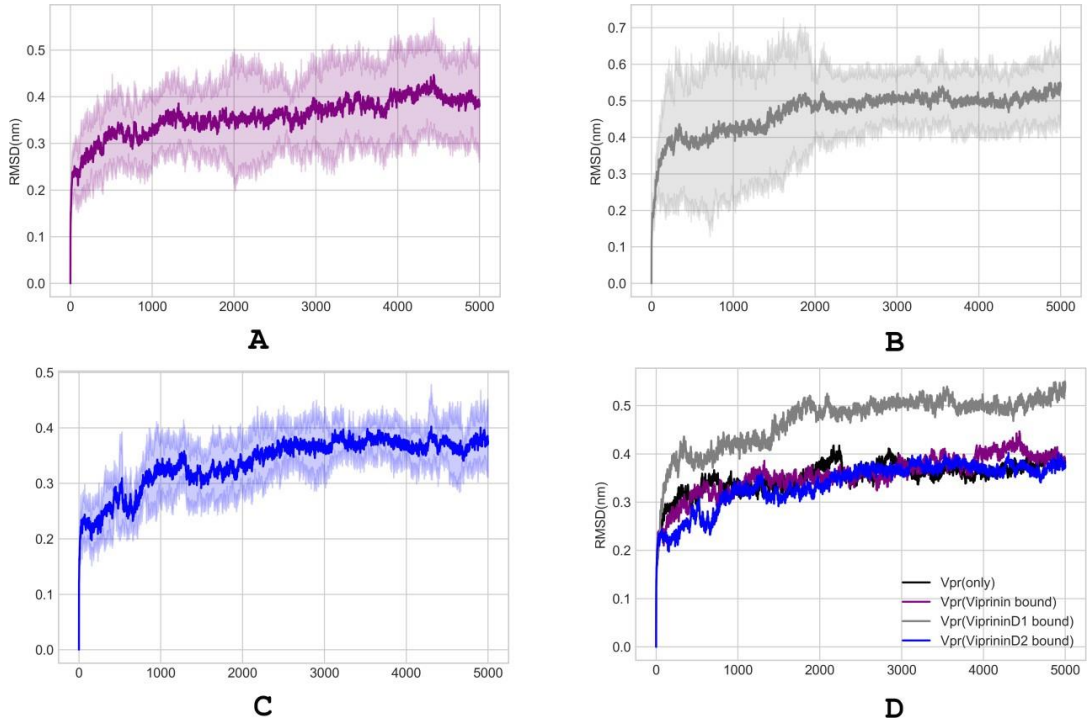

Figure 25: Figure D displays the RMSD data with associated error values for the Vpr backbone when it is bound to Viprinin (A), ViprininD1 (B), and ViprininD2 (C), as obtained from seven independent replicas. These RMSD values are graphed in comparison to the

RMSD values of the free Vpr backbone (D). The X-axis in all plots represents the number of frames.

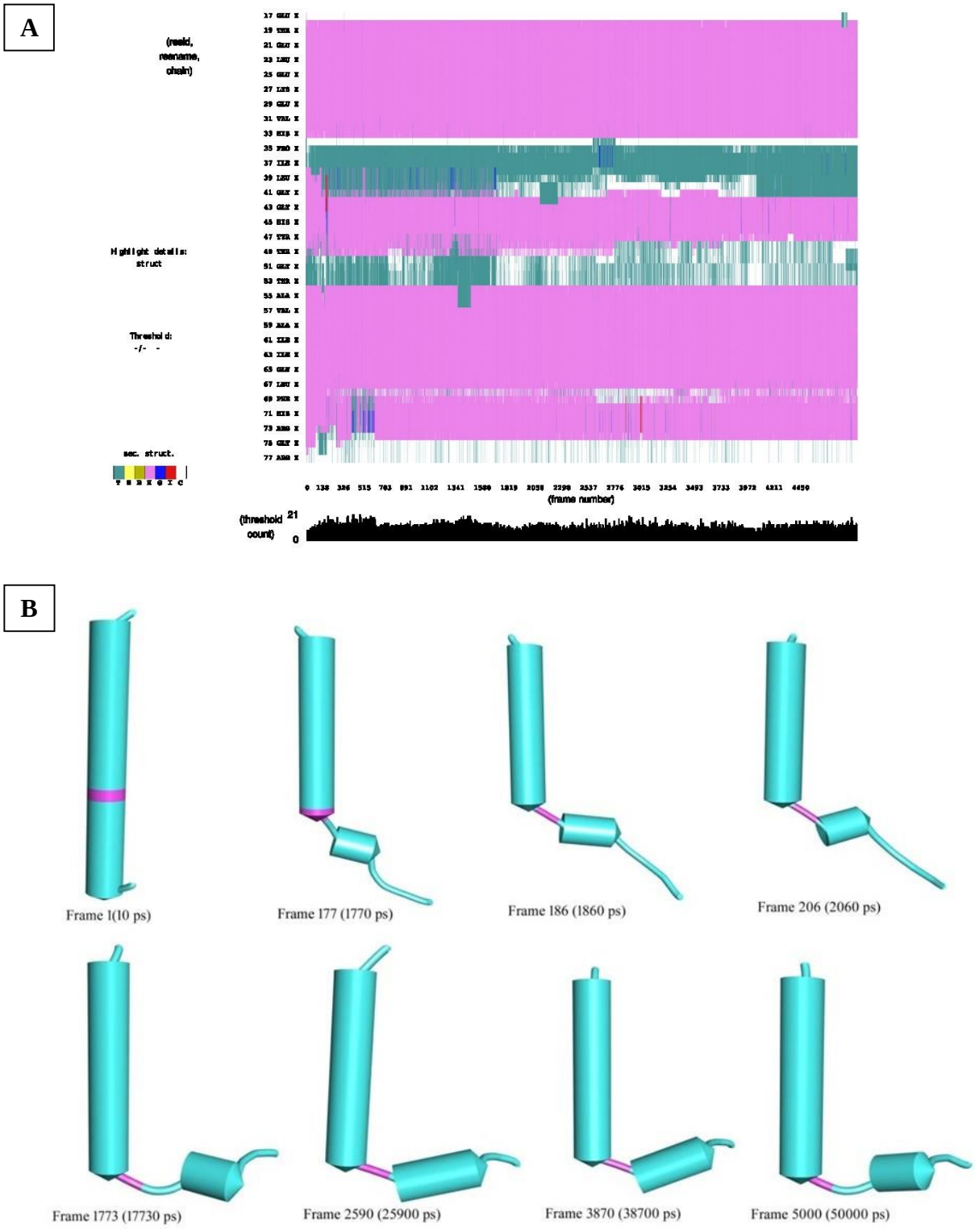

Figure 26: **A)** Secondary structure of Vpr during simulation. It can be noted that during simulation part of Helix-2 (38-50) unfolds into Turns and coils (replica 1). **B)** Vpr helix 3 at

different time points of the simulation (from replica 1). Helix is represented as Tube and the Pink colored residue is Leu68.

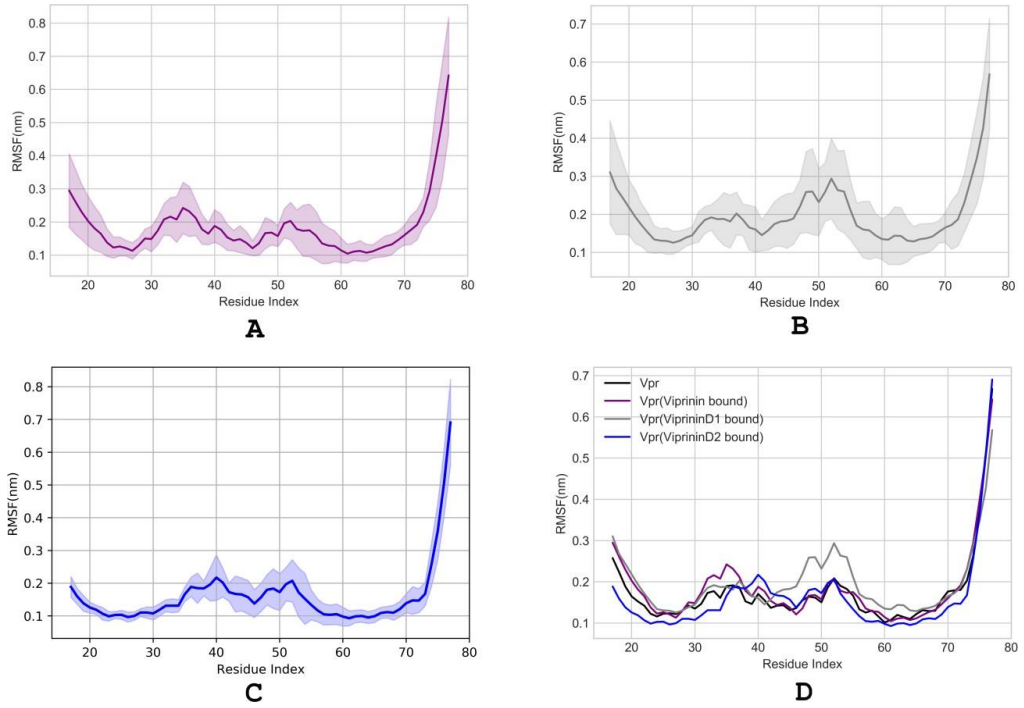

Figure 27: RMSF plot (mean value from seven independent runs) of Vpr backbone complexed with A) Viprinin, B) ViprininD1 and C) ViprininD2. Shaded regions are the error values. D) Overlaid RMSF plots with the ligand free Vpr backbone for comparative purposes.

In our study, ViprininD1 caused a marked structural alteration in Vpr, penetrating its hydrophobic core in most runs, unlike Viprinin and ViprininD2 (**Figure 28**). This penetration was favored by ViprininD1's more hydrophobic Piperidine ring.

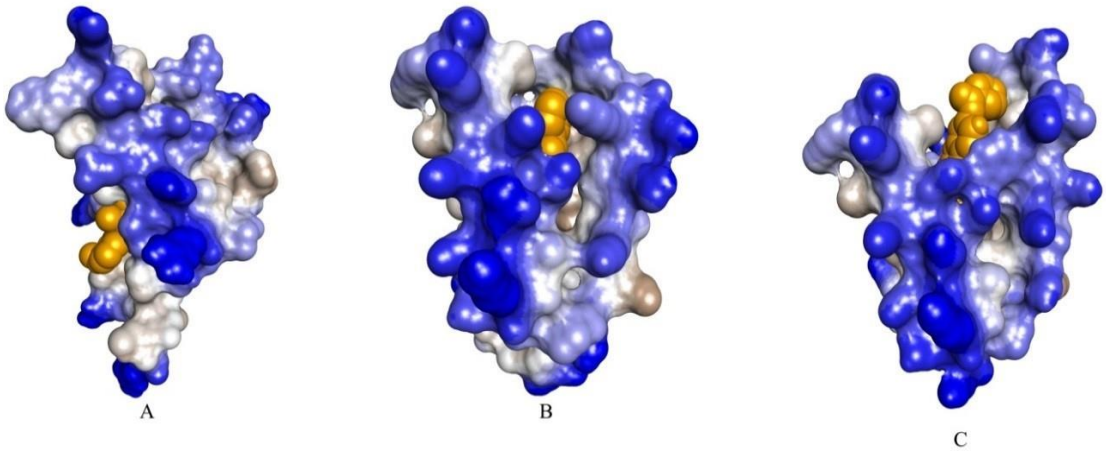

Figure 28: Vpr-ViprininD1 complex (run 1). A) Starting Docked pose of Vpr and ViprininD1. B) Average structure of Vpr-ViprininD1 at time interval of 30 ns to 35.8 ns. C) Average structure of Vpr-ViprininD1 at time interval of 35.9 ns to 50 ns. Vpr is presented with surface representation with probe radius of 1.4 Å and colored according to hydrophobicity. Orange molecule is the ViprininD1.

Elevated ligand RMSD values showed that all three ligands moved within or penetrated the hydrophobic pocket from the primary docking site during simulation, causing distortion to Vpr's structure (**Figure 29**). Ligands predominantly bound to the protein through multiple hydrophobic contacts, with only occasional hydrogen bonds (**Figure 30**).

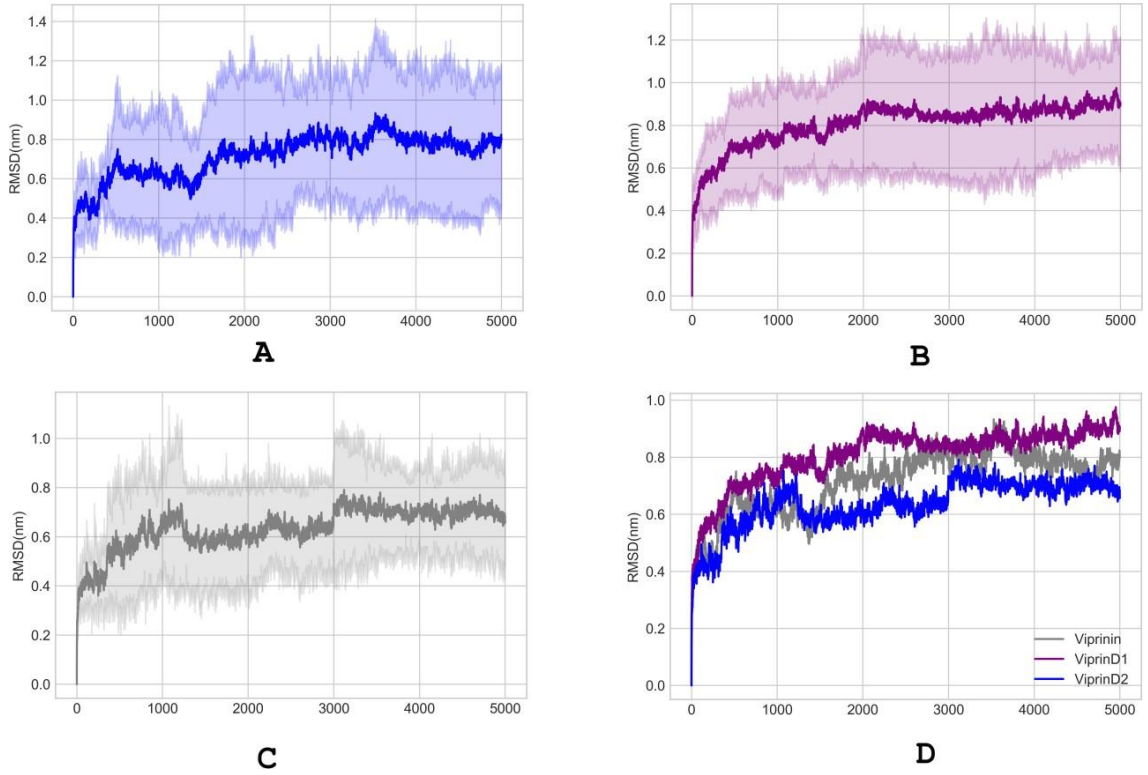

Figure 29: Average RMSD values of A) Viprinin, B) ViprininD1, C) ViprininD2 from seven runs after removing overall rotation and translation of Vpr. Shaded region is error value. D) Overlayed plot for comparative analysis purposes.

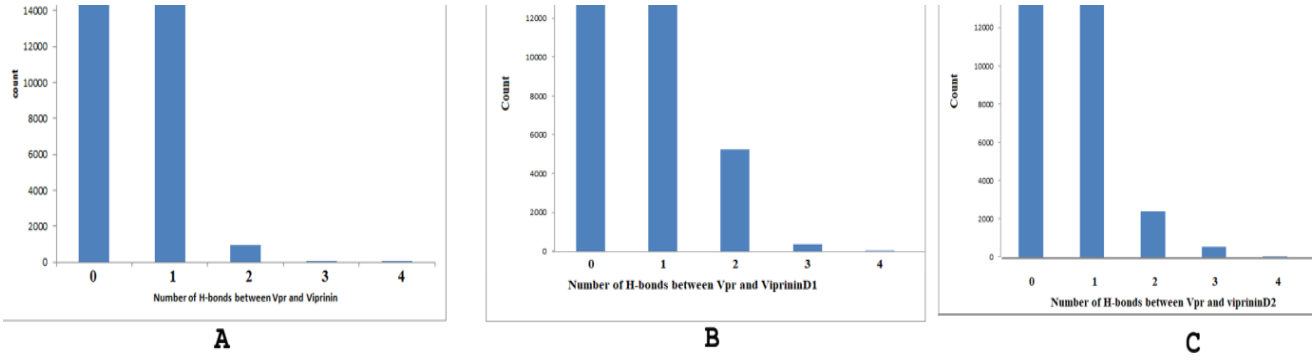

Figure 30: Histograms of the number of hydrogen bonds between Vpr and A) Viprinin, B) ViprininD1 and C) ViprininD2 over all time frames of all 7 runs.

4.1.3 Principal component analysis

From PCA, we observed differences in the modes and direction of motion vectors across various complexes. By projecting the structural ensemble onto the first three principal components, we quantitatively assessed the impact of ligands on the Vpr backbone (**Figure 31**). ViprininD1 and ViprininD2 significantly impacted the Vpr backbone dynamics, leading to distortion of the three-helix architecture. Vpr_V1's distortion increased the binding affinity for ViprininD1, while Vpr_V2's distortion reduced the binding affinity.

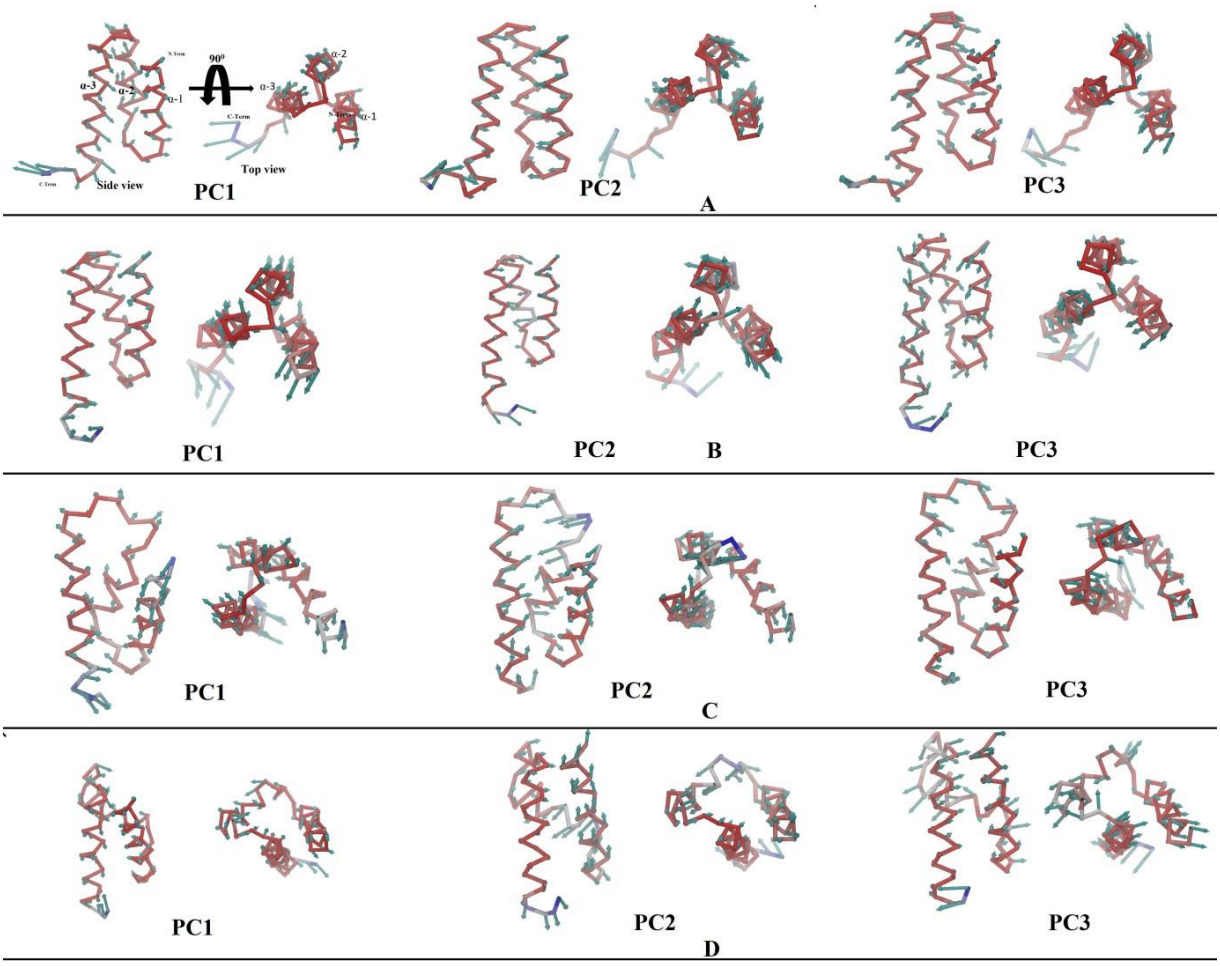

Figure 31: PCA is performed by concatenating the trajectories of seven independent runs (trajectories from 30 ns to 50 ns). Cα displacement vectors on PC1, PC2 and PC3 of A) Free Vpr; B) Vpr-Viprinin complex (Vpr_V); C) Vpr-ViprininD1 complex (Vpr_V1); D) Vpr-ViprininD2 complex (Vpr_V2) are shown. N-term, C-term and indexes of alpha helices are labelled on PC1 of Vpr. The orthographic top view is achieved by rotating the side view 900 anticlockwise along X-axis. The length of the arrow indicates the magnitude of the displacement. To quantitatively describe vector directionality between the proteins, cosine correlation or overlap values were calculated.

4.1.4 MM-PBSA calculation

We used MM-PBSA methods to assess the interaction strength of Viprinin, ViprininD1, and ViprininD2 with Vpr (**Figure 32**). This involved analyzing 1400 snapshots from the last 10 ns of each of the seven simulation runs. Viprinin exhibited a slightly higher, though statistically insignificant, binding energy (-97.2±12.09 kJ/mol) compared to ViprininD2 (-

96.4±14.4 kJ/mol). In contrast, ViprininD1 had the highest binding energy of -140±9.6 kJ/mol. Per-residue binding energy contributions revealed distinct preferences for the ligands. Viprinin and ViprininD2 primarily bound to α-Helix 3 (residues 59-77), while ViprininD1 entered the hydrophobic pocket, interacting with residues from all three α-Helices. This binding pattern could affect the formation of the DCAF1-Vpr-UNG2 complex, potentially impacting G2 cell cycle arrest activity. Specific residues contributing to binding were identified, with Leu26, Le68, Phe69, and Phe72 playing major roles in the binding of Viprinin and ViprininD2. ViprininD1 showed high energy contributions from Leu64 and Leu68. Surprisingly, Glu25 and Gln65, known for their importance in binding, had minimal contributions, with nearby Leu and Ile residues playing more significant roles in ligand binding (**Figure 33**).

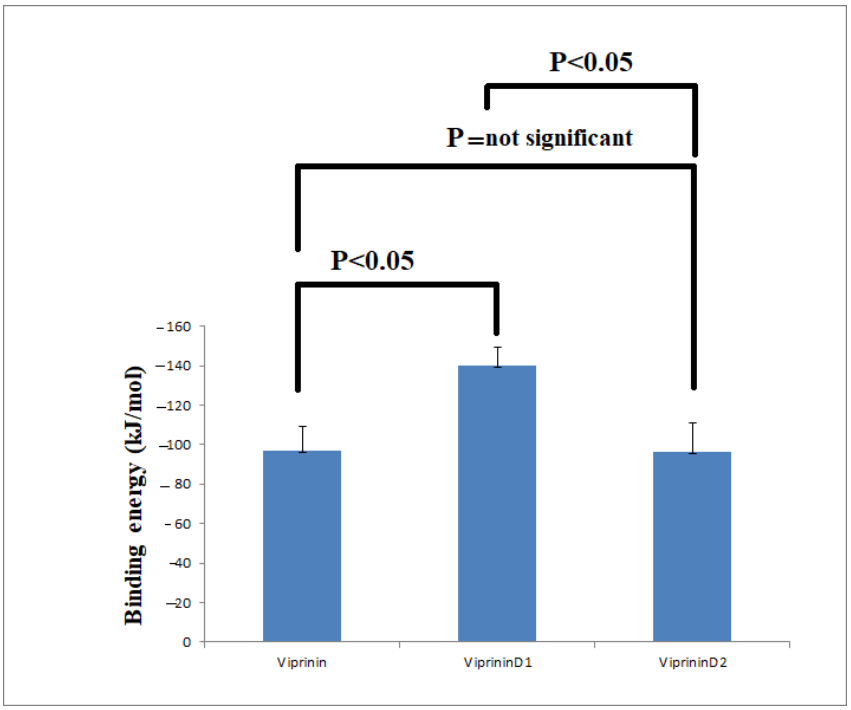

Figure 32: Average total binding energy of the ligands with Vpr drawn from seven independent runs.

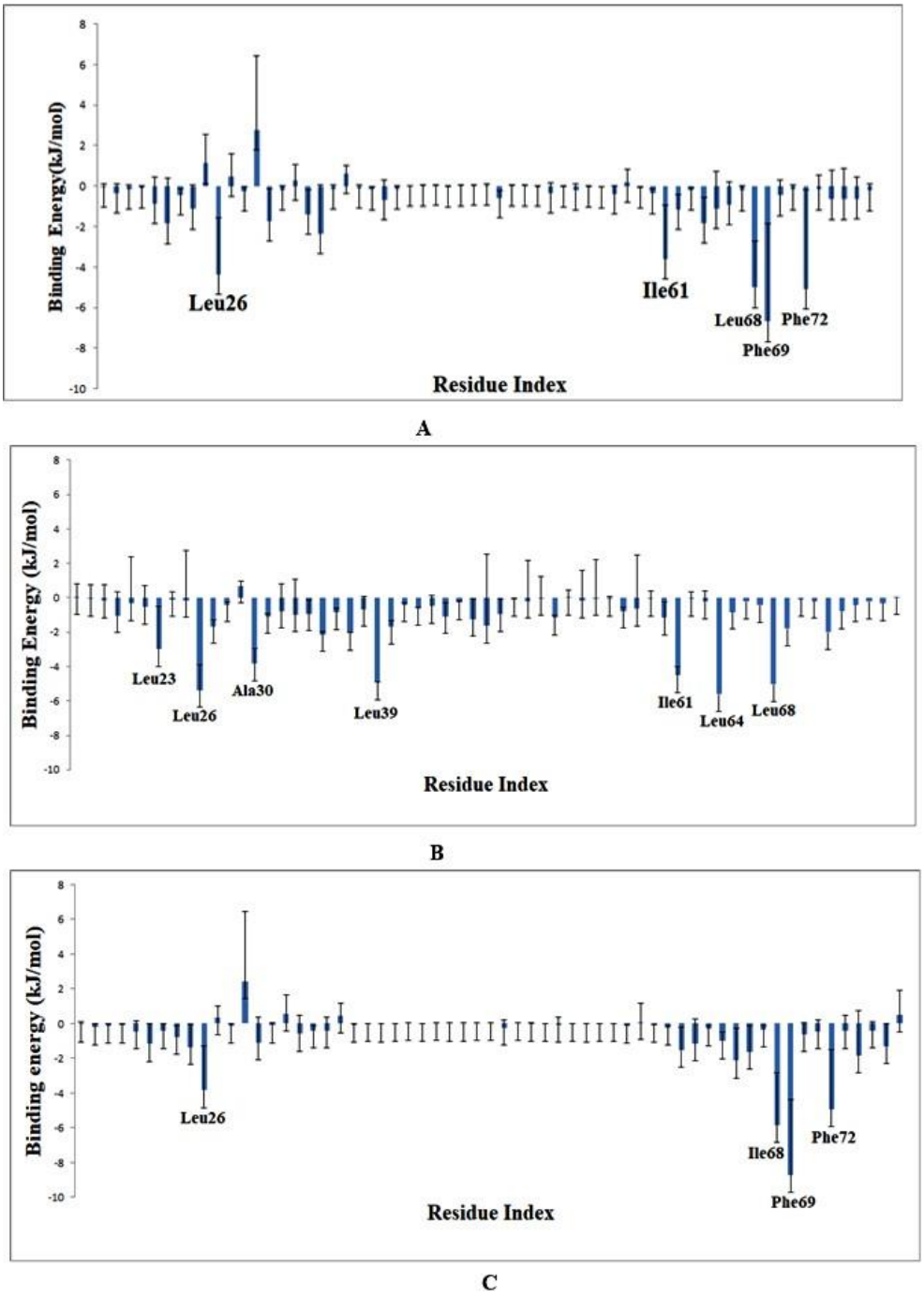

Figure 33: Average per residue binding energy of A) Vpr complexed with Viprinin, B) Vpr complexed with ViprininD1 and C) Vpr complexed with ViprininD2. Important residues are highlighted.

4.1.5 Umbrella sampling simulation

Three umbrella pulling simulations were conducted to investigate the binding mechanism of Viprinin, ViprininD1, and ViprininD2. These simulations aimed to calculate the potential of mean force (PMF) and determine the binding free energy (ΔG) by measuring the difference

between the highest and lowest PMF values. The computed average ΔG values were -10.5±3.7 kcal/mol-1 for Viprinin, -13.0±2.3 kcal/mol-1 for ViprininD1, and -7.8±1.07 kcal/mol-1 for ViprininD2, suggesting similar MM-PBSA binding energy patterns. In all three PMF profiles (**Figure 34**), the free energy starts at zero, decreases to a significant minimum, and stabilizes around ζ = 2.0-2.3 nm, representing the point at which noncovalent bonds between the ligand and the protein break.

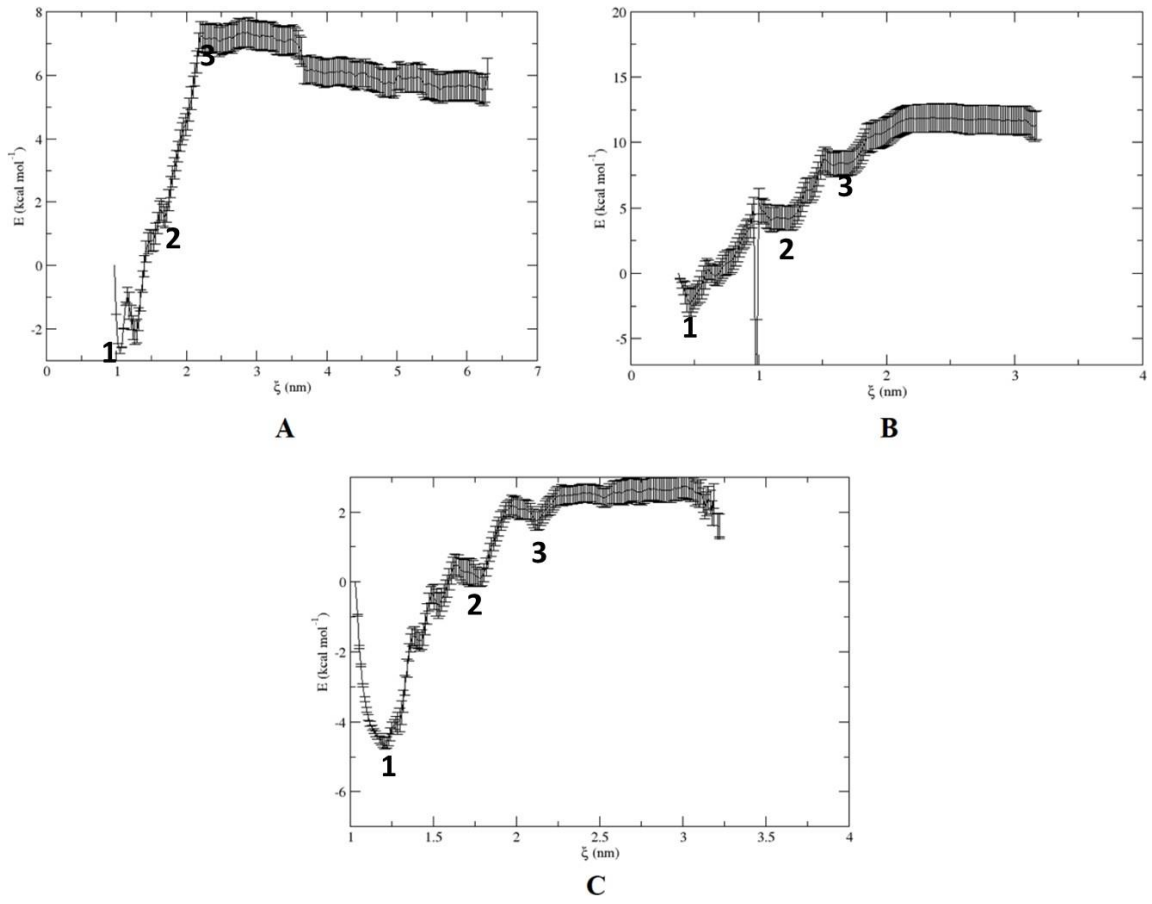

Figure 34: Representative potential of mean force (PMF) curve of the unbinding process of the ligands along reaction coordinate (z axis). Run which is very close to the average ΔG value is taken as representatives. A) PMF curve of Viprinin unbinding process; B) PMF curve of ViprininD1 unbinding process; C) PMF curve of ViprininD2 unbinding process. The error of computations was evaluated over 100 rounds of bootstrapping analysis. Snapshots are taken from the numbered points of the PMF profile

The unbinding process for all ligands involves the disruption of multiple hydrophobic interactions. Viprinin, for instance, forms interactions with Leu26, Leu68, Phe69, and Phe72, with the primary pocket involving pi-anion, alkyl, hydrogen bond, and pi-pi interactions.

These interactions gradually break during the unbinding process. ViprininD1 and ViprininD2 follow similar unbinding patterns with their respective interactions. Overall, the unbinding simulations shed light on the dynamics of ligand dissociation from the protein, with various noncovalent interactions playing essential roles in the process (**Figure 35**).

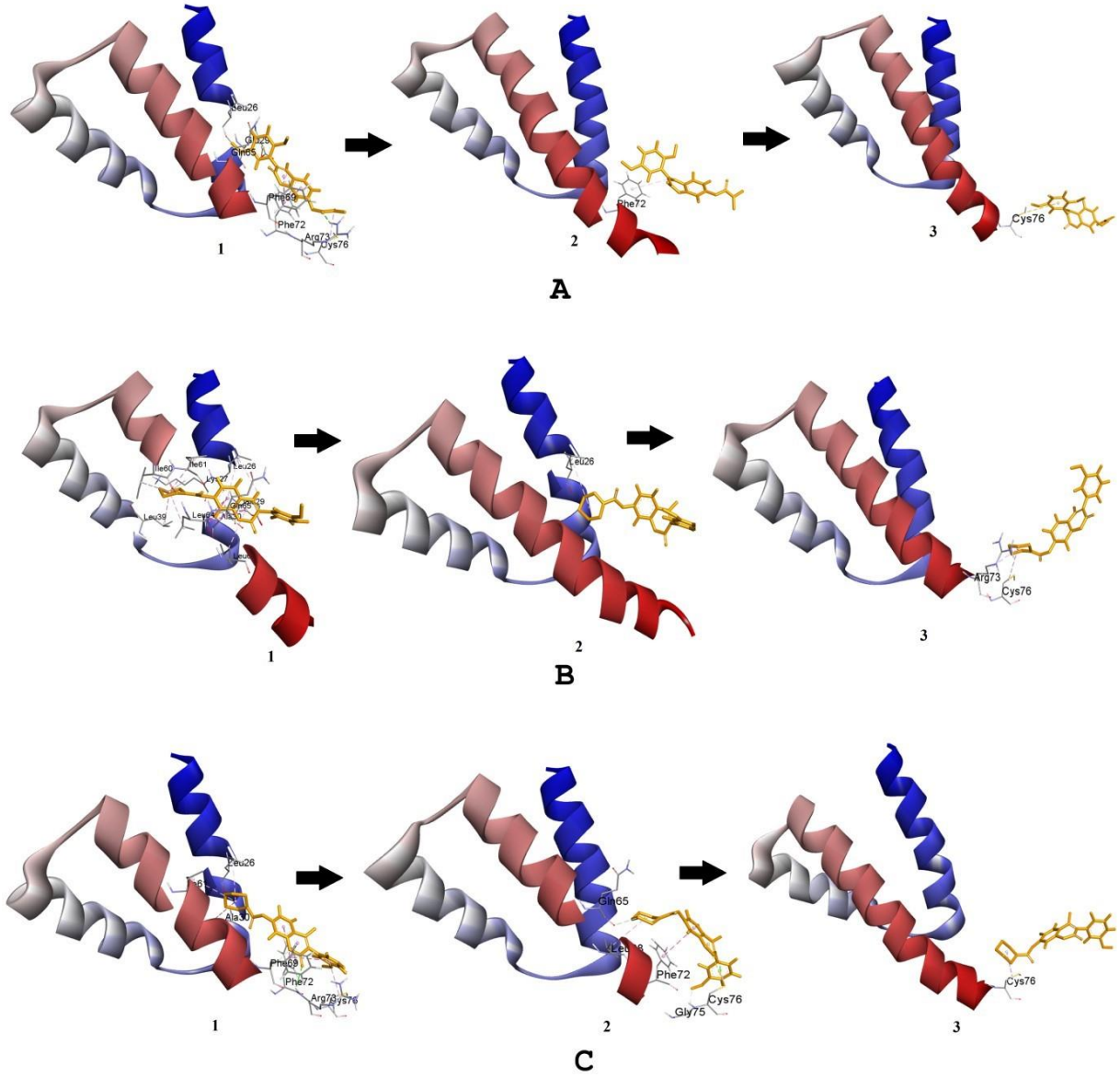

Figure 35: Unbinding process of the A) Viprinin; B) ViprininD1 and C) ViprininD2 from Vpr. Snapshots are taken from the various points of PMF curve.

4.2 Computer-aided De Novo Design and Optimization of novel potential inhibitors of HIV-1 Nef Protein

4.2.1 De-novo generation of a lead compound

We used Autogrow4 to develop a lead compound targeting pocket 3, which is most stable pocket as depicted in section 1.2. The algorithm was halted at generation 30 as docking scores reached a plateau after generation 24. The docking scores for each generation are shown in **Figure 36**, highlighting the top-ranked compounds.

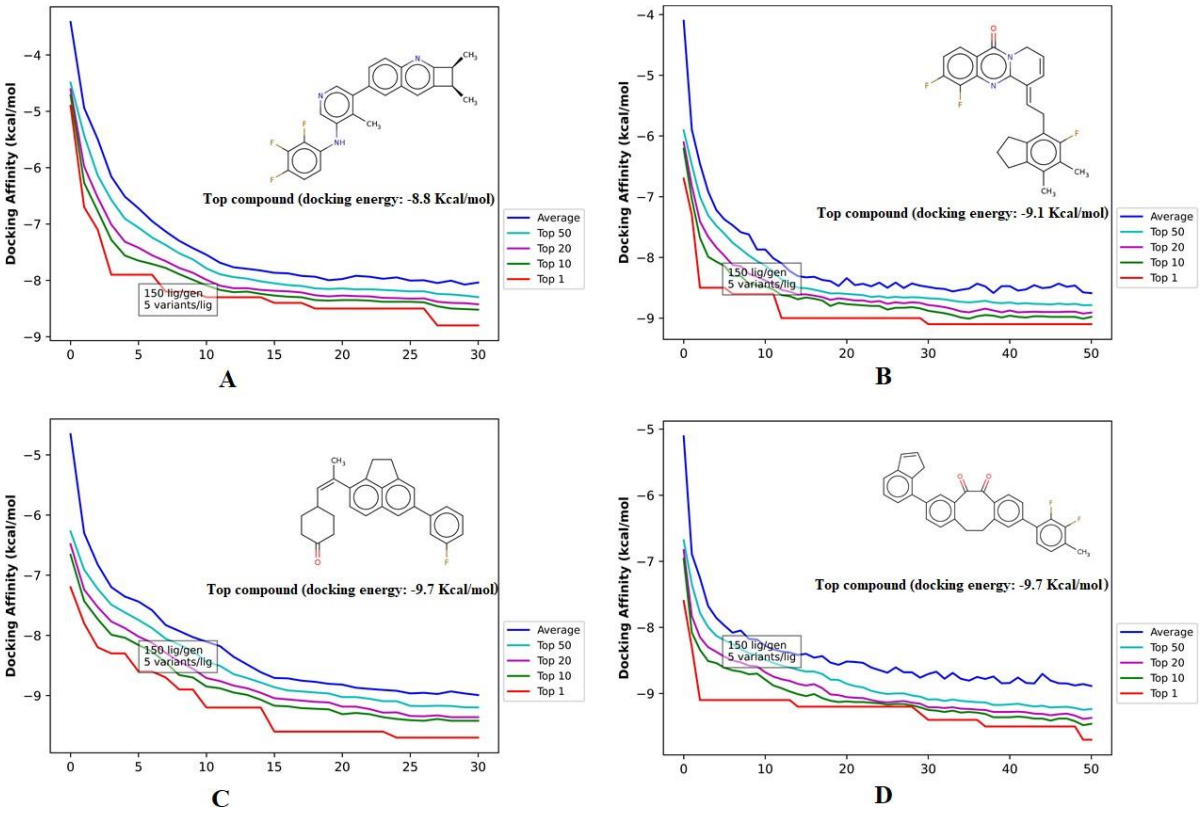

Figure 36: Autogrow4 generated compounds using ZINC fragment library of molecular weight (MW) A) ≤ 100; B) 100 ≤ MW ≤ 150; C)150 ≤ MW ≤ 200; D) 200 ≤ MW ≤ 250. The docking energy of the top compound from each category is reported.

Physicochemical properties of the compounds were assessed using SwissADME, revealing poor water solubility. The selected compounds, labeled compound 1 and compound 2, had the highest VINA scores (-9.7 kcal/mol) and were chosen for subsequent molecular dynamics (MD) simulations. The docked poses of top four compounds are detailed **in Figure 37 and Figure 38**.

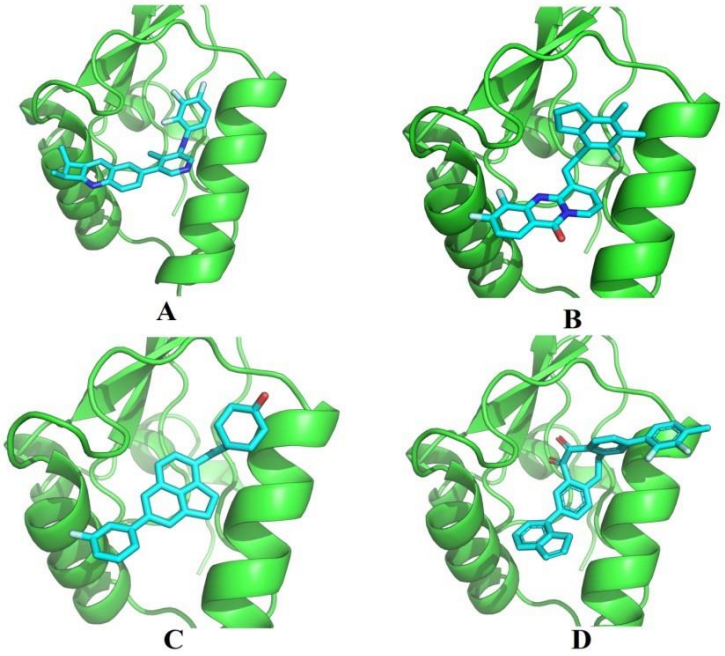

Figure 37: Initial binding pose of the AutoGrow4 generated compounds. A) ≤ 100; B) 100 ≤ MW ≤ 150; C)150 ≤ MW ≤ 200; D) 200 ≤ MW ≤ 250.

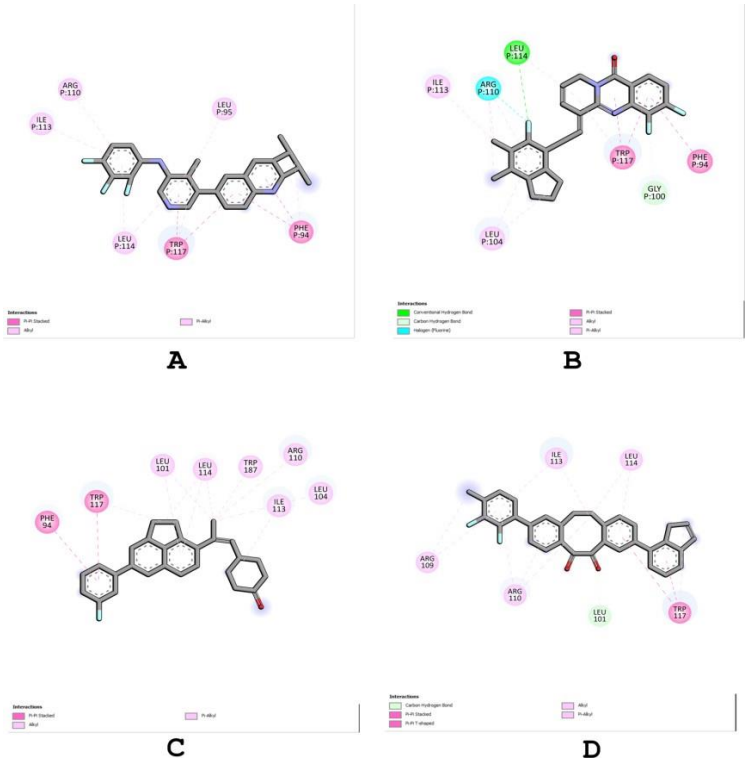

Figure 38: Two-dimensional interaction diagrams of the AutoGrow4 generated compounds with Nef. Diagrams are built in BIOVIA Discovery studio. A) ≤ 100; B) 100 ≤ MW ≤ 150; C)150 ≤ MW ≤ 200; D) 200 ≤ MW ≤ 250.

4.2.2 MD simulation of selected compounds

Five independent 100 nanosecond replicas were conducted for Nef-docked complexes of compound 1 and compound 2 and the trajectories are shown in **Figure 39**.

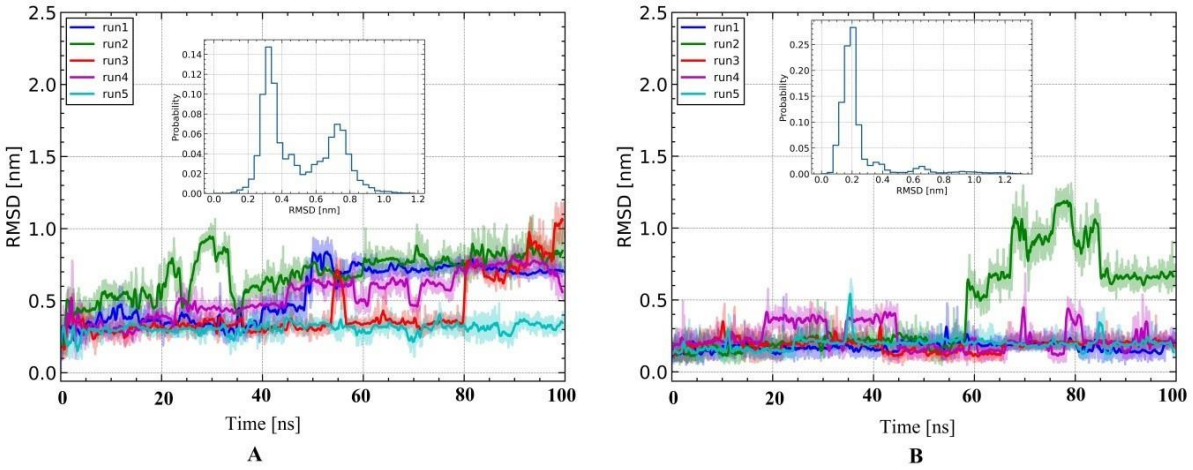

Figure 39: RMSD graph (with running average of 100 ps interval) and probability histogram (inset) of A) compound 1 and B) compound 2. Compound 2 exhibited greater stability, with RMSD values centered on 2.0 Å and the compound 1 displayed overall instability, with RMSD peaks at 3 Å and around 7 Å.

To investigate the stabilization of compound 2, PCA of the ligand conformations were performed. It was found that the Cyclohexanone oxygen was exposed to the solvent in every cluster (**Figure 40**)and stabilized by the water molecules. The fluorine (F) atom engaged in hydrogen bonding with water molecules in three out of four top clusters. Water molecules acting as bridges likely compensated for the lack of direct hydrogen bonds between compound 2 and Nef. Compound 2 appeared to mimic a similar hydrogen bond network (**Figure 41B**).

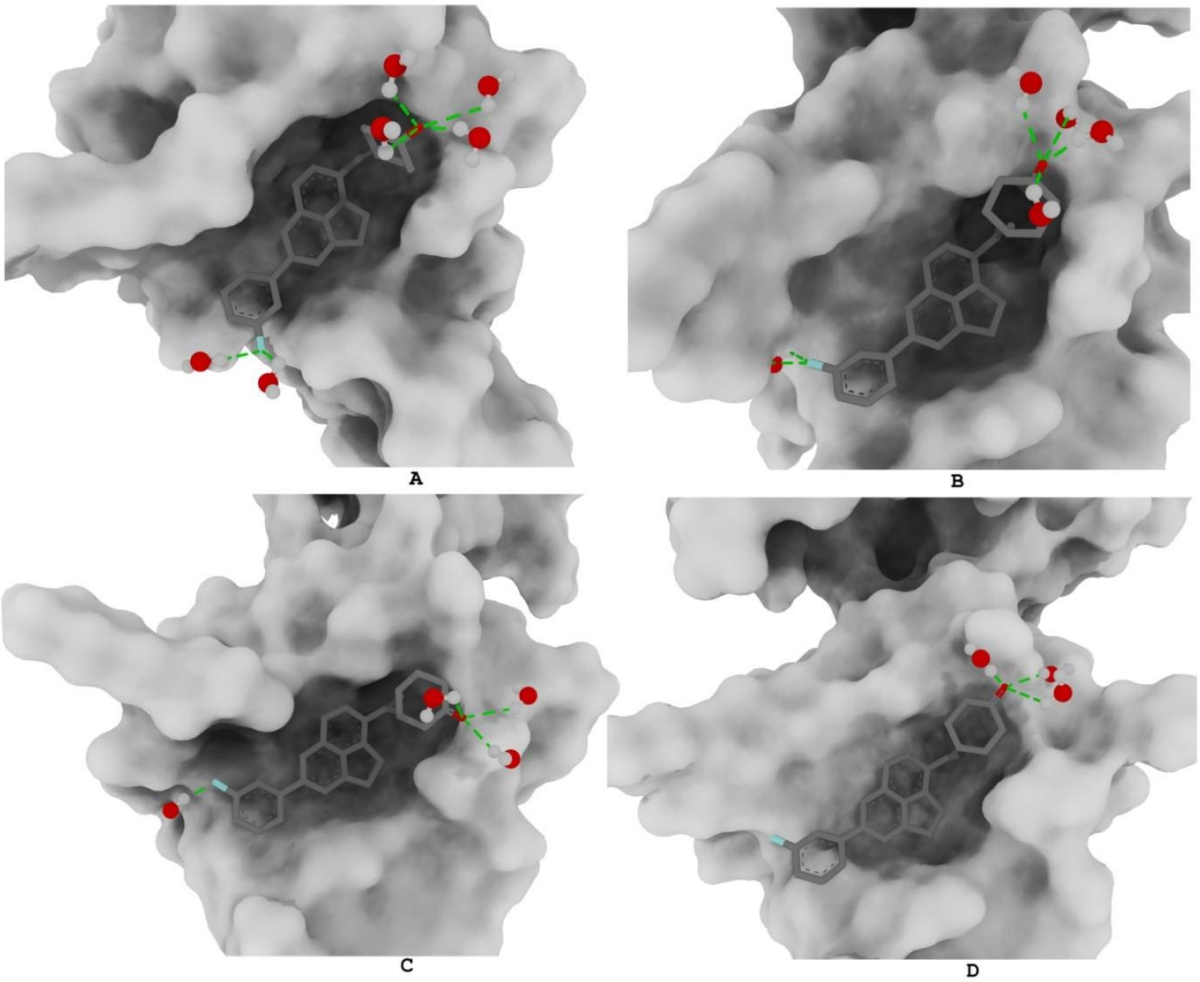

Figure 40: Representative structures from the top four densest clusters after K-means clustering of PCA data. A) Cluster 1 representative (probability=0.17); B) cluster 2 representative (probability=0.13); C) cluster 3 representative (probability=0.12) and D) cluster 4 representative (probability=0.11). The protein surface is colored as solvent accessibility with a probe radius of 1.4 Å.

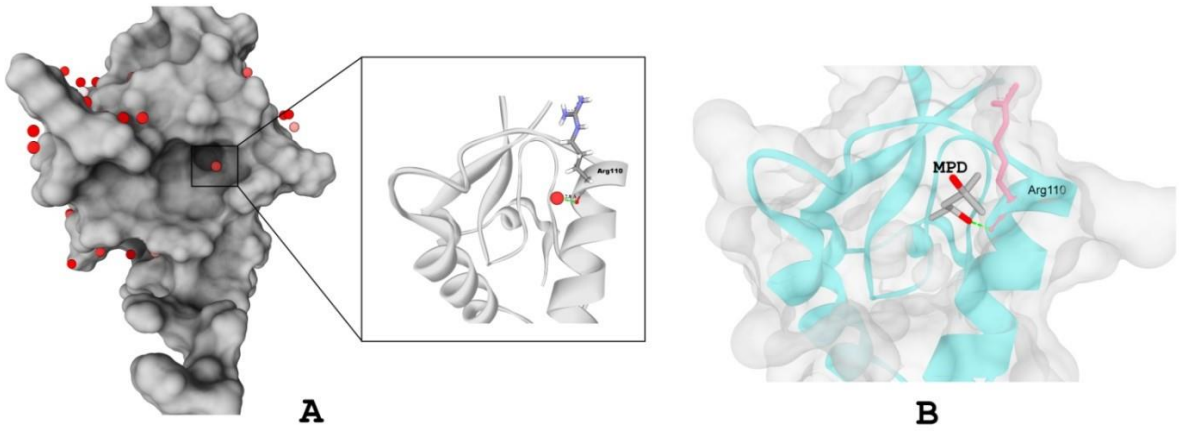

Figure 41: A) Hydration analysis of pocket 3. Stable water molecules are represented as red beads according to the occupancy value. B) MPD molecule bound with Arg110 through an H-bond in the crystal structure (PDB id: 4U5W).

4.2.3 Assessing the Accessibility of compound 2 towards pocket 3

From the ColDock runs, we found that two out of the five replicas closely resembled the VINA-docked pose (**Figure 42**) in pocket 3. This consistent binding was observed even at lower simulated ligand concentrations (**Figure 43**).

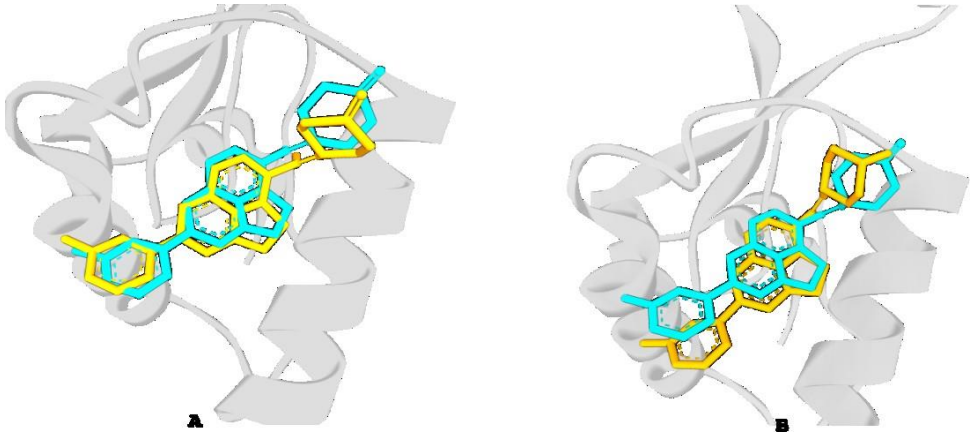

Figure 42: Alignment of VINA docked pose (Cyan) and ColDock generated pose (Orange). A) Central representative snapshot from the largest cluster of the six-ligands systems. RMSD between two poses is 1.37 Å. B) Central representative snapshots from the largest cluster of eight-ligands system. RMSD between two poses is 1.49 Å.

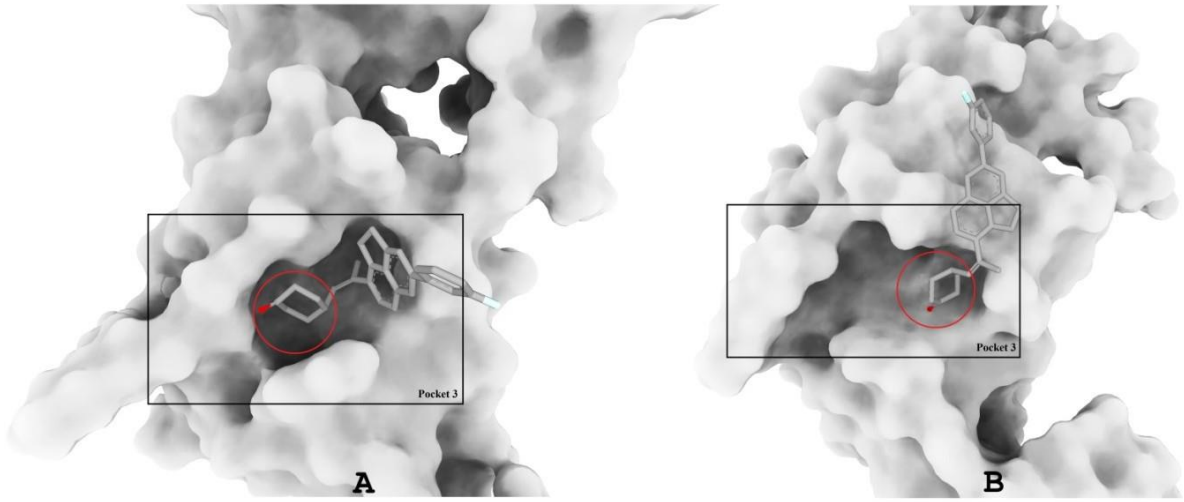

Figure 43: ColDock run from A) Six ligand and B) Eight ligand system. The cyclohexanone moiety (red circle) reaches towards pocket 3 but does not produce the native VINA pose.

4.2.4 Ligand modification to increase the solubility and druggability

Compound 2 (4-[(1Z)-2-[7-(3-fluorophenyl)-1,2-dihydroacenaphthylen-3-yl] prop-1-en-1-yl] cyclohexan-1-one) exhibits high lipophilicity and lacks H-bond donor atoms, leading to anticipated poor solubility in water (**Table 2**).

Table 2: Solubility of the modified compounds

Compounds	**Solubility Methods**								
		ESOL			**Ali**			**SILICOS-IT**	
	Log S	solubility	Class	Log S	solubility	Class	Log S	solubility	Class
Compound 2	-6.64	8.76e-05 mg/ml; 2.28e-07 mol/l	Poorly soluble	-6.84	5.54e-05 mg/ml; 1.44e-07 mol/l	Poorly soluble	-9.16	2.68e-07 mg/ml; 6.97e-10 mol/l	Poorly soluble
Compound2_mod1	-5.28	2.20e-03 mg/ml; 5.20e-06 mol/l	Moderately soluble	-5.82	6.47e-04 mg/ml; 1.53e-06 mol/l	Moderately soluble	-7.41	1.66e-05 mg/ml; 3.91e-08 mol/l	Poorly soluble
Compound2_mod2	-4.25	2.61e-02 mg/ml; 5.62e-05 mol/l	Moderately soluble	-4.28	2.42e-02 mg/ml; 5.23e-05 mol/l	Moderately soluble	-7.64	1.06e-05 mg/ml; 2.29e-08 mol/l	Poorly soluble

In an attempt to enhance its drug-like qualities and solubility, a new ligand, compound 2_mod-1 (3-{8-[(1E)-3-hydroxy-1-(4-oxocyclohexyl) prop-1-en-2-yl]acenaphthylen-4-yl}benzamide), was designed, introducing an -OH group and substituting a carboxamide (CONH2) group for the fluorine atom. In a further modification, Compound 2_mod-2 (3-{2,2-difluoro-5-[(1E)-3-hydroxy-1-(4-oxocyclohexyl) prop-1-en -2-yl]-6,9-diazatricyclo[6.3.1.04,12]dodeca-1(12),4,6,8,10-pentaen-10-ylbenzamide), two carbon atoms in the scaffold from modification 1 were replaced with nitrogen atoms, and two hydrogens were substituted with fluorine atoms (**Figure 44**).

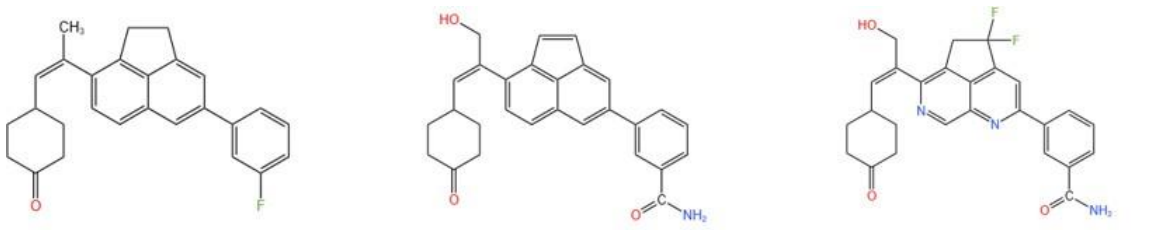

Compound 2 | Compound 2 modification 1 | Compound 2 modification 2

Figure 44: Modifications of the original lead compound (compound 2) to increase the solubility and drug-likeness.

These modifications led to improved computed solubility and drug-likeness (**Table 3**). Both compound 2_mod-1 and compound 2_mod-2 were subjected to docking in pocket 3 using VINA, showing favorable interactions with Nef (**Figure 45**).

Table 3: Solubility of the modified compounds

Compounds					**Solubility Methods**				
		ESOL			**Ali**			**SILICOS-IT**	
	Log S	solubility	Class	Log S	solubility	Class	Log S	solubility	Class
Compound 2	-6.64	8.76e-05 mg/ml; 2.28e-07 mol/l	Poorly soluble	-6.84	5.54e-05 mg/ml; 1.44e-07 mol/l	Poorly soluble	-9.16	2.68e-07 mg/ml; 6.97e-10 mol/l	Poorly soluble
Compound2_mod1	-5.28	2.20e-03 mg/ml; 5.20e-06 mol/l	Moderately soluble	-5.82	6.47e-04 mg/ml; 1.53e-06 mol/l	Moderately soluble	-7.41	1.66e-05 mg/ml; 3.91e-08 mol/l	Poorly soluble
Compound2_mod2	-4.25	2.61e-02 mg/ml; 5.62e-05 mol/l	Moderately soluble	-4.28	2.42e-02 mg/ml; 5.23e-05 mol/l	Moderately soluble	-7.64	1.06e-05 mg/ml; 2.29e-08 mol/l	Poorly soluble

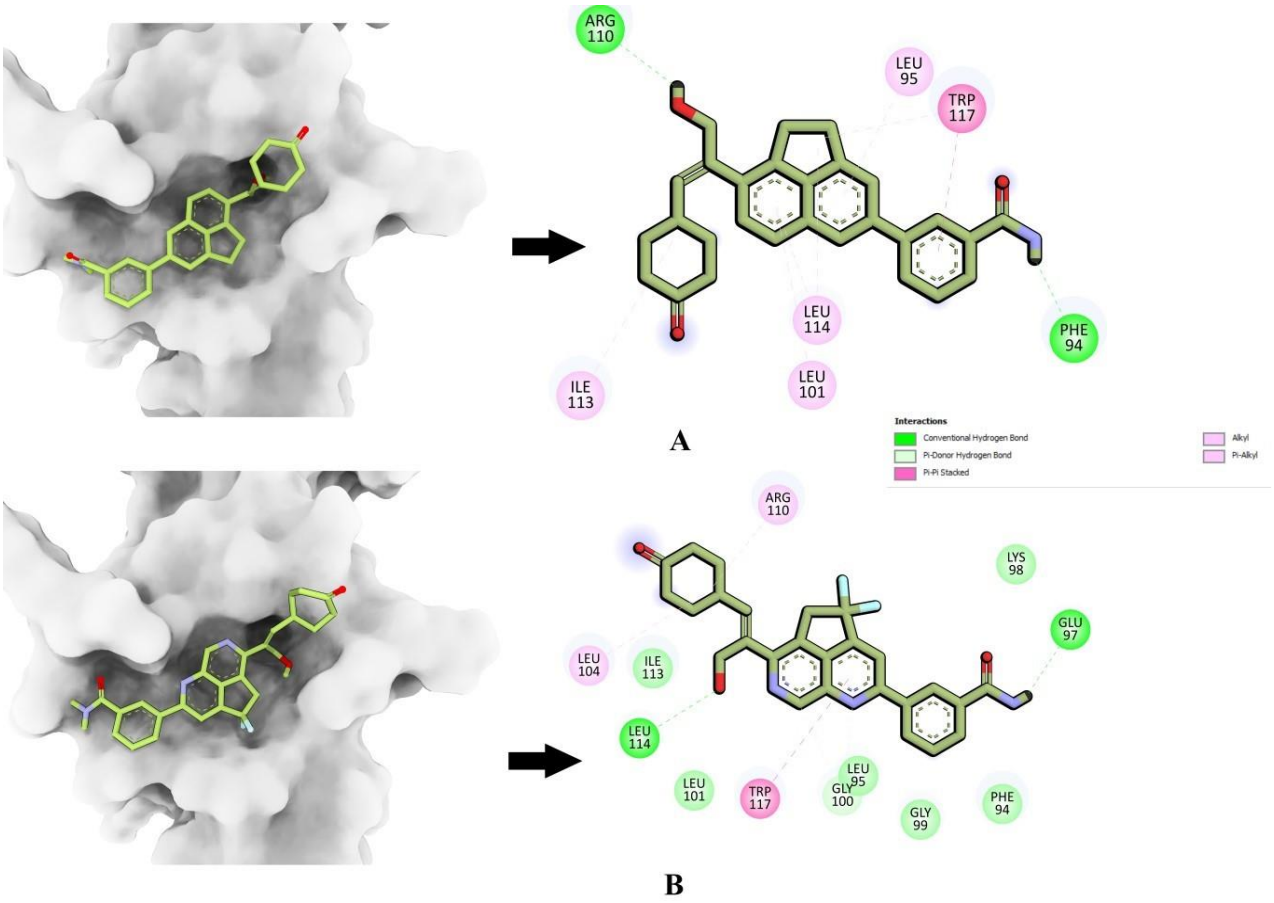

Figure 45: Docked poses of the modified compounds with Nef. A) Compound2_mod-1 and B) compound2_mod-2. Dashed colored lines are the various interaction types. 2D interaction diagrams are generated in BIOVIA discovery studio.

4.2.4 MD simulation of Nef-Modified compounds

Compound 2_mod-1 showed higher RMSD values during simulations compared to the original compound 2 (**Figure 46A**) but compound 2_mod-2 demonstrated greater stability (low RMSD) (**Figure 46B**). Representative structures from PCA based clustering analysis were examined for their binding poses and interaction patterns (**Figure 47**).

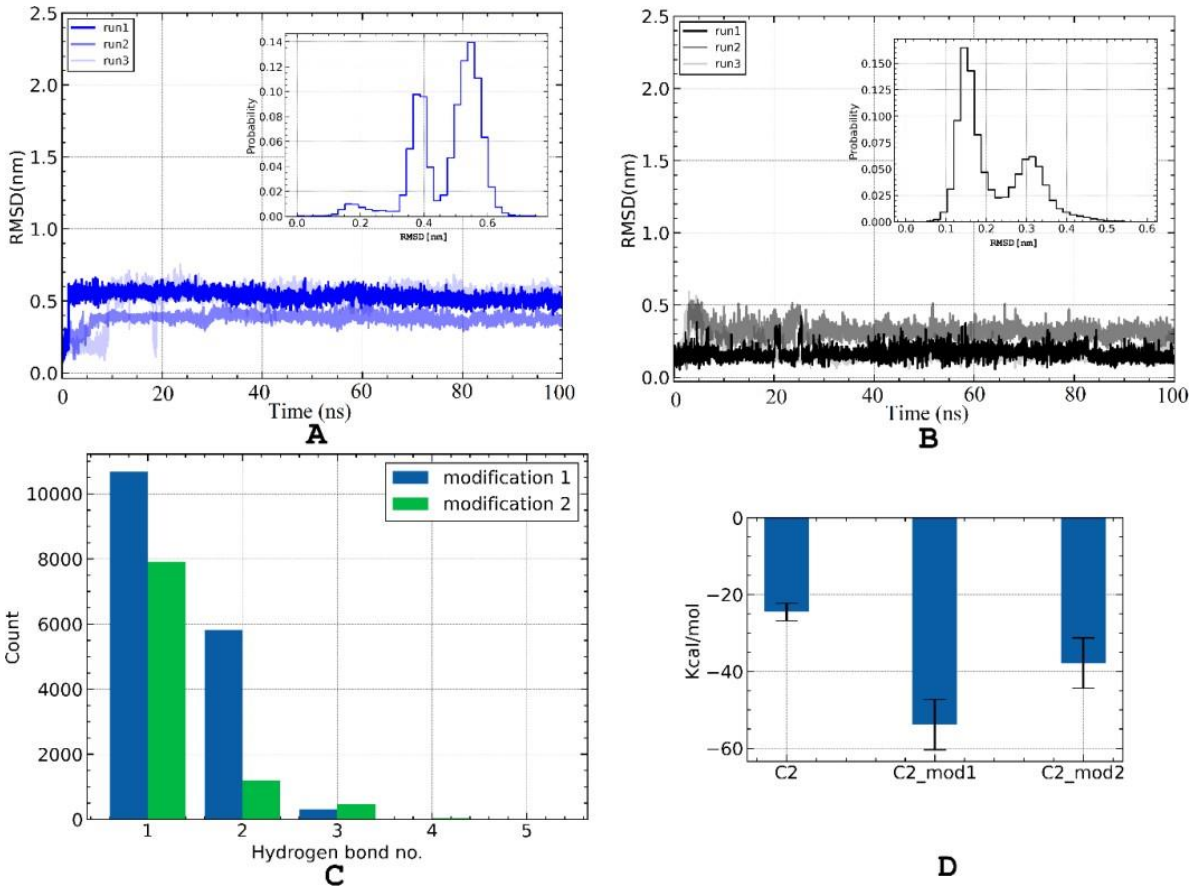

Figure 46: Post-docking MD simulation analysis of the Nef and modified ligand systems. A) RMSD graph and probability histogram (inset) of compound2_mod-1; B) RMSD graph and probability histogram (inset) of compound2_mod-2; C) Hydrogen bond number counts calculated from concatenated trajectories. D) MMGBSA binding free energy calculation at 300 K (C2=compound 2, C2_mod1= compound2_mod-1, C2_mod2= compound2_mod-2). Compound 2_mod-1 exhibited a relatively stronger binding free energy ((-52.22 ± 6.5 kcal/mol) compared to compound 2_mod-2 ((-35.6 ± 2.91 kcal/mol).

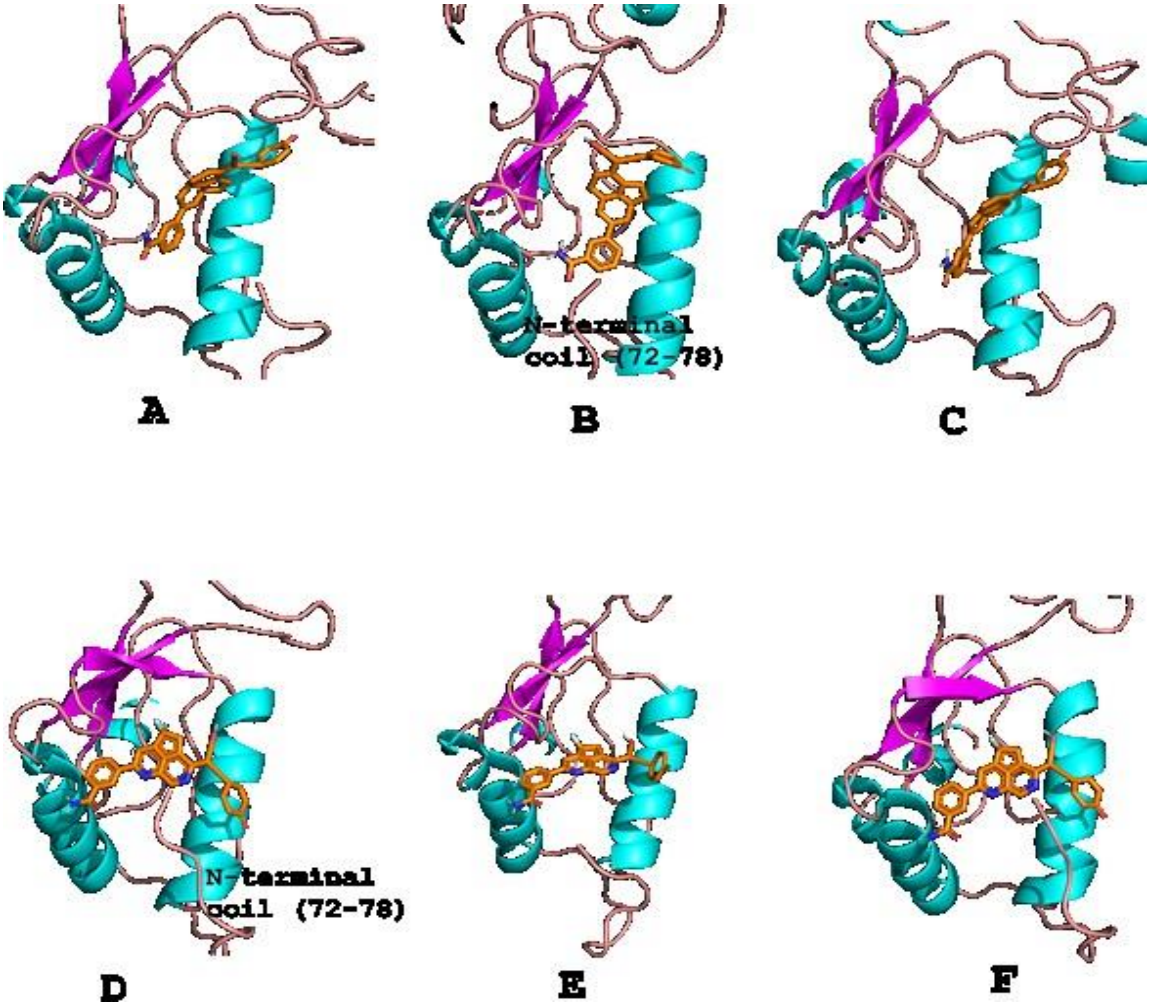

Figure 47: Representative structures from the top four densest clusters after K-means clustering of PCA data. A) Cluster 1, B) cluster 2 and C) cluster 3 representative of compound 2_mod-1. Compound 2_mod-1 formed a hydrogen bond with His170 (cluster 1) and engaged with the N-terminal random coil region (cluster 2) in addition to forming hydrogen bonds with Gly100 and Glu162. D) Cluster 1, E) cluster 2 and F) cluster 3 representative of compound 2_mod-2. Compound 2_mod-2 primarily interacted with the N-terminal random coil region, maintaining stability within the pocket groove. It also underwent a 180° flip relative to the initial VINA docked pose.

The RMSF data indicated reduced fluctuations of residues within pocket 3 in the presence of the compounds, while Rg and SASA patterns remained similar to apo-Nef (**Figure 48 and Figure 49A, B**).

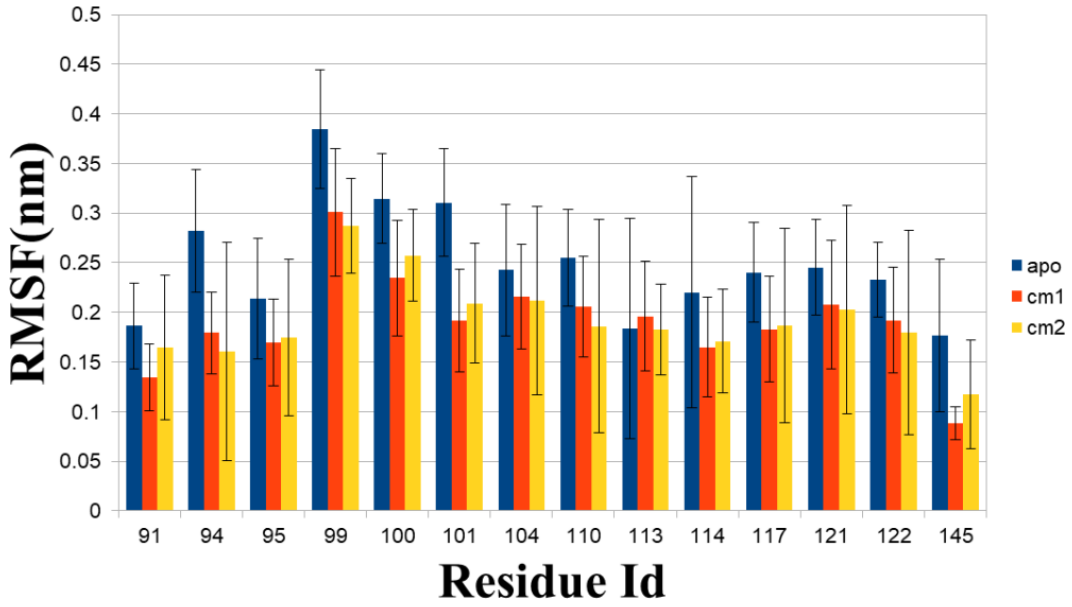

Figure 47: Root mean square fluctuation (RMSF) of the residues in pocket3 responsible for the ligand binding (cm1: Nef bound with compound2_modification1, cm2: Nef bound with compound2_modification2).

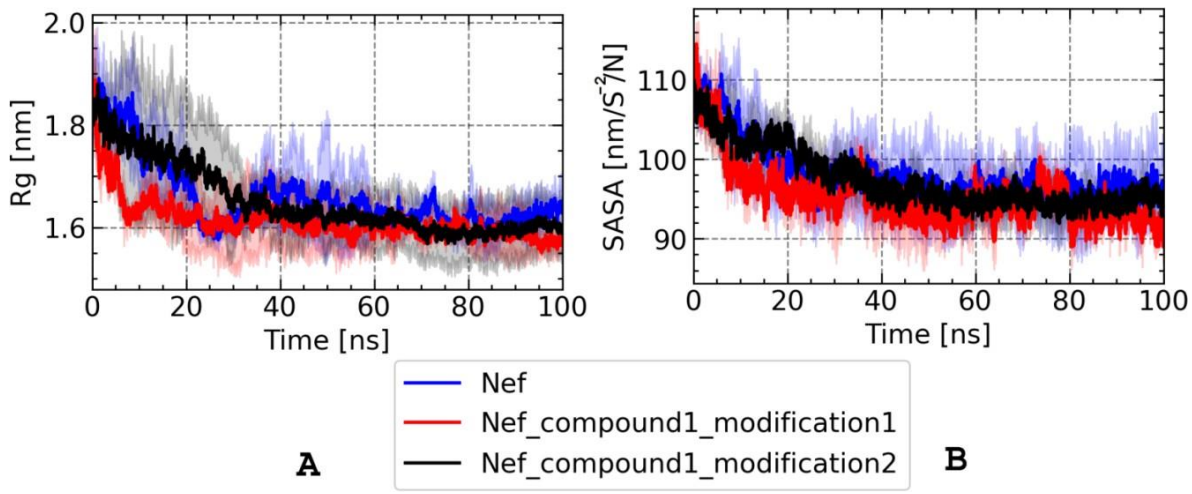

Figure 48: A) Radius of gyration and B) solvent accessible surface area (SASA) of the Nef protein backbone.

4.2.5 Binding Simulations of Compound 2_mod-2

In previous ColDock simulations at high concentrations of ligands, compound 2_mod-2 showed a spontaneous affinity for pocket 3 (**Figure 42**). To further investigate its binding

mechanism with Nef, we employed multiple walkers supervised molecular dynamics (mwSuMD) simulations (**Figure 49**).

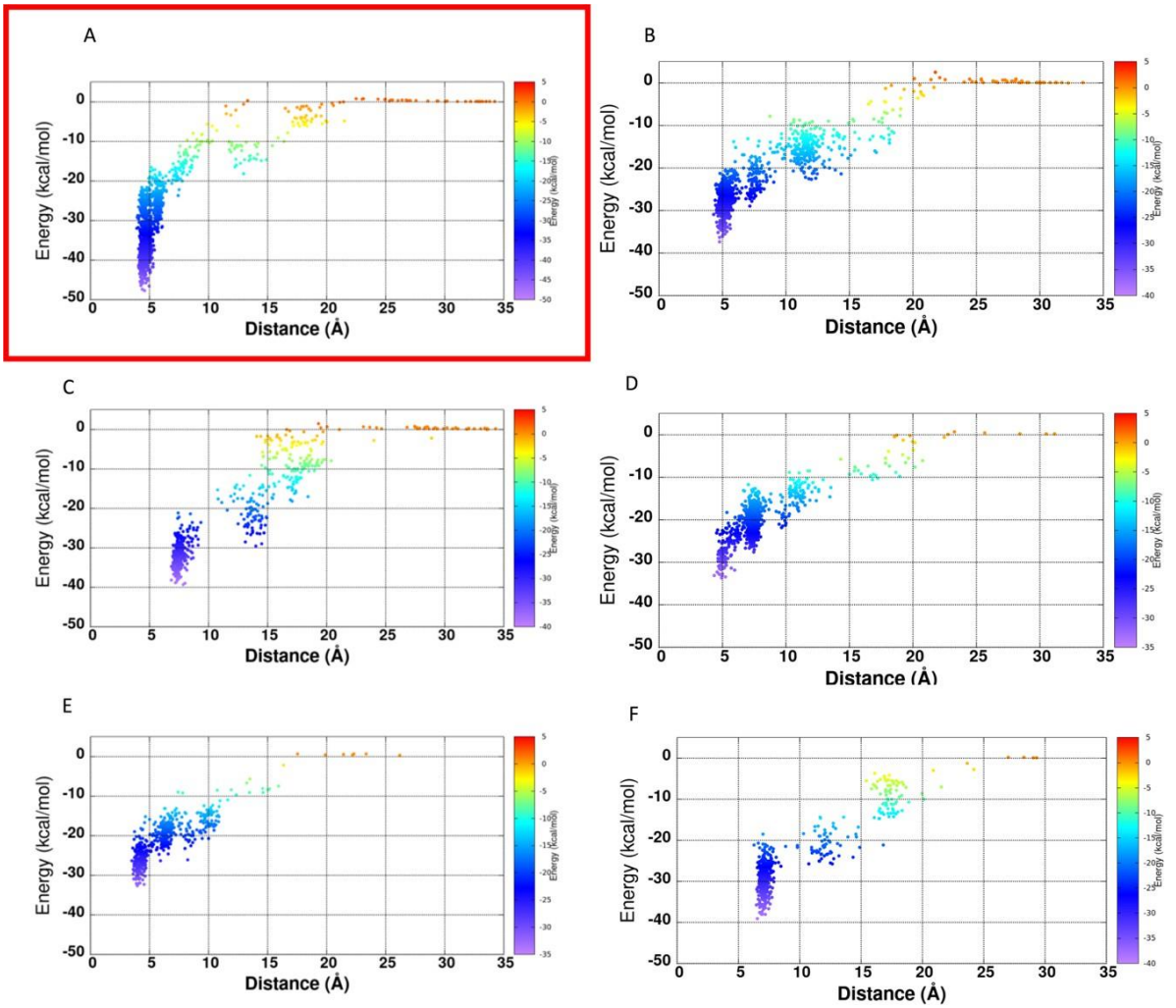

Figure 49: Binding energy landscapes of the six mwSuMD replicas. The best replica in terms of stabilization gained (A) was extended for 200 ns classic MD simulation.

During the binding process to Nef, the ligand initially formed metastable interactions with boundary residues of pocket 3, about 5-7 Å away from the binding site (**Figure 50A**). It then positioned itself within pocket 3, with the cyclohexanone ring near the side chain of Arg100 and the benzamide ring near Phe94. Key side chains involved in the binding are given in **Figure 50C**.

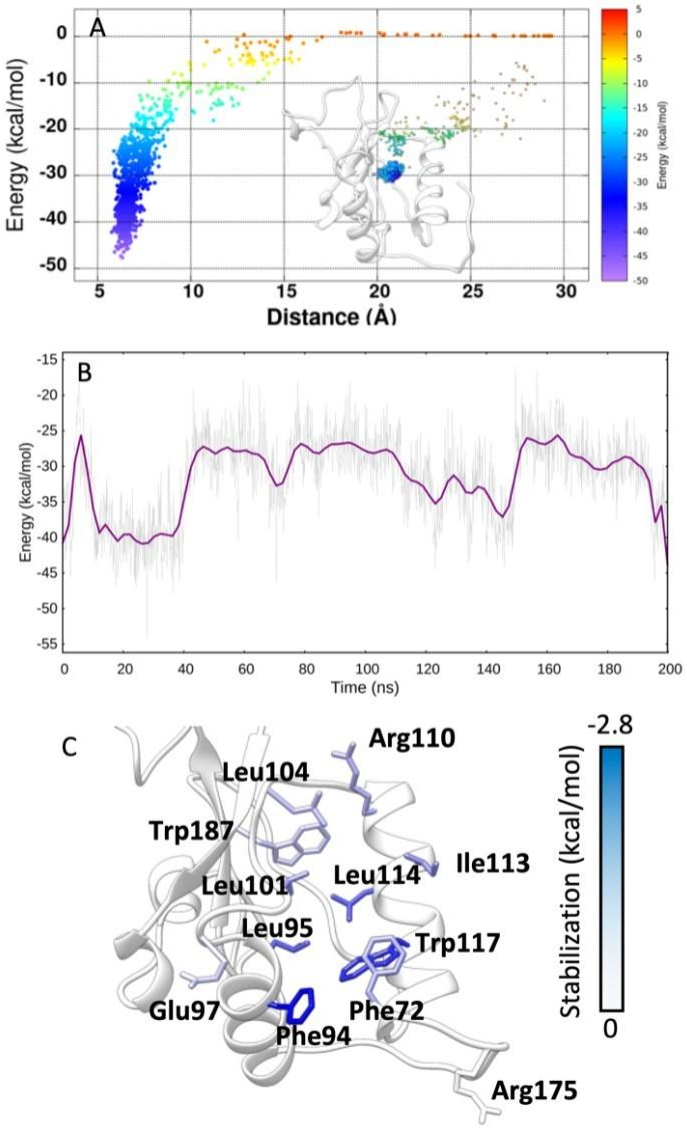

Figure 50: MwSuMD binding simulations pf Compound 2_mod-2. A) Binding energy landscape; **B**) MMGBSA analysis of the post-mwSuMD classic MD simulation. . The overall stabilization energy ranged from -20 to -45 kcal/mol with an average value of -31.4 ± 5.8 kcal/mol; **C**) Nef per-residue interaction energy during the post-mwSuMD classic MD simulation.

Conclusion

Objective 1: Study on the conformational dynamics of the HIV-1 accessory proteins

This computational investigation provides vital insights into the conformational dynamics of the HIV-1 accessory proteins Vpr and Nef. Extensive molecular dynamics simulations reveal that the C_helix of Vpr stably positions itself within lipid bilayers, likely forming the core transmembrane region that enables its ion channel function. In contrast, N_helix exhibits amphipathic properties and remains anchored to the membrane-solvent interface. Interestingly, full length Vpr undergoes substantial conformational change in membrane bilayer in order to be adapted in a channel compatible form. In this arrangement, the C_helix maintains a stable position within the bilayer core, running parallel to the bilayer normal, while the N_helix separates from the core and extends towards the membrane-solvent interface, leading to a previously unachieved, novel open configuration of the Vpr protein.

For Nef, three potential druggable pockets were identified and through extensive conformational sampling we found a pocket which demonstrates remarkable stability and rigidity. This pocket plays a key role in Nef dimerization through multiple hydrophobic and hydrogen bonding interactions with other monomer. We designed a novel inhibitor which is very specific to this pocket and has drug like properties. This compound can potentially disrupt the homodimeriztion process leading to the functional degradation of Nef. This study represents the first rational attempt to design inhibitors against Nef homodimerization in order to inhibit its pathogenic function inside host.

Objective 2: Studies on membrane association mechanisms of HIV-1 accessory proteins and elucidating the process of membrane channel formation

In this study using multistage computational methods, we elucidated the membrane orientation and dynamics of Vpr's helices to gain insights into its ion channel structure. Our findings revealed that embedded, tilted C_helix forms the active transmembrane segment, and it is very conformationally stable in bilayer. We computed the most stable, channel compatible conformation of the C_helix and modelled different oligomeric forms of the ion channel for the first time.

Objective 3: Investigation of selectivity mechanism and conductivity of ion channels formed by HIV-1 accessory proteins

We have predicted the architecture and ion selectivity filter of the HIV-1 Vpr ion channel through extensive molecular dynamics simulations and comparative modelling. Our results point to a pentameric channel arrangement showing stability, cation selective architecture, and electrostatic surface properties very similar to known Influenza M2 proton channel. These computational predictions provide structural insights of ion channel formed by Vpr for the first time which can guide future experiments to confirm the functional ion-conducting form and enable design of novel ion channel blockers.

Objective 4: Identification of suitable small molecules that may act as potential HIV-1 accessory protein inhibitors

This study utilized computational modelling approaches to identify and design potential HIV-1 Vpr and Nef inhibitors. Molecular docking and MD simulations revealed that ViprininD1, a derivative of the natural product Viprinin, exhibits potent inhibitory binding to the viral protein Vpr. ViprininD1 induced substantial conformational changes in Vpr by disrupting the protein's native structure. Binding free energy calculations confirmed ViprininD1 has the strongest affinity among the Viprinin derivatives tested. These findings indicate ViprininD1's potential as a novel Vpr inhibitor warranting further experimental validation.

A *de novo* design strategy generated lead compounds targeting the HIV-1 Nef protein. Lead optimization and MD simulations identified a compound named 3-{2,2-difluoro-5-[(1E)-3-hydroxy-1-(4-oxocyclohexyl) prop-1-en -2-yl]-6,9-diazatricyclo[6.3.1.04,12]dodeca-1(12),4,6,8,10-pentaen-10-ylbenzamide as a promising Nef inhibitor. This compound showed improved solubility and drug-likeness compared to the original lead. Binding simulations revealed spontaneous, specific binding to the target Nef pocket mediated by key functional residues. This compound may act as a starting point for developing Nef inhibitors with nanomolar affinity. This computational study discovered two promising HIV-1 accessory protein against Vpr and Nef. If effective, these compounds or their derivatives could potentially be developed into novel antiretroviral therapies targeting HIV-1 accessory proteins.

Significance of the study

This study makes significant contributions towards elucidating the structural and functional dynamics of key HIV-1 accessory proteins using advanced computational techniques. By employing extensive all-atom and coarse-grained molecular dynamics simulations combined with enhanced sampling methods, it provides crucial atomic-scale insights into the conformational mechanisms of the Vpr and Nef proteins. A major highlight is the extensive modelling conducted to characterize Vpr's membrane association and ion channel formation processes. The simulations reveal how specific helical segments orient themselves in the lipid bilayer, with the C-helix stably embedding within the membrane core. The proposed Vpr ion channel models mark the first concerted effort at structurally characterizing this important functional complex and its selectivity mechanisms. The models enable a deeper understanding of Vpr's role in regulating ion conductance and disrupting the cell membrane potential.

The identification and assessment of structural pockets on Nef highlights promising druggable sites for targeting its interactions and downstream signalling effects. The stability analysis points to the homodimerization pocket as a suitable candidate for structure-based inhibitor design against Nef. Furthermore, the project computationally screens and optimizes novel small molecule compounds against Vpr and Nef through molecular docking studies and dynamic simulations. Lead compounds are modified to improve their solubility and binding capabilities. The effective binding of designed inhibitors validates the identified target sites for disruption of viral activity.

By providing molecular insights into HIV-1 protein conformations, structural dynamics, and inhibition strategies, this study makes significant contributions to anti-HIV drug discovery efforts. The extensive use of computational biophysics enhances interpretability compared to purely data-driven approaches. The proposed ion channel models of Vpr have broader biological impact beyond viral mechanisms. Overall, the research forms a vital framework for future studies on HIV-1 structural biology and structure-based drug development using computational simulations.

Future directions

This study provides a strong computational framework for studying the structural dynamics of HIV-1 accessory proteins like Vpr and Nef. The modelling and simulations can be expanded in several fruitful directions to deepen the mechanistic insights gained. One interesting avenue is performing long time scale simulations (hundreds of microseconds) with advanced sampling techniques (i.e. Metadynamics, conformational flooding etc.) to capture large conformational changes in accessory proteins, going beyond the nanosecond scale phenomena characterized currently. Events like helix folding/unfolding, complex dissociation pathways, and collective motions require modelling microsecond to millisecond scale processes. The work on ion channels can also be enhanced by simulating ion permeation and blockage mechanisms using advanced algorithms.

From a drug discovery standpoint, the designed compounds against Vpr and Nef can undergo quantitative structure-activity relationship (QSAR) studies to correlate inhibition potencies with physicochemical properties. Modeling interactions with other underexplored pockets on the proteins is also worthwhile. The lead candidates can be synthesized and assayed in vitro to measure antiviral activities against HIV-1.

References

1. Richter SN, Frasson I, Palù G. Strategies for inhibiting function of HIV-1 accessory proteins: a necessary route to AIDS therapy? Curr Med Chem. 2009;16(3):267-86. doi: 10.2174/092986709787002646. PMID: 19149577.

2. https://www.unaids.org/en/resources/fact-sheet

3. Kogan M, Rappaport J. HIV-1 accessory protein Vpr: relevance in the pathogenesis of HIV and potential for therapeutic intervention. Retrovirology. 2011 Apr 13;8:25. doi: 10.1186/1742-4690-8-25. PMID: 21489275; PMCID: PMC3090340.

4. Strebel K. HIV accessory proteins versus host restriction factors. Curr Opin Virol. 2013 Dec;3(6):692-9. doi: 10.1016/j.coviro.2013.08.004. Epub 2013 Nov 15. PMID: 24246762; PMCID: PMC3855913.

5. Stevenson M. HIV-1 pathogenesis. Nat Med. 2003 Jul;9(7):853-60. doi: 10.1038/nm0703-853. PMID: 12835705.

6. Cohen A., Terwilliger E.F., Sodroski J.G., Haseltine W.A. Identification of a protein encoded by the vpu gene of HIV-1. Nature. 1988;334:532–534. doi: 10.1038/334532a0.

7. Carrasco L. Modification of membrane permeability by animal viruses. Adv. Virus Res. 1995;45:61–112.

8. Gonzalez M.E., Carrasco L. Viroporins. FEBS Lett. 2003;552:28–34. doi: 10.1016/S0014-5793(03)00780-4.

9. Nieva J.L., Madan V., Carrasco L. Viroporins: Structure and biological functions. Nat. Rev. Microbiol. 2012;10:563–574. doi: 10.1038/nrmicro2820.

10. Willey R.L., Maldarelli F., Martin M.A., Strebel K. Human immunodeficiency virus type 1 Vpu protein induces rapid degradation of CD4. J. Virol. 1992;66:7193–7200.

11. Willey R.L., Maldarelli F., Martin M.A., Strebel K. Human immunodeficiency virus type 1 Vpu protein regulates the formation of intracellular gp160-CD4 complexes. J. Virol. 1992;66:226–234.

12. Geraghty R.J., Panganiban A.T. Human immunodeficiency virus type 1 Vpu has a CD4- and an envelope glycoprotein-independent function. J. Virol. 1993;67:4190–4194.

13. Wray V., Federau T., Henklein P., Klabunde S., Kunert O., Schomburg D., Schubert U. Solution structure of the hydrophilic region of HIV-1 encoded virus protein U (Vpu) by CD and 1H NMR spectroscopy. Int. J. Pept. Protein Res. 1995;45:35–43. doi: 10.1111/j.1399-3011.1995.tb01565.x.

14. Chen M.Y., Maldarelli F., Karczewski M.K., Willey R.L., Strebel K. Human immunodeficiency virus type 1 Vpu protein induces degradation of CD4 in vitro: The cytoplasmic domain of CD4 contributes to Vpu sensitivity. J. Virol. 1993;67:3877–3884.
15. Schubert U., Strebel K. Differential activities of the human immunodeficiency virus type 1-encoded Vpu protein are regulated by phosphorylation and occur in different cellular compartments. J. Virol. 1994;68:2260–2271.
16. Veillette M., Desormeaux A., Medjahed H., Gharsallah N.E., Coutu M., Baalwa J., Guan Y., Lewis G., Ferrari G., Hahn B.H., et al. Interaction with cellular CD4 exposes HIV-1 envelope epitopes targeted by antibody-dependent cell-mediated cytotoxicity. J. Virol. 2014;88:2633–2644. doi: 10.1128/JVI.03230-13.
17. Pham T.N., Lukhele S., Hajjar F., Routy J.P., Cohen E.A. HIV Nef and Vpu protect HIV-infected CD4+ T cells from antibody-mediated cell lysis through down-modulation of CD4 and BST2. Retrovirology. 2014;11:e15. doi: 10.1186/1742-4690-11-15.
18. Van D.N., Goff D., Katsura C., Jorgenson R.L., Mitchell R., Johnson M.C., Stephens E.B., Guatelli J. The interferon-induced protein BST-2 restricts HIV-1 release and is downregulated from the cell surface by the viral Vpu protein. Cell Host Microbe. 2008;3:245–252.
19. Grice A.L., Kerr I.D., Sansom M.S. Ion channels formed by HIV-1 Vpu: A modelling and simulation study. FEBS Lett. 1997;405:299–304. doi: 10.1016/S0014-5793(97)00198-1.
20. Padhi S, Khan N, Jameel S, Priyakumar UD. Molecular dynamics simulations reveal the HIV-1 Vpu transmembrane protein to form stable pentamers. PLoS One. 2013 Nov 6;8(11):e79779. doi: 10.1371/journal.pone.0079779. PMID: 24223193; PMCID: PMC3819244.
21. Coady M.J., Daniel N.G., Tiganos E., Allain B., Friborg J., Lapointe J.Y., Cohen E.A. Effects of Vpu expression on Xenopus oocyte membrane conductance. Virology. 1998;244:39–49. doi: 10.1006/viro.1998.9087.
22. Hsu K., Han J., Shinlapawittayatorn K., Deschenes I., Marban E. Membrane potential depolarization as a triggering mechanism for Vpu-mediated HIV-1 release. Biophys. J. 2010;99:1718–1725. doi: 10.1016/j.bpj.2010.07.027.
23. Herrero L., Monroy N., Gonzalez M.E. HIV-1 Vpu protein mediates the transport of potassium in Saccharomyces cerevisiae. Biochemistry. 2013;52:171–177. doi: 10.1021/bi3011175.
24. González ME. Vpu Protein: The Viroporin Encoded by HIV-1. Viruses. 2015 Aug 4;7(8):4352-68. doi: 10.3390/v7082824. PMID: 26247957; PMCID: PMC4576185.

25. Zhang H, Pomerantz RJ, Dornadula G, Sun Y. Human immunodeficiency virus type 1 Vif protein is an integral component of an mRNP complex of viral RNA and could be involved in the viral RNA folding and packaging process. J Virol. 2000 Sep;74(18):8252-61. doi: 10.1128/jvi.74.18.8252-8261.2000. PMID: 10954522; PMCID: PMC116333.

26. Takaori-Kondo A, Shindo K. HIV-1 Vif: a guardian of the virus that opens up a new era in the research field of restriction factors. Front Microbiol. 2013 Feb 20;4:34. doi: 10.3389/fmicb.2013.00034. PMID: 23430691; PMCID: PMC3576844.

27. Usami, Y., Wu, Y., and Göttlinger, H. G. (2015) SERINC3 and SERINC5 restrict HIV-1 infectivity and are counteracted by Nef. Nature 526, 218–223

28. Saksela, K. (2011) Interactions of the HIV/SIV pathogenicity factor Nef with SH3 domain-containing host cell proteins. Curr. HIV. Res. 9,531–542

29. Geyer M, Munte CE, Schorr J, Kellner R, Kalbitzer HR. Structure of the anchor-domain of myristoylated and non-myristoylated HIV-1 Nef protein. J Mol Biol. 1999 May 28;289(1):123-38. doi: 10.1006/jmbi.1999.2740. PMID: 10339411.

30. Gerlach, H., Laumann, V., Martens, S., Becker, C. F., Goody, R. S., and Geyer, M. (2010) HIV-1 Nef membrane association depends on charge, curvature, composition and sequence. Nat. Chem. Biol. 6, 46–53 .

31. Jäger, S., Cimermancic, P., Gulbahce, N., Johnson, J. R., McGovern, K. E., Clarke, S. C., Shales, M., Mercenne, G., Pache, L., Li, K., Hernandez, H., Jang, G. M., Roth, S. L., Akiva, E., Marlett, J., et al. (2011) Global landscape of HIV-human protein complexes. Nature 481, 365–370.

32. Moarefi, I., LaFevre-Bernt, M., Sicheri, F., Huse, M., Lee, C. H., Kuriyan, J., and Miller, W. T. (1997) Activation of the Src-family tyrosine kinase Hck by SH3 domain displacement. Nature 385, 650–653.

33. Briggs, S. D., Sharkey, M., Stevenson, M., and Smithgall, T. E. (1997) SH3- mediated Hck tyrosine kinase activation and fibroblast transformation by the Nef protein of HIV-1. J. Biol. Chem. 272, 17899–17902.

34. Narute, P. S., and Smithgall, T. E. (2012) Nef alleles from all major HIV-1 clades activate Src-family kinases and enhance HIV-1 replication in an inhibitor-sensitive manner. PLoS One 7, e32561 .

35. Komuro, I., Yokota, Y., Yasuda, S., Iwamoto, A., and Kagawa, K. S. (2003) CSF-induced and HIV-1-mediated distinct regulation of Hck and C/ EBPb represent a heterogeneous susceptibility of monocyte-derived macrophages to M-tropic HIV-1 infection. J. Exp. Med. 198, 443–453.

36. Emerman, M. (1996). HIV-1, Vpr and the cell cycle. Current Biology, 6(9), 1096–1103. https://doi.org/10.1016/s0960-9822(02)00676-0

37. Cohen EA, Terwilliger EF, Jalinoos Y, Proulx J, Sodroski JG, Haseltine WA. Identification of HIV-1 vpr product and function. J Acquir Immune Defic Syndr (1988). 1990;3(1):11-8. PMID: 2136707.

38. Miyatake, H., Sanjoh, A., Murakami, T., Murakami, H., Matsuda, G., Hagiwara, K., Yokoyama, M., Sato, H., Miyamoto, Y., Dohmae, N., & Aida, Y. (2016). Molecular mechanism of HIV-1 Vpr for binding to importin-a. Journal of Molecular Biology, 428(13), 2744–2757.

39. Belzile, J.-P., Richard, J., Rougeau, N., Xiao, Y., & Cohen, E. A. (2010). HIV-1 Vpr induces the K48-linked polyubiquitination and proteasomal degradation of target cellular proteins to activate ATR and promote G2 arrest. J Virol, 84(7), 3320–3330.

40. Wu, Y., Zhou, X., Barnes, C. O., DeLucia, M., Cohen, A. E., Gronenborn, A. M., Ahn, J., & Calero, G. (2016). The DDB1-DCAF1-Vpr-UNG2 crystal structure reveals how HIV-1 Vpr steers human UNG2 toward destruction. Nature Structural & Molecular Biology, 23(10), 933–940.

41. Piller SC, Ewart GD, Premkumar A, Cox GB, Gage PW. Vpr protein of human immunodeficiency virus type 1 forms cation-selective channels in planar lipid bilayers. Proc Natl Acad Sci U S A. 1996 Jan 9;93(1):111-5. doi: 10.1073/pnas.93.1.111. PMID: 8552585; PMCID: PMC40188.

42. Piller SC, Jans P, Gage PW, Jans DA: Extracellular HIV-1 virus protein R causes a large inward current and cell death in cultured hippocampal neurons: implications for AIDS pathology. Proc Natl Acad Sci USA 1998,95:4595-4600.

43. UniProt Consortium. UniProt: the universal protein knowledgebase in 2021. Nucleic Acids Res. 2021 Jan 8;49(D1):D480-D489. doi: 10.1093/nar/gkaa1100. PMID: 33237286; PMCID: PMC7778908.

44. Tusnády GE, Simon I. The HMMTOP transmembrane topology prediction server. Bioinformatics. 2001 Sep;17(9):849-50. doi: 10.1093/bioinformatics/17.9.849. PMID: 11590105.

45. Krogh A, Larsson B, von Heijne G, Sonnhammer EL. Predicting transmembrane protein topology with a hidden Markov model: application to complete genomes. J Mol Biol. 2001 Jan 19;305(3):567-80. doi: 10.1006/jmbi.2000.4315. PMID: 11152613.
46. Morellet N, Bouaziz S, Petitjean P, Roques BP. NMR structure of the HIV-1 regulatory protein VPR. J Mol Biol. 2003 Mar 14;327(1):215-27. doi: 10.1016/s0022-2836(03)00060-3. PMID: 12614620.

47. Waterhouse A, Bertoni M, Bienert S, Studer G, Tauriello G, Gumienny R, Heer FT, de Beer TAP, Rempfer C, Bordoli L, Lepore R, Schwede T. SWISS-MODEL: homology modeling of protein structures and complexes. Nucleic Acids Res. 2018 Jul 2;46(W1):W296-W303. doi: 10.1093/nar/gky427. PMID: 29788355; PMCID: PMC6030848.

48. Alvarado JJ, Tarafdar S, Yeh JI, Smithgall TE. Interaction with the Src homology (SH3-SH2) region of the Src-family kinase Hck structures the HIV-1 Nef dimer for kinase activation and effector recruitment. J Biol Chem. 2014 Oct 10;289(41):28539-53. doi: 10.1074/jbc.M114.600031. Epub 2014 Aug 13. PMID: 25122770; PMCID: PMC4192505.

49. Lee J, Cheng X, Swails JM, Yeom MS, Eastman PK, Lemkul JA, Wei S, Buckner J, Jeong JC, Qi Y, Jo S, Pande VS, Case DA, Brooks CL 3rd, MacKerell AD Jr, Klauda JB, Im W. CHARMM-GUI Input Generator for NAMD, GROMACS, AMBER, OpenMM, and CHARMM/OpenMM Simulations Using the CHARMM36 Additive Force Field. J Chem Theory Comput. 2016 Jan 12; 12(1):405-13. doi: 10.1021/acs.jctc.5b00935. Epub 2015 Dec 3. PMID: 26631602; PMCID: PMC4712441.

50. Jiménez J, Doerr S, Martínez-Rosell G, Rose AS, De Fabritiis G. DeepSite: protein-binding site predictor using 3D-convolutional neural networks. Bioinformatics. 2017 Oct 1;33(19):3036-3042. doi: 10.1093/bioinformatics/btx350. PMID: 28575181.

51. Kozakov D, Grove LE, Hall DR, Bohnuud T, Mottarella SE, Luo L, Xia B, Beglov D, Vajda S. The FTMap family of web servers for determining and characterizing ligand-binding hot spots of proteins. Nat Protoc. 2015 May;10(5):733-55. doi: 10.1038/nprot.2015.043. Epub 2015 Apr 9. PMID: 25855957; PMCID: PMC4762777.

52. Spiegel JO, Durrant JD. AutoGrow4: an open-source genetic algorithm for de novo drug design and lead optimization. J Cheminform. 2020 Apr 17;12(1):25. doi: 10.1186/s13321-020-00429-4. PMID: 33431021; PMCID: PMC7165399.

53. Takemura K, Sato C, Kitao A. ColDock: Concentrated Ligand Docking with All-Atom Molecular Dynamics Simulation. J Phys Chem B. 2018 Jul 26;122(29):7191-7200. doi: 10.1021/acs.jpcb.8b02756. Epub 2018 Jul 11. PMID: 29993242.

54. Harvey MJ, Giupponi G, Fabritiis GD. ACEMD: Accelerating Biomolecular Dynamics in the Microsecond Time Scale. J Chem Theory Comput. 2009 Jun 9;5(6):1632-9. doi: 10.1021/ct9000685. Epub 2009 May 21. PMID: 26609855.

55. Deganutti G, Pipitò L, Rujan RM, et al. Hidden GPCR structural transitions addressed by multiple walker supervised molecular dynamics (mwSuMD). bioRxiv; 2022. DOI: 10.1101/2022.10.26.513870.

56. Song W, Corey RA, Ansell TB, Cassidy CK, Horrell MR, Duncan AL, Stansfeld PJ, Sansom MSP. PyLipID: A Python Package for Analysis of Protein-Lipid Interactions from Molecular Dynamics Simulations. J Chem Theory Comput. 2022 Feb 8;18(2):1188-1201. doi: 10.1021/acs.jctc.1c00708. Epub 2022 Jan 12. PMID: 35020380; PMCID: PMC8830038.

57. Morris GM, Huey R, Lindstrom W, Sanner MF, Belew RK, Goodsell DS, Olson AJ. AutoDock4 and AutoDockTools4: Automated docking with selective receptor flexibility. J Comput Chem. 2009 Dec;30(16):2785-91. doi: 10.1002/jcc.21256. PMID: 19399780; PMCID: PMC2760638.

58. Wecker, K., Morellet, N., Bouaziz, S., & Roques, B. P. (2002). NMR structure of the HIV-1 regulatory protein Vpr in H2O/trifluoroethanol. European Journal of Biochemistry, 269(15), 3779–3788. https://doi.org/10.1046/j.1432-1033.2002.03067.x

59. Drabik D, Chodaczek G, Kraszewski S, Langner M. Mechanical Properties Determination of DMPC, DPPC, DSPC, and HSPC Solid-Ordered Bilayers. Langmuir. 2020 Apr 14; 36(14):3826-3835. doi: 10.1021/acs.langmuir.0c00475. Epub 2020 Mar 24. PMID: 32176506; PMCID: PMC7467745.

60. Farrotti A, Bocchinfuso G, Palleschi A, Rosato N, Salnikov ES, Voievoda N, Bechinger B, Stella L. Molecular dynamics methods to predict peptide locations in membranes: LAH4 as a stringent test case. Biochim Biophys Acta. 2015 Feb;1848(2):581-92. doi: 10.1016/j.bbamem.2014.11.002. Epub 2014 Nov 13. PMID: 25445672.

61. Padhi S, Khan N, Jameel S, Priyakumar UD. Molecular dynamics simulations reveal the HIV-1 Vpu transmembrane protein to form stable pentamers. PLoS One. 2013 Nov 6;8(11):e79779. doi: 10.1371/journal.pone.0079779. PMID: 24223193; PMCID: PMC3819244.

62. Heinemann SH, Terlau H, Stühmer W, Imoto K, Numa S 1992. Calcium channel characteristics conferred on the sodium channel by single mutations. Nature 356: 441–443.

63. Zhou Y, Morais-Cabral JH, Kaufman A, MacKinnon R. Chemistry of ion coordination and hydration revealed by a K+ channel-Fab complex at 2.0 A resolution. Nature. 2001 Nov 1;414(6859):43-8. doi: 10.1038/35102009. PMID: 11689936.

64. Jensen MØ, Borhani DW, Lindorff-Larsen K, Maragakis P, Jogini V, Eastwood MP, Dror RO, Shaw DE. Principles of conduction and hydrophobic gating in K+ channels. Proc Natl Acad Sci U S A. 2010 Mar 30;107(13):5833-8. doi: 10.1073/pnas.0911691107. Epub 2010 Mar 15. PMID: 20231479; PMCID: PMC2851896.

65. Ong, E. B. B., Watanabe, N., Saito, A., Futamura, Y., Abd El Galil, K. H., Koito, A., Osada, H. (2011). Vipirinin, a coumarin-based HIV-1 Vpr inhibitor, interacts with a hydrophobic region of VPR. The Journal of Biological Chemistry, 286(16), 14049–14056.

Plagiarism Certificate

DrillBit

The Report is Generated by DrillBit Plagiarism Detection Software

Submission Information

Author Name	Satyabrata Majumder
Title	Studies on the conformational dynamics of the HIV-1 accessory proteins to guide new therapeutic development
Paper/Submission ID	1127057
Submitted by	kalyan.dbs@presiuniv.ac.in
Submission Date	2023-11-23 17:50:12
Total Pages	13
Document type	Synopsis

Result Information

Similarity **9 %**

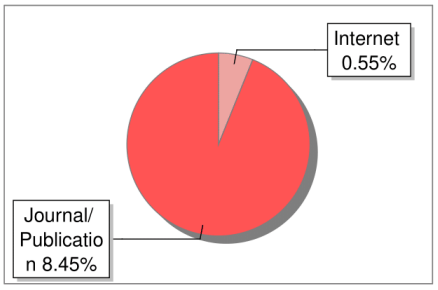

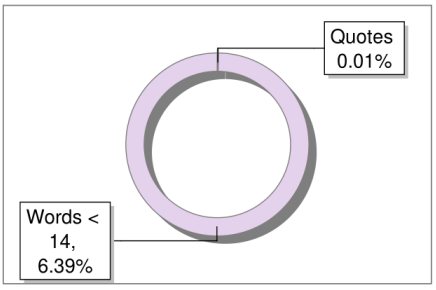

Exclude Information

Quotes	Excluded
References/Bibliography	Excluded
Sources: Less than 14 Words Similarity	Excluded
Excluded Source	**0 %**
Excluded Phrases	Not Excluded

A Unique QR Code use to View/Download/Share Pdf File

DrillBit

DrillBit Similarity Report

9	8	A	A-Satisfactory (0-10%) B-Upgrade (11-40%) C-Poor (41-60%) D-Unacceptable (61-100%)
SIMILARITY %	MATCHED SOURCES	GRADE	

LOCATION	MATCHED DOMAIN	%	SOURCE TYPE
1	www.dx.doi.org	6	Publication
2	Ligand-Dependent Conformations and Dynamics of the Serotonin 5-HT2A Receptor Det by Shan-2012	1	Publication
3	ndl.ethernet.edu.et	1	Publication
4	scholar.sun.ac.za	<1	Publication
5	www.frontiersin.org	<1	Publication
6	mdpi.com	<1	Internet Data
7	ebin.pub	<1	Internet Data
8	Orientation measurements of clay minerals by polarized attenuated total reflecti by Grgoire-2020	<1	Publication

Conferences Attented

4th REGIONAL SCIENCE AND TECHNOLOGY CONGRESS
(SOUTHERN REGION), 2019
Jointly Organised By
DEPARTMENT OF SCIENCE & TECHNOLOGY AND BIO-TECHNOLOGY, GOVT. OF WEST BENGAL
&
MAULANA ABUL KALAM AZAD UNIVERSITY OF TECHNOLOGY, WEST BENGAL

This is to certify that Prof./Dr./Mr./Ms. Satyabrata Majumder. of Presidency University is the presenting Author / Co-author / Corresponding Author in Oral / Poster / Exhibition session of the 4th Regional Science and Technology Congress (Southern Region) 2019, jointly organised by Department of Science and Technology and Bio-Technology, Government of West Bengal & Maulana Abul Kalam Azad University of Technology, West Bengal during December 23-24, 2019 at Haringhata, Nadia-741249.

Dr. Somdatta Chakravortty
Organising Secretary
4th Regional Science and Technology Congress (Southern Region), 2019
Maulana Abul Kalam Azad University of Technology, West Bengal

Dr. Suchandra Choudhury
Organising secretary
4th Regional Science and Technology Congress (Southern Region), 2019
Department of Science & Technology and Bio-Technology, Govt. of West Bengal

---

"When Science Meets Life"

SOCIETY OF BIOLOGICAL CHEMISTS (I), KOLKATA CHAPTER
Organizes a Two Day Symposium on
9th & 10th April 2022
&
Presents this Certificate to

Satyabrata Majumder

In appreciation of Oral/Poster presentation/Participation in the symposium at Sister Nivedita University, Newtown, West Bengal

President | **Secretary**

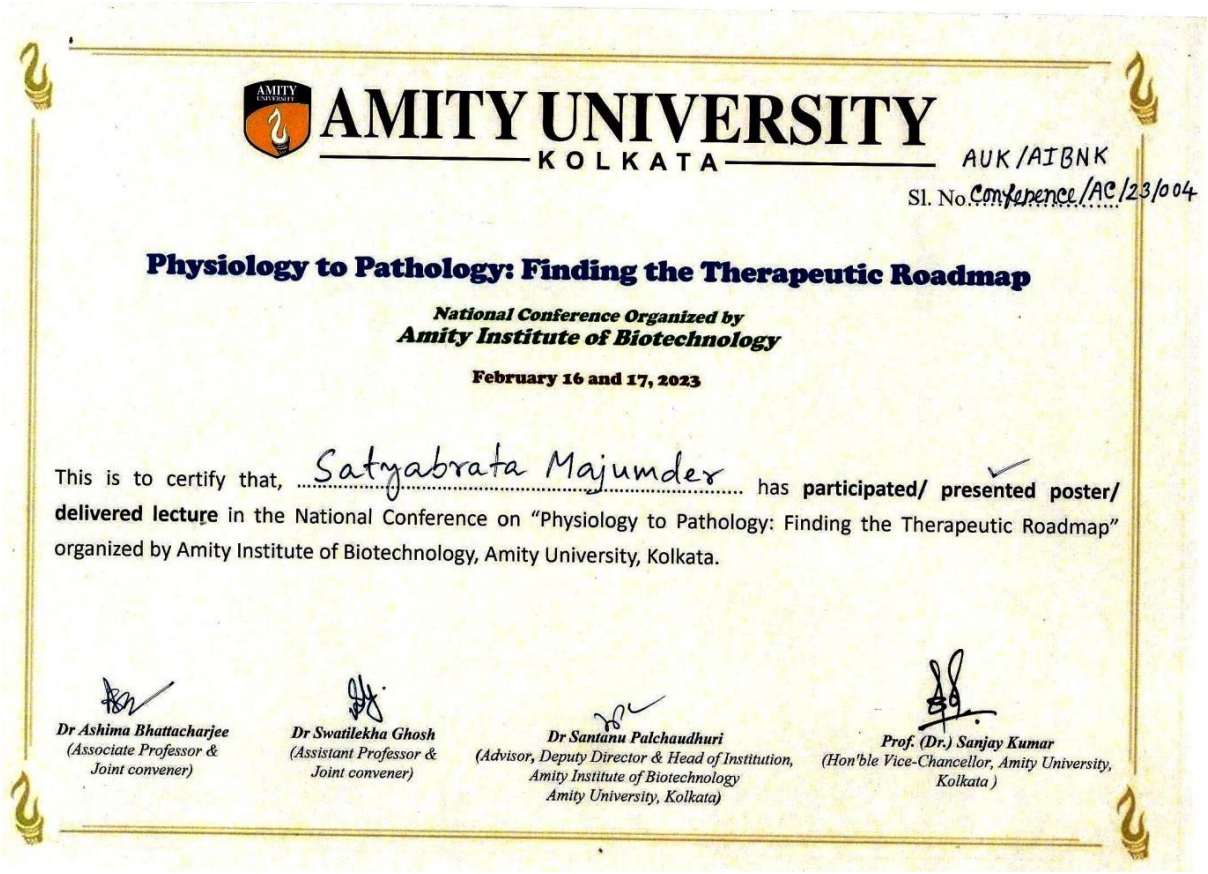

AMITY UNIVERSITY
KOLKATA

AUK/AIBNK
Sl. No. Conference/AC/23/004

Physiology to Pathology: Finding the Therapeutic Roadmap

National Conference Organized by
Amity Institute of Biotechnology

February 16 and 17, 2023

This is to certify that, Satyabrata Majumder has **participated/ presented poster/ delivered lecture** in the National Conference on "Physiology to Pathology: Finding the Therapeutic Roadmap" organized by Amity Institute of Biotechnology, Amity University, Kolkata.

Dr Ashima Bhattacharjee
(Associate Professor & Joint convener)

Dr Swatilekha Ghosh
(Assistant Professor & Joint convener)

Dr Santanu Palchaudhuri
(Advisor, Deputy Director & Head of Institution, Amity Institute of Biotechnology Amity University, Kolkata)

Prof. (Dr.) Sanjay Kumar
(Hon'ble Vice-Chancellor, Amity University, Kolkata)

EXCELLENCE SINCE 1817

Certificate of Participation

This is to certify that

Satyabrata Majumder

Presidency University, Kolkata

BIOMOLECULES TO BIOME
N-terminal LIFE SCIENCES C-terminal

presented ***POSTER*** in the two day **International Conference (Online) on**

"Biomolecules To Biome" held on August 24-25, 2022

Organized by **Department of Life Sciences, Presidency University, Kolkata, India.**

Dr. Ranjana Pal & Dr. Puja Ray
Joint Organizing Secretaries
Biomolecules To Biome - 2022

Prof. Prabir Kumar Mukhopadhyay
HOD (Life Sciences)
Presidency University, Kolkata
(Chairman)

Prof. Sankar Bose
Dean of Faculty of Natural and Mathematical Sciences
(Patron)

JOURNAL OF BIOMOLECULAR STRUCTURE AND DYNAMICS
https://doi.org/10.1080/07391102.2021.1954553

Taylor & Francis
Taylor & Francis Group

Check for updates

An insight into the binding mechanism of Viprinin and its morpholine and piperidine derivatives with HIV-1 Vpr: molecular dynamics simulation, principal component analysis and binding free energy calculation study

Satyabrata Majumder and Kalyan Giri

Department of Life Sciences, Presidency University, Kolkata

Communicated by Ramaswamy H. Sarma

ABSTRACT

HIV-1 Vpr is an accessory protein responsible for a plethora of functions inside the host cell to promote viral pathogenesis. One of the major functions of Vpr is the G_2 cell cycle arrest. Among several small molecule inhibitors, Viprinin, a coumarin derivative, has been shown to specifically inhibit the G_2 cell cycle arrest activity of Vpr thus making it an excellent choice for a lead molecule to design antiretroviral drug. But the exact mechanism of binding of the Viprinin and its two potent derivatives with Vpr is still not understood. In this study with combined molecular docking, molecular dynamics simulation, Molecular Mechanics Poisson-Boltzmann Surface Area (MM-PBSA) method, Principal component analysis and Umbrella sampling simulation, we have explored the binding mechanism of Viprinin and its two derivatives with Vpr. MM-PBSA and Umbrella sampling calculations suggest that Viprinin and ViprininD1 have higher binding energy than ViprininD2. Molecular dynamics simulation shows that the ligands are not very stable inside the initial binding pocket and various hydrophobic interactions are responsible to hold the ligands with Vpr. Vpr backbone Principle Component Analysis (PCA) shows various unique essential motions of Vpr bound with Viprinin and its two derivatives. This study may give detailed insight of the mode of binding of the specified compounds at atomic scale and provide valuable information about the possibility of using these compounds as a potent Vpr inhibitor.

Abbreviations: HIV-1: Human Immunodeficiency Virus tytpe 1; Vpr: Viral protein r; MM-PBSA: Molecular Mechanics Poisson-Boltzmann Surface Area; RMSD: Root mean square deviation; RMSF: Root mean square fluctuation; PCA: Principal Component analysis; PMF: Potential of Mean Force; AIDS: Acquired immune deficiency syndrome; GA: Genetic Algorithm

ARTICLE HISTORY
Received 22 August 2019
Accepted 2 July 2021

KEYWORDS
HIV-1 Vpr; Viprinin; Molecular Dynamics Simulation; MM-PBSA; Principal Component Analysis; Umbrella sampling

1. Introduction

Human immunodeficiency virus 1 is the causative agent of AIDS and it belongs to lentiviral family that encodes six accessory proteins, Tat, Rev, Vpu, Vif, Nef, and Vpr along with retroviral Gag, Pol and Env proteins. Viral protein R (Vpr) is a 96 amino acid, 14 kDa protein (Yuan et al., 1990) and it plays crucial roles in virus spread, pathogenesis and virus replication efficiency (Levy et al., 1994; Ogawa et al., 1989). It performs a myriad of functions inside the host cell to promote disease progression and hence contributes to the development of AIDS. Vpr is characterized by the presence of three well-defined α-helices spanning residues 17-33, 38-50 and 56-77 and random coils at the N- and C-termini (Morellet et al., 2003). Amino acid residues residing in three α-helices are important for its multifunctional role. For example, residues W18, Q3, L22, K27, L23, and F34 of Helix 1 are associated with the cytopathic functions of Vpr (Barnitz et al., 2011; Chen et al., 1999; Stromájer-Rácz et al., 2010); Residues 52-96 (Helix 3 and C-terminal random coil) are shown to bind with ANT and results in the induction of apoptosis (Jacotot et al., 2001); residues in the region 71-82 are involved in mitochondrial membrane permeabilization-inducing (MMP) activity (Jacotot et al., 2001) etc. Among all the functions, two most important functions of Vpr are viral Pre-Integration Complex(PIC) transportation from cytoplasm to the host cell nucleus via interaction with importin-α and G_2 cell cycle arrest (González, 2017).

Nuclear import of Viral PIC in non-dividing cells, such as Macrophages, is one of the major function of Vpr (Popov et al., 1998). Previously it was demonstrated that Vpr transports PIC through Importin-α mediated pathway and the region 17-74 is responsible for the interaction (Kamata et al., 2005). Recent crystal structure of Vpr C-terminal 85-96 in complex with Importin-α2 reveals the actual mode of binding between Vpr and Importin-α and the process of Nuclear transportation (Miyatake et al., 2016). In the case of Vpr mediated G_2 cell cycle arrest, different mechanisms have been proposed, but the exact mechanism is still poorly understood. A study demonstrated that Vpr forms a chromatin-associated nuclear focus by recruiting VprBP-DDB1 complex and targets a chromatin-bound substrate whose Ubiquitination and proteolysis initiates the activation of ataxia

CONTACT Kalyan Giri kalyan.dbs@presiuniv.ac.in Department of Life Sciences, Presidency University, 86/1 College Street, Kolkata, 700073, India.
Supplemental data for this article can be accessed online at http://doi.org/10.1080/07391102.2021.1954553.
© 2021 Informa UK Limited, trading as Taylor & Francis Group

Computational Biology and Chemistry 104 (2023) 107871

Contents lists available at ScienceDirect

Computational Biology and Chemistry

journal homepage: www.elsevier.com/locate/cbac

Computer-aided *de novo* design and optimization of novel potential inhibitors of HIV-1 Nef protein

Satyabrata Majumder [a], Giuseppe Deganutti [b], Ludovico Pipitò [b], Dwaipayan Chaudhuri [a], Joyeeta Datta [a], Kalyan Giri [a,*]

[a] Department of Life Sciences, Presidency University, Kolkata, India
[b] Centre for Sport, Exercise, and Life Sciences, Coventry University, Coventry CV1 5FB, UK

ARTICLE INFO

Keywords:
HIV-1 Nef protein
De Novo ligand design
Supervised molecular dynamics

ABSTRACT

Nef is a small accessory protein pivotal in the HIV-1 viral replication cycle. It is a multifunctional protein and its interactions with kinases in host cells have been well characterized through many in vitro and structural studies. Nef forms a homodimer to activate the kinases and subsequently the phosphorylation pathways. The disruption of its homodimerization represents a valuable approach in the search for novel classes of antiretroviral. However, this research avenue is still underdeveloped as just a few Nef inhibitors have been reported so far, with very limited structural information about their mechanism of action. To address this issue, we have employed an *in silico* structure-based drug design strategy that combines de novo ligand design with molecular docking and extensive molecular dynamics simulations. Since the Nef pocket involved in homodimerization has high lipophilicity, the initial de novo-designed structures displayed poor drug-likeness and solubility. Taking information from the hydration sites within the homodimerization pocket, structural modifications in the initial lead compound have been introduced to improve the solubility and drug-likeness, without affecting the binding profile. We propose lead compounds that can be the starting point for further optimizations to deliver long-awaited, rationally designed Nef inhibitors.

1. Introduction

Human immunodeficiency virus 1 (HIV-1), a member of the Lentiviral family, is the causative agent of acquired immune deficiency syndrome (AIDS). It encodes six accessory proteins (Tat, Rev, Vpu, Vif, Nef, and Vpr) along with other regulatory proteins (Sterbel et al., 2013). Nef is a relatively small (27–34 kDa) nonenzymatic auxiliary protein that is expressed early in the viral life cycle and performs a plethora of functions inside the host cells. Early research indicated that Nef was a "negative factor" for HIV-1 replication, which led to its initial naming (Ahmad and Venkatesan, 1988). Nef is an important player in viral pathogenesis by promoting viral replication and enabling immune escape in infected hosts (Staudt et al., 2020). Early pieces of evidence showed that expression of Nef in $CD4^+$ T-cells and macrophages causes AIDS-like disease in transgenic mice and that patients infected with *nef* defective HIV-1 fail to progress to AIDS suggesting a direct role for Nef in HIV-1 pathogenesis (Jolicoeur, 2011; Hanna et al., 1998; Rhodes et al., 2000; Kirchhoff et al., 1995).

Nef is composed of two main parts: the N-terminal anchor region and a folded core region in which a flexible internal loop (~25 residues) is present. The N-terminal 60 amino acids that make up the anchor region are mainly unstructured and contain a myristoylation site at the starting glycine residue. This myristoylation helps the Nef anchoring to the flexible core of the membrane leaflet. It interacts with a plethora of membrane proteins and factors such as CD4, CXCR4, CCR5, MHC-I, T-cell receptor, SERINC5, trafficking proteins, guanine nucleotide exchange factors, protein kinases, etc. (Usami et al., 2015; Saksela, 2011; Geyer et al., 1999; Gerlach et al., 2010; Akgun et al., 2013; Kent et al., 2010; Jägeret al., 2011). Numerous structural and in vitro studies on the recruitment and activation of Src-family kinases indicated that Nef preferentially binds to the SH3 domain of the Hck and Lyn kinases and displaces the SH3 domain from the kinase regulatory position resulting in constitutive kinase activation in vitro systems (Moarefi et al., 1997; Briggs et al., 1997). Nef-dependent activation of the Hck is a conserved function of all HIV-1 Nef M-group subtypes (Narute et al., 2012) Previous studies showed that both the expression of a dominant-negative

* Correspondence to: Department of Life Sciences, Presidency University, 86/1 College Street, Kolkata 700073, India.
E-mail address: kalyan.dbs@presiuniv.ac.in (K. Giri).

https://doi.org/10.1016/j.compbiolchem.2023.107871
Received 19 December 2022; Received in revised form 7 April 2023; Accepted 14 April 2023
Available online 15 April 2023
1476-9271/© 2023 Elsevier Ltd. All rights reserved.

This document is confidential and is proprietary to the American Chemical Society and its authors. Do not copy or disclose without written permission. If you have received this item in error, notify the sender and delete all copies.

Computational insights into the Conformational Dynamics of HIV-1 Vpr in lipid bilayer for ion channel modeling

Journal:	*Journal of Chemical Information and Modeling*
Manuscript ID	ci-2023-01859e
Manuscript Type:	Article
Date Submitted by the Author:	19-Nov-2023
Complete List of Authors:	Majumder , Satyabrata ; Presidency University Kolkata Deganutti, Giuseppe; Coventry University, Centre for Sport, Exercise and Life Sciences Pipito , Ludovico ; Coventry University, Centre for Sport, Exercise and Life Sciences Chaudhuri, Dwaipayan; Presidency University Kolkata Datta, Joyeeta ; Presidency University Kolkata Giri, Kalyan; Presidency University Kolkata, Life Sciences

SCHOLARONE™
Manuscripts

Revision submitted